University of Natural Resources and Life Sciences, Vienna

Lincoln University
Te Whare Wānaka o Aoraki
CHRISTCHURCH•NEW ZEALAND

CHEMICAL IMAGING IN THE RHIZOSPHERE OF ARSENIC HYPERACCUMULATING FERNS (*PTERIS VITTATA* AND *PTERIS QUADRIAURITA*)

Master Thesis

Submitted by

Stefan Wagner, BSc.

Vienna, October 2017

Supervised by

Univ.Prof. Dipl.-Ing. Dr.nat.techn.
Walter W. Wenzel

Institute of Soil Research, Department of Forest- and Soil Sciences, University of Natural Resources and Life Sciences, Vienna, Austria

Prof. Dr.
Brett Robinson

Department of Soil and Physical Sciences, Faculty of Agriculture and Life Sciences, Lincoln University, New Zealand

Co-supervised by

Dipl.-Ing. Dr. Christoph Höfer

Priv.-Doz. Dr. Markus Puschenreiter

Institute of Soil Research, Department of Forest- and Soil Sciences, University of Natural Resources and Life Sciences, Vienna, Austria

ACKNOWLEDGEMENTS

At first, I would like to thank my BOKU supervisors Prof. Walter Wenzel, Dr. Markus Puschenreiter and Dr. Christoph Höfer for their generous guidance and advice over the course of this work. Walter and Markus, thank you for letting me be a part of your outstanding research group and providing the best working environment a student could possibly wish for. Christoph, without your confidence in my abilities, your continuous and candid support, and your brilliant as well as fresh ideas this thesis could not have been accomplished.

Equally, I want to thank my LU co-supervisor Prof. Brett Robinson for improving my skills in soil chemistry and scientific writing during my stay in New Zealand. I also owe thanks to Dr. Jakob Santner for sharing his expertise on chemical imaging and Dr. Eva Oburger for helping me with experimental work that did not make it into this thesis.

I further thank all team members of the *Rhizosphere Ecology and Biogeochemistry Group* who kept me going through the constant supply with food for body and mind – both in and off the lab. Special thanks to Sebastian Ehrmann, Daniel Schwertberger and Christina Roschitz for their helping hands whenever the workload seemed overwhelming.

Last but not least, I express my deep gratitude to my beloved family and close friends for their exceptional support, trust and patience throughout my educational career. I am truly blessed to be backed by such wonderful people.

Pteris Vittata

ABSTRACT

Background. Arsenic (As)-hyperaccumulating ferns are used for gentle, plant-based remediation (i.e., phytoremediation) of As-contaminated soil and serve as valuable model species to unravel As acquisition and tolerance mechanisms in terrestrial plants. Yet, the processes controlling the biogeochemical fate of As in the soil-root interface (i.e., the rhizosphere) of As-hyperaccumulators are still poorly understood due to an apparent lack of information on As transformation and speciation dynamics at rhizosphere scale.

Aims. In this thesis we investigated the *in situ* distribution of labile inorganic As species (i.e., arsenite (As^{III}) and arsenate (As^{V})), their biogeochemically associated solutes (i.e., phosphorus (P), manganese (Mn), and iron (Fe)), and molecular oxygen (O_2) at high spatial (sub-mm) resolution alongside individual root axes of two As-hyperaccumulating ferns (*Pteris vittata* and *P. quadriaurita*) grown in highly As-contaminated soil. To this end, a rhizotron experiment was performed using two different chemical imaging methods simultaneously, including (i) novel dual-layer diffusive gradients in thin films (DGT) technology combined with laser ablation-inductively coupled plasma-mass spectrometry (LA-ICP-MS) and (ii) planar optodes (PO).

Results. We found well-developed zones of labile As^{V} depletion in the rhizosphere of *P. vittata*, confining localized zones of labile As^{III} and As^{V} co-accumulation along its roots. The increased As^{III}/As^{V} concentrations coincided with elevated levels of labile Mn, whereas labile Fe fractions remained consistently unchanged. While zones of labile As^{V} depletion, co-localized with decreased concentrations of labile P, occurred independent of the fern species, no increased levels of labile As^{III}/As^{V} relative to bulk soil were found in the rhizosphere of *P. quadriaurita*. Simultaneously, we observed extensive O_2 depletion expanding around roots of both fern species.

Conclusions. Our results show that species-dependent root activities of the As-hyperaccumulating ferns trigger highly localized redox reactions controlling As transformation and speciation in the rhizosphere soil. Following As^{V} uptake in *P. vittata* root tissues, As is partly released back into the soil environment, raising concern about its use in phytoremediation of highly As-contaminated soil. Highly localized co-accumulation of labile As^{III}/As^{V} alongside *P. vittata* roots indicates either As^{V} mobilization from the soil matrix and/or (bio)chemical re-oxidation of released As^{III}, with O_2, Mn (oxyhydr)oxides and As-resistant

microorganisms serving as electron acceptors. These findings provide novel insight into the complexity of biogeochemical interactions in the rhizosphere of As-hyperaccumulators, and may help to improve sustainable As mitigation strategies.

KURZFASSUNG

Hintergrund. Arsen (As)-hyperakkumulierende Farne werden für die sanfte, durch Pflanzen gestützte Sanierung (Phytosanierung) von As-kontaminierten Böden verwendet und dienen als wertvolle Modell Spezies um As Akquirierungs- und Toleranzmechanismen in terrestrischen Pflanzen aufzuklären. Aufgrund eines offensichtlichen Mangels an Informationen zur As Transformations- und Speziierungsdynamik in der Boden-Wurzel Grenzfläche (Rhizosphäre) von As-Hyperakkumulatoren, sind die Prozesse, welche das biogeochemische Verhalten von As in Interaktion mit anderen Elementen und unter Einfluss von Wurzelaktivitäten kontrollieren, noch weithin unbekannt.

Ziele. Das Ziel dieser Masterarbeit war es deshalb die *in situ* Verteilung von gelösten anorganischen As Spezies (Arsenit (As^{III}) und Arsenat (As^{V})), deren biogeochemisch assoziierten gelösten Elementen (Phosphor (P), Mangan (Mn) und Eisen (Fe)), und molekularem Sauerstoff (O_2) in hoher räumlicher (sub-mm) Auflösung entlang einzelner Wurzeln von zwei As-Hyperakkumulatoren (*Pteris vittata* und *P. quadriaurita*), gezogen auf einem stark As-kontaminierten Boden, zu erforschen. Hierzu führten wir ein Rhizotron Experiment durch bei welchem zwei chemische Bildgebungsmethoden simultan verwendet wurden, einschließlich (i) einer neuartigen zweischichtigen ‚Diffusionsgradienten in Dünnschichten (DGT)' Probenahme in Kombination mit Laser Ablation-induktiv gekoppelter Plasma-Massenspektrometrie (LA-ICP-MS) und (ii) planare Optoden (PO).

Ergebnisse. In der Rhizosphäre von *P. vittata* traten ausgeprägte Zonen verminderter labiler As^{V} Konzentrationen auf, welche ko-lokalisierte Zonen von erhöhten labilen As^{III} und As^{V} Konzentrationen entlang der Wurzeln begrenzten. Die erhöhten As^{III}/As^{V} Konzentrationen waren deckungsgleich mit erhöhten Werten von labilen Mn Spezies, wohingegen labile Fe Fraktionen beständig unverändert blieben. Während Zonen verminderter labiler As^{V} Konzentrationen, ko-lokalisiert mit verminderten labilen P Konzentrationen, unabhängig von der Farnspezies auftraten, wurden, im Vergleich zum restlichen Boden, keine erhöhten labilen As^{III}/As^{V} Werte in der Rhizosphäre von *P. quadriaurita* gemessen. Gleichzeitig beobachteten wir im durchwurzelten Boden beider Farnspezies eine extensive Abnahme von O_2.

Fazit. Die in dieser Masterarbeit präsentierten Daten zeigen, dass artspezifische Wurzelaktivitäten der As-hyperakkumulierenden Farne stark lokalisierte Redoxreaktionen

induzieren, welche die Transformation und Speziierung von As in der Rhizosphäre kontrollieren. Nach der Wurzelaufnahme von As^{V} durch *P. vittata* wird As teilweise wieder in die Bodenumwelt zurückgeführt, was ihre Verwendung in der Phytosanierung von Böden mit hoher As-Kontamination in Frage stellt. Die räumlich stark begrenzte, ko-lokalisierte Anreicherung von labilem As^{III}/As^{V} indiziert eine As^{V} Mobilisierung von der Bodenmatrix und/oder eine (bio)chemische Reoxidation von freigesetztem As^{III} bei welcher O_2, Mn-(oxyhydr)oxide und As-resistente Mikroorganismen als Elektronenakzeptoren fungieren. Diese Erkenntnisse bieten einen neuen Einblick in die Komplexität der biogeochemischen Interaktionen in der Rhizosphäre von As-Hyperakkumulatoren, und können zu einer Verbesserung nachhaltiger Strategien zur Schadensminderung von As beitragen.

TABLE OF CONTENTS

ABBREVIATIONS

The following list describes the meaning of various abbreviations and acronyms used in this thesis.

Abbreviation	Description
2D	two-dimensional
AM	arbuscular mycorrhiza
AR	arsenate reductase
C_{DGT}	time-averaged concentration at interface of DGT device and medium
CEC	cation exchange capacity
CRM	certified reference material
DAP	days after planting
DGT	diffusive gradients in thin films
DOC	dissolved organic carbon
dwt	oven-dry weight (105 °C)
EC	electrical conductivity
E_h	soil redox potential
f_{DGT}	time-averaged solute flux into the DGT binding layer
Forst99	arsenic-contaminated experimental soil from Carinthia, Austria
MBG	mixed binding gel
MSG	mercapto silica gel
MWHC	maximum water holding capacity (%)
ICP-OES	inductively coupled plasma optical emission spectrometry
ICP-MS	inductively coupled plasma mass spectrometry
LA	laser ablation
LMWOA(s)	low-molecular-weight-organic-anion(s)
LOD	limit of detection
LOQ	limit of quantification
MY	Macrolex® fluorescence yellow 10GN
n	sample size, number of replicates
PE	polyethylene
PO(s)	planar optode(s)
PP	polypropylene
PTFE	polytetrafluoroethylene
PtOEP	platinum(II)octaethylpor-phyrin
ROI(s)	region of interest(s)

rpm	revolutions per minute
RSD	relative standard deviation
RT	rhizotron
SEM	standard error of the mean
SSR	soil:solution ratio
TEA(s)	terminal electron acceptor(s)
TF	translocation factor
WR	working range

1 INTRODUCTION

Arsenic (As) is an abundant trace metalloid in the geosphere that is classified by the International Agency for Research on Cancer (IARC) as a non-threshold human carcinogen (IARC, 2004). Despite its natural abundance, typical As concentrations in uncontaminated soils are low, ranging between 0.1-55 mg kg^{-1} (Wenzel, 2013). Unfortunately, natural processes (i.e., geogenic weathering of As-bearing parent materials or volcanic emissions) and human activities (e.g. metal ore mining and processing or the use of As-tainted groundwater for crop irrigation) lead to drastically increased soil As concentrations, causing adverse effects on human health in numerous regions worldwide (Adriano, 2001; Smedley and Kinniburgh, 2013; Edmunds et al., 2015).

Plant species differ considerably in their sensitivity to As and only few terrestrial plants tolerate elevated soil As concentrations. Among them, *Pteris vittata* L. (Chinese brake fern) and eleven other species in the *Pteridaceae* family of ferns are able to hyperaccumulate As without facing toxic effects (Ma et al., 2001; Wang and Ma, 2015). *P. vittata* is the pioneer As-hyperaccumulating plant and has the capability to accumulate up to 22,000 mg As kg^{-1} dry weight (dwt) in its above-ground tissues (i.e., fronds) (Ma et al., 2001) as compared to <1 mg As kg^{-1} dwt in most plants (Adriano, 2001). Thus, *P. vittata* may be used for phytoextraction, a plant-based remediation (i.e., phytoremediation) technology that employs hyperaccumulating plants on-site to reduce the concentration of inorganic metal(loid) pollutants in contaminated media below risk-based thresholds (Baker et al., 1994; Salt et al., 1998; Wenzel, 2009). Moreover, *P. vittata* has become a unique model species to study the mechanisms of As hyperaccumulation and detoxification in the kingdom plantae. Although advances have been achieved (Zhao et al., 2009; Danh et al., 2014; Han et al., 2017b), our understanding of As dynamics and its complex interplay with other element fluxes (particularly phosphorus (P), manganese (Mn), and iron (Fe)) in the soil-root interface (i.e., the rhizosphere) of hyperaccumulating ferns remains largely unknown.

1.1 Arsenic speciation in the soil environment

Arsenic in soil exists naturally in a large variety of organic and inorganic chemical forms (species). These species differ in their physico-chemical characteristics, resulting in different reactivity, mobility, phytoavailability, and phytotoxicity (Adriano, 2001; Fitz and Wenzel, 2006). Inorganic As species, including the trivalent arsenite (As^{III}) and the pentavalent arsenate (As^{V}), predominate in terrestrial soils and are generally considered more toxic than organic arsenicals (Wenzel, 2013). Acting as a phosphate analogue, As^{V} can substitute inorganic P in many biochemical reactions such as ATP synthesis, thus interfering with life's main energy generation system. Its reduced counterpart, As^{III}, is generally considered more toxic than As^{V} due to its broad interaction with critical sulfhydryl (–SH) groups in proteins, disrupting enzymatic activity and cellular metabolism (Hughes, 2002).

The speciation of inorganic As in soil is thermodynamically dictated by the reduction-oxidation (redox) potential (E_h) and pH. In soil solutions of aerobic (oxic) soil systems (E_h >200 mV), and within a common pH range (pH 4-9), As^{V} prevails and occurs as dissociation products ($H_2AsO_4^-$ at pH <7 and $HAsO_4^{2-}$ at pH >7) of arsenic acid (H_3AsO_4) (Masscheleyn et al., 1991; Sadiq, 1997). The As^{V} oxyanions are generally poorly mobile due to strong adsorption to positively charged surfaces of Fe (oxyhydr)oxides, which are the quantitatively most important secondary mineral binding phases for As in soils (Wenzel, 2013). With increasing pH and/or increasing anionic competition, As^{V} may be mobilized into solution due to the increasing negative surface charge of the soil matrix, leading to enhanced electrostatic As^{V} repulsion (Smedley and Kinniburgh, 2002). At anaerobic (anoxic) soil conditions (E_h <200 mV), As appears mainly as As^{III} ($H_3AsO_3^0$) (Masscheleyn et al., 1991). Given the high pK_a (9.23) of arsenous acid (H_3AsO_3), As^{III} is undissociated at pH values <9 and therefore has a higher mobility than As^{V}.

Once dissolved, inorganic As species can readily undergo (bio)chemical transformation. Both, abiotic and biotic redox reactions are likely causes for the thermodynamically unfavorable co-existence of As^{III} and As^{V} in aerobic soil environments. The abiotic As transformation is triggered by changes in the soil E_h and the availability of redox partners for the reduction of As^{V} (S(II), Fe(II), H_2, reduced organic acids) (Rochette et al., 2000; Jones et al., 2000) or the oxidation of As^{III} (O_2, Mn(III, IV) (oxyhydr)oxides, Fe(II)-activated goethite, Fe(IV) via H_2O_2 Fenton reactions) (Oscarson et al., 1981; Scott and Morgan, 1995; Borch et al., 2010). These abiotic transformation processes proceed at substantially slower rates than biotic reactions

(Newman et al., 1997; Huang, 2014). The biotic As transformation is mainly mediated by various microorganisms that are able to oxidize As^{III} or reduce As^{V} either directly, via detoxification or dissimilatory energy generation/conservation mechanisms (Oremland and Stolz, 2003), or indirectly, via production of reactive inorganic or organic compounds (Jiang et al., 2009). Root activities not only influence As transformation processes through the stimulation of the microbial community, but can also directly contribute to As transformation and speciation in the rhizosphere microenvironment (Fitz and Wenzel, 2002).

1.2 Arsenic uptake and transformation in hyperaccumulator ferns

Arsenic hyperaccumulating ferns are native to aerobic soils where As^{V} is the predominant As species available for plant uptake. Nonetheless, both As^{III} and As^{V} can be taken up in root tissues. There is consensus that As^{V} may be taken up by higher plants via P transporter proteins (Wang et al., 2002; Zhao et al., 2009). However, in hyperaccumulating plants (e.g. *P. vittata*), As^{V}/P-transporters may have a higher affinity for As^{V} than in non-accumulator plants, indicated by substantially higher As^{V} influx and lower K_m (Michaelis-Menten constant) values in hyperaccumulating *Pteris* species (Poynton et al., 2004). The transporters responsible for As^{III} uptake in *P. vittata* are less clear. While aquaporin water channels belonging to the family of major intrinsic proteins (MIPs) have been identified to passively mediate As^{III} uptake in many non-accumulator plants (Zhao et al., 2009), their action in As^{III} uptake in *P. vittata* has been questioned as As^{III} influx into *P. vittata* roots appears to be controlled by an transporter-mediated active, i.e., energy-dependent, process with passive loading being negligible (Wang et al., 2011). Only recently, He et al. (2016) demonstrated that the aquaporin PvTIP4;1 from *P. vittata* may also mediate As^{III} uptake in its root tissues.

Once As^{III}/As^{V} is absorbed by *P. vittata* roots, As translocation into the fronds via xylem transport proceeds rapidly (Su et al., 2008). Although mainly As^{V} is taken up from soil, As^{III} predominates in *P. vittata* xylem sap and frond tissues (Su et al., 2008; Zhao et al., 2009), pointing at As^{V} reduction within the plant. Transformation of As^{V} to As^{III} via arsenate reductase (AR) is considered a major detoxification mechanism in *P. vittata*, as it limits the strong competition between As^{V} and P for the same transporter and reduces the overall interference of As with plant P nutrition (Zhao et al., 2009). To inhibit its phytotoxic effects, As^{III} may be efficiently sequestered both, intracellularly in the epidermal cell vacuoles (Lombi et al., 2002), and exocellularly in the pinnae cell apoplasm of *P. vittata* fronds (Datta et al., 2017). The

location of As^{V} conversion to As^{III} in *P. vittata*, however, remains controversial: whereas earlier works speculated that As^{V} is mainly reduced in the fronds (Kertulis et al., 2005; Pickering et al., 2006), increasing evidence suggests that As^{V} reduction primarily occurs in the roots (Duan et al., 2005; Su et al., 2008; Liu et al., 2009) and the rhizomes (Mathews et al., 2010; Wan et al., 2017). Recently, Cesaro et al. (2015) demonstrated the constitutive expression of two AR proteins in both fronds and roots of *P. vittata* sporophytes. Upon exposure to As^{V}, the AR activity in the root tissues was up-regulated, indicating that As^{V} reduction in roots is essential for efficient As detoxification and translocation when grown at elevated soil As^{V} levels.

1.3 Arsenic speciation in the rhizosphere of hyperaccumulator ferns

Despite being a major entry point for As into the food chain, only few researchers have explored As species and dynamics in the rhizosphere. Some studies, based on rhizobox and rhizobag experiments, have demonstrated that relatively high As^{III} levels can occur in aerobic rhizosphere soil solutions compared to bulk soil (Ultra et al., 2007a; Ultra et al., 2007b; Vetterlein et al., 2007). A potential explanation for this observation is the fact that many plants, similar to microorganisms (Bhattacharjee and Rosen, 2007), are able to detoxify absorbed As^{V} via intracellular As^{V} reduction and subsequent release of As^{III} (As^{III} efflux) into the surrounding medium (Xu et al., 2007; Zhao et al., 2009; Meadows, 2014). The aquaporin Lsi1 (OsNIP2;1) has been identified to mediate As^{III} efflux in rice roots via facilitated diffusion (Ma et al., 2008; Zhao et al., 2010). Besides Lsi1, other plant aquaporins can transport As^{III} bi-directionally across the plasmalemma and thus may be involved in As^{III} efflux (Bienert et al., 2008; Ali et al., 2009). However, As^{III} efflux might also occur through energy-dependent, active transporters. The expression of the *P. vittata* As^{III} antiporter PvACR3 in *Arabidopsis thaliana* increased As^{III} root efflux and enhanced As tolerance (Chen et al., 2013), indicating that As^{III} efflux confers As detoxification on plants. Although released As^{III} can be readily re-absorbed by roots, continuous As^{III} efflux into the rhizosphere limits the cellular As burden in roots and, hence, reduces As phytotoxic effects (Zhao et al., 2009).

Compared to non As-accumulator plants, *P. vittata* is thought to exhibit low As^{III} efflux into the surrounding medium due to its highly efficient As^{III} xylem loading system (Su et al., 2008; Huang et al., 2011). Nonetheless, substantial As^{III} efflux from *P. vittata* roots has been measured recently, when *P. vittata* was grown on sterile agar media, containing highly elevated As^{V} concentrations of up to 37.5 mg As^{V} L^{-1} (Chen et al., 2016; Han et al., 2016). While,

similar to the results of previous studies (Su et al., 2008; Huang et al., 2011), little As^{III} release was observed at low As^{V} concentrations in the growth media (0.75 mg As^{V} L^{-1}), As^{III} release increased exponentially if roots were exposed to high As^{V}-concentrations (>15 mg As^{V} L^{-1}). These results suggest that As^{III} efflux may thus be an important mechanism for As detoxification in *P. vittata* when grown at high As^{V} substrate concentrations (Chen et al., 2016; Han et al., 2016). However, since the studies were conducted under sterile, hydroponic conditions and at labile As^{V} concentrations which are unlikely to occur in natural soil systems (Wenzel et al., 2002), some of the proposed findings may have limited validity for enhancing our understanding of As fluxes in the rhizosphere of soil-grown *P. vittata* specimen (Fitz and Wenzel, 2002).

In addition to root efflux, increased labile As^{III} and As^{V} in the rhizosphere may also result from efficient As mobilization through root exudates, microorganisms and fungi. *P. vittata* inhabits aerobic, calcareous soils with neutral to moderately alkaline pH (Jones, 1987; Lessl and Ma, 2013) where the phytoavailability of essential nutrients such as P, Mn, and Fe is typically low (Sparks, 2003). Physiological adaptations of plants to improve their nutrient uptake, such as root exudation of dissolved organic carbon (DOC) compounds (e.g. low-molecular-weight-organic-anions (LMWOAs)) or local acidification of the rhizosphere soil (Hinsinger, 2001), can concomitantly increase As mobility in the rhizosphere via ligand- and/or proton-promoted co-dissolution of As and Fe (oxyhydr)oxides (Fitz and Wenzel, 2002; Fitz et al., 2003; Vetterlein et al., 2007). Indeed, evidence is mounting that *P. vittata* uses similar mobilization mechanisms, as indicated by strong correlations of enhanced DOC concentrations with dissolved As, P and Fe in rhizosphere soil solutions (Fitz et al., 2003; Tu et al., 2004; Gonzaga et al., 2009; Das et al., 2017). Apart from root exudates, As-resistant rhizobacteria of *P. vittata* have been identified to effectively mobilize As from poorly soluble mineral phases (Ghosh et al., 2011; Han et al., 2017b).

To further elucidate possible As^{III} efflux and As solubilisation mechanisms in the rhizosphere of *P. vittata* grown in As-contaminated soil, it is necessary to investigate the small-scale spatial distribution of As^{III}/As^{V} solute flux alongside their biogeochemically associated elements (e.g. P, Mn, and Fe) and other physico-chemical soil parameters (e.g. O_2) *in situ*.

1.4 High resolution chemical imaging in the rhizosphere

In recent years, methods for the investigation of elemental solute flux in the rhizosphere of terrestrial plants have been developed based on passive, two-dimensional (2D) chemical imaging techniques originating from aquatic biogeochemistry. These novel 2D imaging methods allow to visualize multiple analytes, co-localized, at high spatial (sub-mm) and temporal (min-h) resolution, providing *in situ*, spatially referenced information on biogeochemically important analytes at the bulk soil – rhizosphere – plant root interface (Santner et al., 2015b; Oburger and Schmidt, 2016).

1.4.1 Diffusive gradients in thin films (DGT)

One group of 2D chemical imaging methods is based on the diffusive gradients in thin films (DGT) technique (Davison and Zhang, 1994). As a low-invasive, diffusion based sampling method, DGT uses thin hydrogels impregnated with finely distributed, analyte-selective binding agents to gradually accumulate labile chemical species (i.e., anions and cations) during deployment in aqueous environments (e.g. soil, sediment, water) (Zhang and Davison, 1995).

A standard DGT assembly (Figure 1) for solute sampling consists of a binding gel, overlain by an ion-permeable diffusive gel (i.e., a polyacrylamide hydrogel without binding agent) and covered by a protective membrane filter. This stack is loaded in a DGT piston device with defined dimensions only exposing the membrane to the probed phase (Zhang and Davison, 1995). During DGT deployment, solutes diffuse through the membrane and diffusive gel towards the surface of the binding gel where the target analytes are rapidly bound. The effective concentration of the target analytes at the interface of the binding gel and diffusive gel remain “zero”, establishing a steep concentration gradient towards the probed phase, thus inducing continuous diffusive flux of solutes towards the DGT binding gel (Degryse et al., 2009). Post DGT sampling, piston samplers are disassembled, the binding gels (binding layers) retrieved and the accumulated mass of analyte in the binding layer is determined. Because the analyte accumulation follows Fick’s first law of diffusion (Zhang and Davison, 1995), the time-averaged solute flux into the binding layer, f_{DGT} (Eq. 1), and time-averaged concentrations at the interface of the DGT device and the probed phase, C_{DGT} (Eq. 2), can be calculated using Eq. 1 and Eq.2, respectively. Here, M denotes the mass of analyte accumulated in the binding layer, Δg the length of the diffusive path (e.g. diffusive gel and membrane filter), D the analyte-

specific diffusion coefficient in the diffusion gel at a certain temperature, A the area exposed to the probed phase, and t the duration of deployment (Davison and Zhang, 1994).

$$f_{DGT} = \frac{M}{At} \quad \text{(Eq. 1)}$$

$$C_{DGT} = \frac{M\Delta g}{DAt} \quad \text{(Eq. 2)}$$

When applied in soils, the mass of analyte accumulated in the binding layer upon deployment reflects the potentially labile analyte concentration in the soil porewater, its rate of diffusion through the soil porewater, and the kinetics of analyte desorption from the soil solid phase (Zhang et al., 2001; Lehto et al., 2006). Thus, under conditions of diffusion limitation, DGT may sample a similar elemental pool as plant roots. This hypothesis is supported by several studies showing strong correlations between element concentrations in plants and those sampled by DGT deployed in the corresponding soil (Zhang et al., 2001; Zhang et al., 2004; Nolan et al., 2005; Wang et al., 2014).

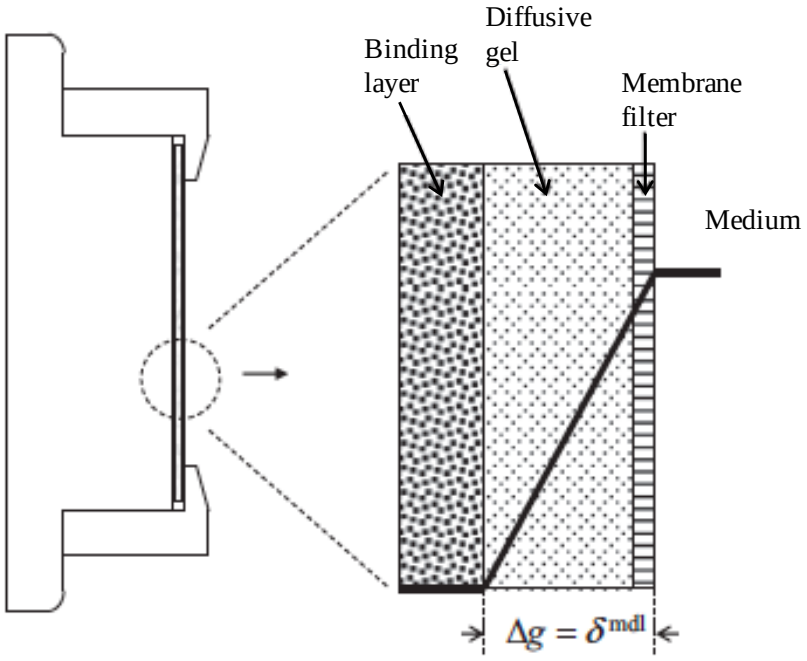

Figure 1: Schematic of a standard DGT assembly in a piston sampler. The exploded view shows the binding layer, diffusive gel and protective membrane filter. The solid line in the exploded view shows the concentration gradient of an analyte diffusing from the probed phase (medium) into the DGT gel (binding layer). Adapted from Davison and Zhang (2016).

Besides its use for bulk sample analyses (Figure 1), DGT can be exploited for 2D chemical imaging to map the spatial (sub-mm) distribution of labile chemical species in plant rhizospheres (Santner et al., 2015b; Santner and Williams, 2016; Oburger and Schmidt, 2016). To map the flux of solutes at sub-mm scale, binding agents used in the DGT binding gel must be homogeneously distributed and of fine particle size (<10 μm) (Santner et al., 2015b). Furthermore, Δg is minimized by removing the diffusive gel from the gel stack to reduce image blurring by lateral solute diffusion in the diffusive layer (Santner et al., 2015a). Thus, for chemical mapping, labile solutes bind directly to the DGT binding gel surface after rapid diffusion through a thin membrane filter only, protecting roots and rhizosphere soil in the region of interest (ROI) from physical damage (Kreuzeder et al., 2013).

With the ability to analyze multiple analytes simultaneously, laser ablation inductively coupled plasma mass spectrometry (LA-ICP-MS) has become the analytical method of choice to convert the spatial information saved in loaded DGT gels into 2D high resolution chemical images (Santner and Williams, 2016). For DGT–LA-ICP-MS analysis, loaded DGT gels are introduced into the sample ablation cell of a LA system coupled to an ICP-MS instrument. The laser beam is focused on the planar DGT gel surface and subsequently ablates the DGT gel surface line-by-line (raster scan). The laser-ablated, analyte-carrying aerosols are transferred via a closed gas stream (e.g. Ar, He) into the plasma of a connected ICP-MS, which is set to a continuous scan for the target isotopes according to their mass-to-charge (m/z) ratio. Post scanning, the recorded ICP-MS signals can be translated into a spatially resolved data matrix for each analyte and signals can be calibrated by applying an external calibration function derived from matrix matched DGT–LA-ICP-MS standard series with known elemental concentrations. Finally, the calibrated data matrix can be visualized as a 2D contour plot by assigning a false color scale to the measured values, thus representing a chemical image (Höfer, 2017).

The simultaneous application of different DGT gels as a dual-layer DGT stack is a promising approach for obtaining concomitant chemical images of analytes that cannot be sampled by application of a single DGT binding gel; however, only few researchers have used this approach so far (Santner and Williams, 2016). Recently, urethane-based, ultra-thin (~100 μm) and physically stable DGT gels have been developed that greatly facilitate the generation of high resolution chemical images from such dual-layer DGT approaches (Kreuzeder et al., 2013).

Thus, many DGT combinations for 2D chemical imaging have become possible, enabling e.g. *in situ* speciation of soluble inorganic As in environmental media (Bennett et al., 2011).

1.4.2 Planar optode sensors (PO)

Another group of 2D chemical imaging methods comprises planar optical sensor membranes (planar optodes) that are capable of real-time measurement of the spatial distribution of analytes at µm-scale (Gansert and Blossfeld, 2008). The first planar optode (PO) was introduced for 2D measurement of the O_2 distribution in freshwater ecosystems (Glud et al., 1996). More recently, POs have also been adapted for rhizosphere research, where they have been successfully applied to visualize spatio-temporal distributions of O_2, NH_4^+, pCO_2, and pH (Blossfeld and Gansert, 2012; Santner et al., 2015b; Oburger and Schmidt, 2016).

The measuring principle of PO sensors relies on changes in photoluminescence (fluorescence or phosphorescence) corresponding to the analyte concentration (Santner et al., 2015b). Common and cost-effective PO setups used for 2D imaging in the rhizosphere are based on a RGB-color ratiometric imaging approach (Larsen et al., 2011; Hoefer et al., 2015). Here, the PO sensors consist of a reversible, analyte-sensitive fluorescence indicator (luminophore) and an analyte-independent reference/antenna dye homogeneously incorporated in an analyte-permeable matrix that is coated as thin film onto a support material (e.g. a polyester foil) (Santner et al., 2015b). These PO foils can then be applied to the ROI in the rhizosphere. The analyte sensing follows initial excitation of the luminophore using e.g. high-power light-emitting diodes (LEDs). Subsequent to excitation, the luminophore returns back to its ground state (de-excitation) and concomitantly emits energy (photons) in relation to the analyte concentration. The emission intensity of the analyte specific luminophore and reference dye is then measured using a e.g. digital single-lens reflex (DSLR) camera which allows for simultaneous recording of three different color spectra (red, green, and blue). Subsequently, the intensity ratio between individual color spectra can be calculated and, upon external calibration, assigned to the analyte concentration in the ROI (Santner et al., 2015b). Recently developed combinations of PO sensors with DGT gels allow for the simultaneous imaging of anionic and/or cationic solutes and physico-chemical soil parameters (e.g. pH, O_2) in parallel (at different ROIs) (Hoefer et al., 2015), and in the same place (at identical ROIs) (Stahl et al., 2012; Guan et al., 2015; Williams et al., 2014; Hoefer et al., 2017; Han et al., 2017a).

2 HYPOTHESIS

The aim of this study was to elucidate the spatial distribution of soluble inorganic As species (i.e., As^{III} and As^{V}), their biogeochemically associated solutes (i.e., P, Mn, Fe), and molecular oxygen (O_2) in rhizosphere and bulk soil of *P. vittata* and *P. quadriaurita* grown in highly As-contaminated soil using a rhizotron experiment.

The hypothesis comprises, that efficient As^{V} uptake by both As-hyperaccumulating ferns may lead to distinct depletion of DGT-available As^{V} in the direct vicinity of individual roots concurrently to root-induced As solubilisation from Fe (oxyhydr)oxide sorbent phases. Recently, it was shown under hydroponic, sterile conditions that *P. vittata* roots may exude substantial amounts of As^{III} if grown in media containing >15 mg As L^{-1} (Chen et al., 2016). Therefore, we further tested the hypothesis that (i) excess As^{III} concentrations may be found in the rhizosphere of soil-grown specimen of both hyperaccumulator ferns, and that (ii) As^{III} released into the rhizosphere will be quickly re-oxidized to As^{V} leading to co-localized spatial patterns of As and simultaneously of elements involved in the redox chemistry of As.

The main objectives of this study included:

- to apply a dual-layer diffusive gradients in thin films (DGT) method that allows for low-invasive, semi-quantitative, and co-localized inorganic As^{III}/As^{V} speciation at high spatial (sub-mm) resolution in the rhizosphere of ferns;
- to investigate the spatial (sub-mm) distribution of As^{III}, As^{V}, P, Mn and Fe fluxes in the rhizosphere of *P. vittata* and *P. quadriaurita* and bulk soil;
- to monitor spatio-temporal O_2 dynamics in rhizosphere vs. bulk soil using planar optodes (POs);
- to explore the effects of As sorption and redox transformation mediated by Mn and Fe (oxyhydr)oxides along individual roots and plant uptake by As-hyperaccumulating ferns.

3 MATERIAL AND METHODS

3.1 Laboratory procedures

The experimental work was conducted in the laboratory and greenhouse facilities of the Institute of Soil Research, University of Natural Resources and Life Sciences Vienna, Universitäts- und Forschungszentrum Campus Tulln, Austria. Laboratory water type 1 (≤0.055 µS cm^{-1}, TKA-GenPure, Thermo Electron LED GmbH, Niederelbert, Germany) was used for laboratory procedures and solution preparation. If not stated otherwise, glass- and plasticware was acid-cleaned by immersion for 24 hours in 5% HNO_3 (v/v) and rinsed three times with lab water type 1 prior use. All chemical reagents used in this work were of p.a. grade and supplied by Alfa Aesar (Karlsruhe, Germany), Sigma-Aldrich (Vienna, Austria), Merck (Vienna, Austria) or VWR (Vienna, Austria). DGT gel and PO film coating and handling was carried out in a biological class II laminar flow bench (Clean Air, EuroFlow EF/S, Telstar Laboratory Equipment B.V., Woerden, The Netherlands). Samples for liquid ICP-MS analysis featured a ~2% HNO_3 (w/w) matrix. LA-ICP-MS analysis of the DGT gels was performed in a class 100,000 cleanroom. All analytical instruments were checked for daily performance and calibrated prior use.

3.2 Experimental soil

We collected the upper B horizon of a Calcaric Cambisol (IUSS Working Group WRB, 2015) in September 2015 near St. Margarethen, Carinthia, Austria. This soil (Forst99) was used in previous studies (Lombi et al., 2000; Wenzel et al., 2002; Fitz et al., 2003) and is characterized by a moderately alkaline pH (H_2O) of 7.97 and highly elevated total (*aqua regia* extractable) As concentrations of 2080 ± 18.1 mg kg^{-1}. Increased soil As concentrations were caused by weathering of the rare primary As mineral arseniosiderite ($Ca_2Fe_3(AsO_4)_3O_2 \cdot 3(H_2O)$) (Lombi et al., 2000). The non-specifically bound As concentration, defined here as 0.05 mol L^{-1} $(NH_4)_2SO_4$ extractable As (Wenzel et al., 2001), was determined at 6.77 ± 0.12 mg kg^{-1}. In this soil, As in the soil solid phase was strongly associated with abundant Fe(III) (oxyhydr)oxides (Lombi et al., 2000). After sampling, the soil was air dried, sieved (<2 mm) and characterized for its physico-chemical properties (Table 1).

Table 1: Selected physico-chemical properties of the experimental soil (Forst99).

Parameter	Unit	Value	±	SD[a]	Method
Texture[b]	-	Sandy loam			n.a.
Clay[b]	g kg^{-1}	190	±	n.a.	n.a.
CEC[b,c]	mmol kg^{-1}	334	±	n.a.	n.a.
MWHC[d]	g kg^{-1}	706	±	39.0	saturated soil paste (n = 4)
pH (H_2O)	-	7.97	±	0.04	ÖNORM L 1083 (n = 3)
pH ($CaCl_2$)	-	7.38	±	0.02	ÖNORM L 1083 (n = 3)
pH	-	7.87	±	0.15	saturated soil paste (n = 4)
EC[e]	µS cm^{-1}	460	±	27.8	saturated soil paste (n = 4)
$CaCO_3$	g kg^{-1}	135	±	15.5	ÖNORM L 1084 (n = 3)
Total C	g kg^{-1}	67.9	±	n.a.	ÖNORM L 1080 (n = 2)
Total N	g kg^{-1}	3.08	±	n.a.	dry combustion (n = 2)
DOC[f]	mg kg^{-1}	211	±	16.4	dry combustion (n = 4)

		element concentrations in soil extract								
		total (*aqua regia*) (n=4)			H_2O (n=4)			0.05M $(NH_4)_2SO_4$ (n=4)		
As	mg kg^{-1}	2080	±	18.1	5.28	±	0.03	6.77	±	0.12
P	mg kg^{-1}	1120	±	77.6	0.81	±	0.14	n.a.	±	n.a.
Mn	mg kg^{-1}	1420	±	17.6	0.65	±	0.02	0.64	±	0.07
Fe	mg kg^{-1}	53,700	±	0.53	9.21	±	0.05	19.1	±	0.41
Al	mg kg^{-1}	64,300	±	1.16	13.4	±	0.88	4.63	±	0.90

[a] Standard deviation
[b] Fitz et al. (2003)
[c] cation exchange capacity
[d] maximum water holding capacity
[e] electrical conductivity
[f] dissolved organic carbon

3.2.1 Soil characterization

The Forst99 soil was analyzed for total carbon (C) and nitrogen (N), $CaCO_3$ content, H_2O-extractable element concentrations, total (*aqua regia* extractable) element concentrations and pH, following Austrian standard methods compiled in Blum et al. (1996).

For measuring the maximum water holding capacity (MWHC), a saturated soil paste was prepared by gradually adding water to a batch of air-dried soil in a beaker and stirring the soil-water mixture with a spatula (Rhoades, 1982). At saturation, the soil paste glistened and slid freely and cleanly off the spatula. We then allowed the saturated soil paste to sit for ~4 h,

before determining its water content gravimetrically by drying a subsample at 105 °C (UFE 600, Memmert GmbH + Co. KG, Schwabach, Germany). The MWHC was calculated as the ratio between water content and oven-dry weight (dwt) of the soil paste.

For determining the electrical conductivity (EC), another subsample of the prepared soil paste (~10 g) was centrifuged for 10 min at 15,300 × g. The EC of the obtained supernatant was measured using an EC meter (inoLab® Terminal 740, WTW, Weilheim, Germany).

Dissolved organic carbon (DOC) in H_2O extract (SSR of 1:10 (w/v)) was measured using a vario TOC cube (Elementar Analysensysteme GmbH, Langenselbold, Germany) after pre-treating the sample with 10% HCl (w/w) to remove carbonates.

To identify the non-specifically bound As fraction, the soil was extracted using 0.05 mol L^{-1} $(NH_4)_2SO_4$ at a SSR of 1:25 (w/v) by 4 h end-over-end shaking at 20 °C (Wenzel et al., 2001).

Data on soil texture, clay content and cation exchange capacity (CEC) were inherited from Fitz et al. (2003), as all analyzed soil properties were still in well accordance with previous measurements.

All extractions, digestions and measurements were performed using well homogenized, air-dried, and sieved soil (<2 mm). For quality management, blanks and in-house reference material were included in all extraction and digestion procedures. Extracts which could not be immediately analyzed were either frozen at -20 °C or acidified with ~10% HNO_3 (w/w) to reach a final matrix of ~2% HNO_3 (w/w). Element concentrations in extracts were measured on Optima 8300 (Perkin Elmer, Waltham, USA) ICP-OES, and Elan 9000 DRCe (Perkin Elmer, Waltham, USA) and Thermo Fisher ELEMENT XR (Thermo Fisher Scientific, Bremen, Germany) ICP-MS.

3.3 Experimental plants

Two hyperaccumulator plant species of the *Pteris* genus of ferns, *Pteris vittata* L. and *Pteris quadriaurita* var. *tricolor*, with different As acquisition efficiency were used in this study. Young *P. vittata* sporophytes with about four fronds were obtained from ARC Ferns LLC, Apopka, Florida, USA. Prior shipping, *P. vittata* was treated with a spray application of 0.1498 g L^{-1} cyfluthrin to meet phytosanitary requirements. Their counterparts, young *P. quadriaurita* var. *tricolor* specimens, were purchased from Der Palmenmann®, Castrop Rauxel, Germany.

Compared to *P. vittata*, *P. quadriaurita* Retz. has been reported to concentrate much less As, however up to 2823 mg As kg^{-1} in its fronds were found when grown in a soil spiked with 100 mg As kg^{-1} for 45 days (Srivastava et al., 2006). The commercial variety *P. quadriaurita* var. *tricolor* has not been used in experimental setups up until now.

Upon arrival, *P. vittata* and *P. quadriaurita* were pre-grown in commercially available potting substrate for 22 and 46 days, respectively, to ensure plant vitality and sufficient root development. Out of a pool of ~40 fern specimen per species, we selected six homogeneously grown individuals each for the rhizotron experiment. Approximately two weeks before the start of the experiment, both fern species were sprayed twice with a thiacloprid-based insecticide (Calypso®, Bayer AG, Leverkusen, Germany) to eliminate any possible pests.

3.4 DGT gel and LA-ICP-MS standard preparation

3.4.1 DGT gel fabrication

The presented procedure of fabricating As^{III}-selective DGT gels based on using mercapto-silica binding resin is a modification of the method reported by Bennett et al. (2011). The originally used bisacrylamide-cross-linked polyacrylamide gel matrix where the 3-mercaptopropyl-functionalized silica resin is embedded, was replaced with an ether-based polyurethane hydrogel material (Hydromed-D4, AdvanSource biomaterials, Massachusetts, USA) (Kreuzeder et al., 2013) to overcome problems arising from the high fragility of polyacrylamide-based gels. In addition to the high physical stability, Hydromed-D4 allows the fabrication of ultra-thin (100 µm-thin) hydrogels which is critical for 2D chemical imaging applications. The modified mercapto-silica DGT gel is referred to as “mercapto silica gel” (MSG) throughout this thesis.

To fabricate a MSG gel, a batch of 3-mercaptopropyl-functionalized silica resin (200-400 mesh; Sigma-Aldrich) was finely ground in a ball mill (~20 Hz for 2×5 min; MM 200, Retsch GmbH, Haan, Germany) using polytetrafluoroethylene (PTFE) grinding balls and jars. Milling reduced the original bead size of the resin and ensured homogenous distribution of binding sites in the hydrogel matrix.

For MSG gel preparation, 0.4 g of milled mercapto-silica resin were suspended in 2 mL of water (1:5, w/v) in a 20 mL polypropylene (PP) container. The suspension was vigorously shaken by hand and subsequently dispersed using an ultrasonic bath (RK510, Bandelin Sonorex, Berlin,

Germany) for 10 min. Prior, the hydrogel matrix was prepared by dissolving 8 g of crushed Hydromed-D4 (~5 mm pieces) in 80 mL of a 10:1 ethanol:water solution (v/v) (Kreuzeder et al., 2013). Approximately 18 mL of Hydromed-D4 solution were added to top up to a total of 20 mL of the final mercapto-silica–Hydromed-D4 cocktail. The cocktail was homogenized by vigorous shaking (~3 min) and then fixed on an end-over-end shaker, overnight at 2–3 rpm (revolutions per minute) to remove air bubbles from the viscous gel cocktail.

The MSG coating procedure was performed according to established protocols (Kreuzeder et al., 2013; Hoefer et al., 2017). Briefly, three layers of bubble-free gel solution were knife-coated (Spaltrakel PA5561, BYK-Gardner GmbH, Geretsried, Germany) onto a pristine glass plate (~18 × 24 cm) which was equipped with a 0.25 mm-thick, U-shaped plastic spacer (~10 × 20 cm). After each individual layer, the plate was immediately transferred into an oven (UNE 200, Memmert GmbH + Co. KG, Schwabach, Germany) at 60 °C for complete solvent evaporation. The spacer was removed and the outer ~2 cm of the gel sheet were cut off to remove visible gel inhomogeneities. The finished, triple coated gel including the glass plate was then immersed in ~5 L of water for at least 2 h. Subsequently, the gel was gently detached from the glass plate using plastic tweezers and allowed to fully hydrate for 24 h (water was changed 2–3 times during this period). Following this procedure, a ~100 µm-thin As^{III}-selective MSG with highly homogenous distribution of binding phases was fabricated.

Fabrication of ~100 µm-thin anion and cation mixed binding gels (MBG) was conducted according to Kreuzeder et al. (2013). The MBGs were also urethane-based (Hydromed-D4), and contained a mixture of suspended particulate reagent-iminodiacetate (SPR-IDA; CETAC Technologies, Nebraska, USA), a well-studied binding agent for cationic solutes (Warnken et al., 2004b; Kreuzeder et al., 2013), and zirconium-hydroxide precipitate (ZrOH), a binding agent for labile oxyanions (Kreuzeder et al., 2013; Sun et al., 2014; Guan et al., 2015; Ding et al., 2016).

For gel cutting, a custom-made circular stainless-steel cutter (diameter of 2.4 cm) or PTFE-coated razor blades were used to cut MSG and MBG gels into circular shape for standard DGT piston based samplers or into rectangular shape for the *in situ* deployment in the rhizosphere (chemical imaging). Until usage, MSG and MBG were stored in the dark at 4 °C in PP vials containing lab water type 1 and 0.01 mol L^{-1} $NaNO_3$ (>99%, Sigma-Aldrich), respectively.

Agarose-cross-linked polyacrylamide diffusive gels (thickness of 0.8 mm) needed for DGT–LA-ICP-MS standard production were prepared according to Zhang and Davison (1995).

3.4.2 DGT–LA-ICP-MS standard preparation

To prepare matrix-matched As^{III} and As^{V} calibration standards for LA-ICP-MS, MSG and MBG gels were loaded in standard DGT piston samplers and immersed in quadruplicates into solutions at alternating concentrations of the target analytes and different deployment times as previously reported (Warnken et al., 2004a; Kreuzeder et al., 2013; Hoefer et al., 2015; Hoefer et al., 2017). Some of the Al^{3+}, Ca^{2+}, Cu^{2+}, Fe^{2+}, Mn^{2+}, and PO_4^{3-} multi elemental MBG standards were obtained from Mag. Dr. Andreas Kreuzeder.

The DGT piston samplers (DGT Research Limited, Lancaster, UK) were assembled by stacking a 0.40 mm plastic spacer, a 100 µm resin gel (MSG or MBG), a 0.80 mm diffusive gel, and a 0.14 mm hydrophilic membrane filter (pore size: 0.45 µm, Sartorius AG, Göttingen, Germany) on top of each other in each piston sampler. For the deployment of the DGT samplers, As^{III} and As^{V} stock solutions were prepared by dissolving sodium salts of arsenous acid ($AsNaO_2$; ≥90%, Sigma-Aldrich) and arsenic acid ($Na_2HAsO_4{\cdot}7(H_2O)$; 98-102%, Alfa Aesar) to reach stock solution concentrations of 698 and 610 mg As L^{-1}, respectively. Both stock solutions were used to prepare 3 L of single element solutions containing either varying As^{III} (243, 3,638 and 6,985 µg L^{-1}) or As^{V} (102 and 610 µg L^{-1}) concentrations. A background electrolyte (1 mmol L^{-1} $NaNO_3$) and 5-10 mmol L^{-1} MES buffer at pH ~5.6, which was adjusted using 0.1 mol L^{-1} NaOH (≥97%, Merck), was added. The deployment solutions were well-stirred at ~640 rpm using magnetic stirrers, and left for equilibration overnight, prior immersion of the DGT samplers using custom-built DGT mountings. The DGT samplers were retrieved at varying time intervals derived from the targeted DGT loading calculated according to Eq. 2. In total, eight different As^{III}-standards and four different As^{V}-standards were produced. Additionally, eight blanks were included. The immersion solutions were monitored for its analyte concentrations by taking grab samples of each solution at the beginning and at the end of the DGT deployment period.

After retrieval, the DGT samplers were disassembled and the resin gels thoroughly rinsed with water. Per standard, one gel replicate was prepared for LA-ICP-MS calibration. This gel was placed flat onto a stack of 0.45-µm membrane (Supor 450, Pall Corporation, New York, USA) and gel blotting paper (GB005, Whatmann, Maidstone, UK), covered by a PE foil. The assembly

was subsequently desiccated in a vacuum gel drier (Unigeldryer 3545, Laborgeräte and Vertriebs GmbH, Martinsried, Germany) at 50 °C for ~36 h. After drying, the gel was inseparably merged with the 0.45-µm membrane. Dry standard and blank gels were cut in small strips and mounted onto a clean glass plate with double-sided adhesive tape. Until analysis by LA-ICP-MS, the matrix-matched As^{III}- and As^{V}-standard series were covered with a clean PE foil and stored in a PE zipper bag.

The other three replicates per standard and blank gels were acid digested for liquid ICP-MS analysis using double sub-boiled HNO_3 (65%, w/w) and lab water type 1. MSG gels were digested in closed PFA-vessels (Savillex, Eden Prairie, Minnesota, USA) for 120 min at 160 °C using a mixture of HNO_3 (65%, w/w) (EMPARTA, ACS, Merck) and H_2O_2 (30%, w/w) (TraceSELECT Ultra, Fluka, Sigma-Aldrich) (5:1, v/v). Sample preparation of MBG gels was conducted according to Kreuzeder et al. (2013) and based on microwave-assisted acid digestion using a Multiwave 3000 (Anton Paar, Graz, Austria).

MSG and MBG standard and blank gel digests were analyzed for ^{75}As using a Thermo Fisher ELEMENT XR (Thermo Fisher Scientific, Bremen, Germany) ICP-MS with ^{89}Y as an internal standard for MSG gels, and ^{72}Ge as an internal standard for MBG gels. The maximum relative standard deviation (RSD) of internal standard counts across all analytical runs was 6.6%. A certified reference material (CRM) (SPEX CertiPrep, New Jersey, USA) was measured periodically throughout each run and had an average recovery of 99.3 $\pm$ 7.4%. The average ICP-MS limit of detection (LOD) and limit of quantification (LOQ) were calculated as three times and ten times the standard deviation, respectively, of the digested MSG and MBG blank gels (Table 2). All measured sample concentrations were above the calculated LOD and LOQ values.

Table 2: Limit of detection (LOD) and limit of quantification (LOQ) for MSG (As^{III}) and MBG (As^{V}) gel digests.

	liquid ICP-MS (gel digests)	
	LOD **(ng cm^{-2}) (n = 3)**	**LOQ** **(ng cm^{-2}) (n = 3)**
As^{III}	2.37	7.89
As^{V}	0.107	0.358

3.5 Preparation and calibration of the O_2 sensitive PO

3.5.1 O_2 optode fabrication

Oxygen sensitive POs were prepared according to Larsen et al. (2011). The POs were based on the O_2 quenchable luminophore platinum(II)octaethylpor-phyrin (PtOEP) (Frontier Scientific, Logan, Utah, USA) as oxygen indicator and the coumarin Macrolex® fluorescence yellow 10GN (MY) (LANXESS Deutschland GmbH, Cologne, Germany) as internal reference. PtOEP and MY were mixed in a 1/1% (w/w) ratio, respectively, and dissolved in 4% (w/w) polystyrene (Sigma-Aldrich) using chloroform (Sigma-Aldrich) as solvent. Prior to coating, the sensing cocktail was homogenized using magnetic stirrers (650 rpm for ~24 h) and agitated slowly using an end-over-end shaker (2-3 rpm for ~24 h) to eliminate air bubbles.

A dust-free, double-sided adhesive polyester foil (Melinex® 506, 125 µm, Pütz GmbH + Co. Folien KG, Taunusstein, Germany) was placed in a laminar flow bench and equipped with 50 µm-thick spacers fixed by adhesive tape at the longer sides of the foil. The PO was coated in one stroke using a knife-coating device (Spaltrakel PA5561, BYK-Gardner GmbH, Geretsried, Germany), immediately after pipetting ~2 mL bubble-free PO cocktail onto the top end of the foil. The coated support foil (~10 × 15 cm) was transferred without delay into an oven (UNE 200, Memmert GmbH + Co. KG, Schwabach, Germany) at 40 °C for complete solvent evaporation. This procedure resulted in an estimated dry film of the oxygen sensing layer of ~3 µm. The O_2 PO was stored in the dark in a polyethylene (PE) zipper bag containing lab water type 1.

3.5.2 O_2 optode calibration

For calibration of the O_2 sensitive POs, a modified Stern-Volmer equation was used (Eq. 3), expressing the nonlinear dynamic fluorescence intensity response to molecular oxygen according to Klimant et al. (1995).

$$\frac{R}{R_0} = \left[\alpha + (1-\alpha)\left(\frac{1}{1+K_{sv}\times C}\right)\right] \quad \text{(Eq. 3)}$$

In this equation, R denotes the (red-green)/green pixel intensity ratio, R_0 the ratio in the absence of O_2, α the nonquenchable luminescence signal fraction, K_{sv} the Stern-Volmer quenching constant, and C the O_2 concentration.

The calibrations were conducted in a transparent plastic container, equipped with the O_2 PO at the bottom (coated side facing to the solution). The container was covered with a printed photo of the experimental soil to ensure an adequate background signal. For determining R_0 (0% O_2), a solution containing 10 g L^{-1} $Na_2S_2O_4$ (Sigma-Aldrich) was prepared. The O_2 concentration of the solution was continuously measured using an independently calibrated, optical dissolved oxygen sensor (HQ30D flexi, HACH, Loveland, Colorado, USA) at ~23 °C and ambient pressure. Starting from 0% O_2, the O_2 saturation was gradually increased by bubbling air through the solution using an aquarium pump at a constant flow rate. Measurements were taken after every ~10% increase of the O_2 air saturation and average *R* values were calculated from the measured red and green color spectra intensities. After plotting the measured values, Eq. 3 was fitted for K_{SV} and α for each PO individually. For calibration of the O_2 chemical images, the Stern-Volmer equation was rearranged (Eq. 4). Figure 2 shows an example calibration function after curve fitting using Microsoft Excel 2016.

$$C = \frac{R0 - R}{K_{SV} \times (R - R0 \times \alpha)} \qquad \text{(Eq. 4)}$$

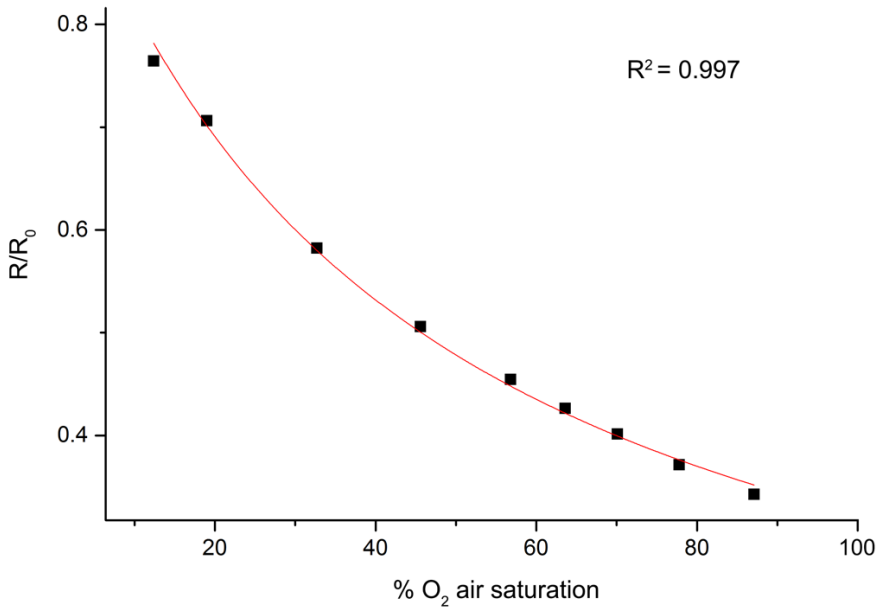

Figure 2: Example calibration curve for one of the planar oxygen optodes used at 23 °C and ambient pressure.

3.6 Rhizotron experiment

A rhizotron experiment was conducted for the *in situ*, high resolution chemical imaging of inorganic As species and other element solutes by DGT. Additionally, POs were applied for mapping of O_2 spatial distribution and temporal flux in the rhizosphere of *P. vittata* and *P. quadriaurita*. The experimental setup was based on previously published procedures for chemical imaging of solutes in plant rhizospheres (Santner et al., 2012; Kreuzeder et al., 2013; Williams et al., 2014; Hoefer et al., 2015; Hoefer et al., 2017).

Here, we used a modified rhizotron assembly after James et al. (1985) (Figure 3). The perspex rhizotron growth containers had inner dimensions of 40 × 10 × 1.5 cm (H × W × D), removable perspex plates on the front side, and 14 irrigation drillings on the back side. The small depth of the rhizotron generally restricts planting of relatively spacious root systems such as well-developed fern rhizomes. Therefore, we equipped the rhizotrons with a custom-built, perspex plant pre-growth box (inner dimensions of H × W × D = 8 × 8 × 8.4 cm), hereafter termed "growth compartment", tightly fitting on top of the rhizotron (Figure 3). The growth compartment was built by Dipl.-Ing. Gottfried Wieshammer (Technisches Büro für Bodenkultur, Vienna, Austria).

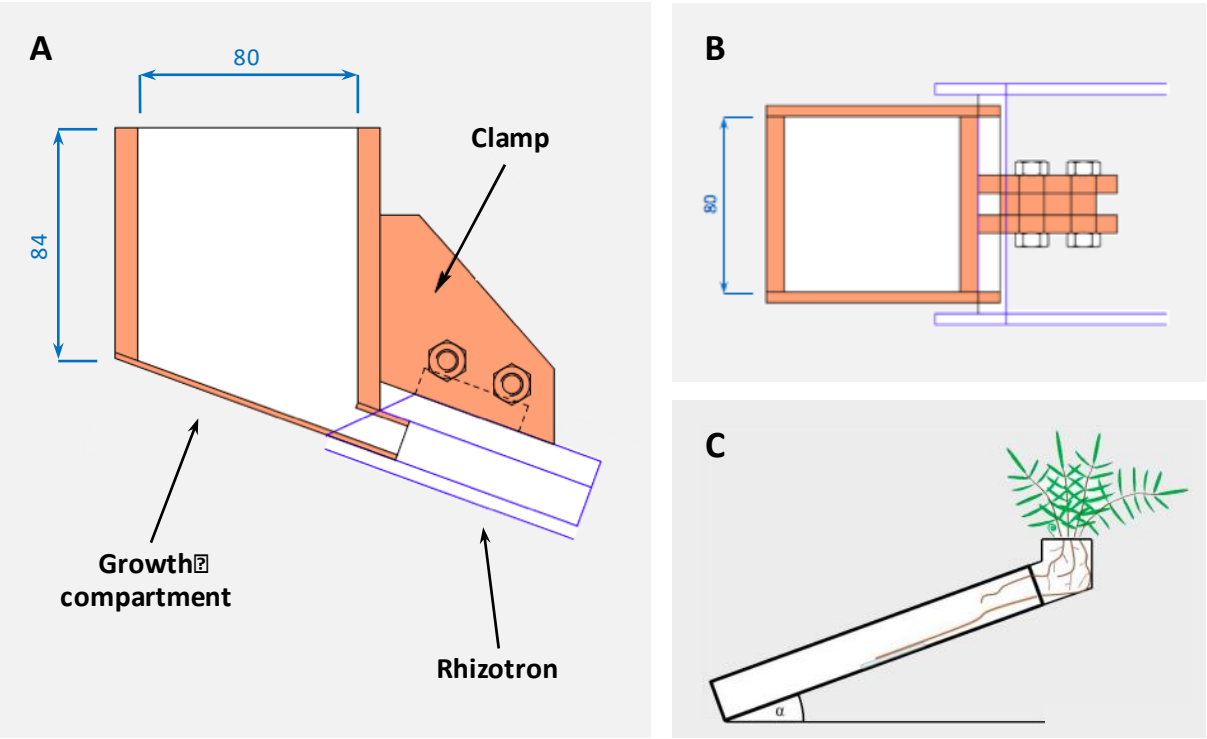

Figure 3: Schematic of a rhizotron plant growth container including growth compartment. (A) Growth compartment connected to the top of the rhizotron. (B) Top view of the growth compartment. (C) Rhizotron

assembly with soil and plant during the growth phase (not to scale). Dimensions are in mm. Technical drawings with courtesy of Dipl.-Ing. Gottfried Wieshammer (Technisches Büro für Bodenkultur, Vienna, Austria).

Twelve rhizotrons were filled with 540 g ± 16 g (dwt) of freshly sieved (<2 mm), pre-moistened Forst99 soil (~36% MWHC) which was equilibrated at ~40% MWHC and room temperature 39 days prior to being filled into rhizotrons. The soil was added layer by layer from the top and carefully compacted with a plastic tamper to achieve a homogenous soil profile with a bulk density of ~0.90 g cm^{-3}. Before closing the rhizotrons, the soil profile was covered with a 50 µm-thin PTFE-foil (Haberkorn, Wolfurt, Austria) overlain by a plastic foil and fixed using adhesive tape. The foils ensured that roots and soil were not disturbed when the front plate was removed for DGT and PO deployment. The rhizotrons were closed by fixing the perspex front plate with two perspex rails which were laterally attached to the rhizotron using screws.

All growth compartments were filled with 543 g ± 5 g (dwt) of pre-moistened Forst99 soil (~40% MWHC) to obtain a bulk density of ~1.00 g cm^{-3}. Prior transfer of the pre-grown ferns into the growth compartments, fern roots were gently rinsed with tap water to wash off any remaining growth substrate. The bottom opening was covered by a thin nylon netting and fixed using adhesive tape. Thereafter, one fern specimen per species was planted into each of six replicate growth compartments and grown until root tips started to reach the opening at the bottom of the growth compartments, ~28 days after planting (DAP). The bottom netting was removed and the growth compartments were connected to the rhizotrons and inclined at ~25-35° to force root development along the removable front plate. During growth, all rhizotrons were wrapped in aluminum foil to protect roots and soil from exposure to light which might have affected the root development and/or induced microphytic growth.

The ferns were grown in a greenhouse chamber with a mean temperature of 20 °C, a photoperiod of 14 h, and an average air humidity of 64%. For soil irrigation, deionized water (≤0.500 µS cm^{-1}, Elix®, Merck KGaA, Darmstadt, Germany) was used and regularly topped up after weighing the rhizotron assembly. Soil in the growth compartments was irrigated from the top by using a PE wash bottle, whereas soil in rhizotrons was irrigated by pipetting water into the 14 irrigation drillings. During the growth period the soil water content in the rhizotron assembly was continuously maintained at ~70% MWHC. We performed DGT sampling and PO sensing at the same time, however at different regions of interest (ROIs), when a dense root

system with multiple roots growing into the rhizotron was developed (Figure 4). In case of *P. vittata*, DGT and POs were applied between 51 and 66 DAP, and in case of *P. quadriaurita* between 65 and 72 DAP.

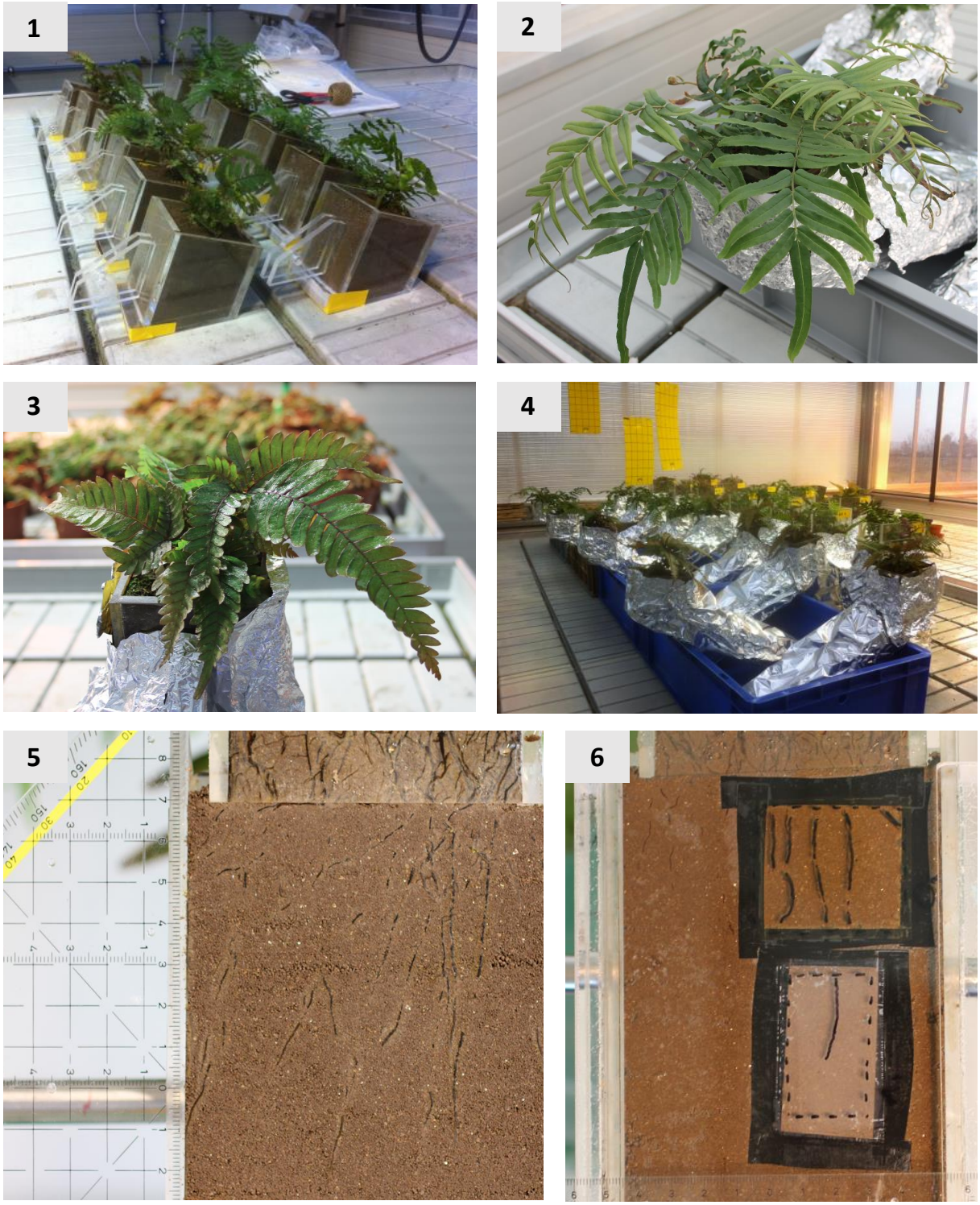

Figure 4: Photographic images showing the rhizotron experiment at different stages. (1) Fern planting in the growth compartment. (2) *P. vittata* in rhizotron RT2 at 45 DAP. (3) *P. quadriaurita* in rhizotron RT7 at 36 DAP. (4) All rhizotrons of both fern species during the growth phase in the greenhouse. (5) Opened rhizotron with detached front plate showing the homogenous soil profile with embedded fern roots prior to DGT and PO

application. (6) Closed rhizotron (RT7) with applied O_2 PO (top) and DGT gels (bottom); black drawings on the front plate indicate the root location.

3.6.1 Co-localized imaging of As^{III}, As^{V}, P, Mn, and Fe using DGT–LA-ICP-MS

Approximately 24 h before DGT and PO application the soil water content in the rhizotrons and growth compartments was increased from the initial ~70% to ~80% MWHC. For DGT and PO application, the rhizotrons were positioned horizontally on a lab bench and the perspex front plates were gently detached, thus only leaving the covering foils on the rhizotron. Subsequently, a clean front plate was placed on the rhizotron, and the rooted ROI marked on the back of the plate. The marked plate was then transferred into a laminar flow bench where MSG and MBG gels were cut into rectangular pieces according to the size of the indicated ROI.

The setup for the DGT sampling of all rhizotrons followed the scheme shown in Figure 5. The MSG and MBG gel pieces were applied as a dual-layer DGT by placing the MSG on top of the MBG at the location of the ROI on the soil-facing side of the front plate. Thereby the MSG served as both, binding layer for As^{III}, and ultra-thin diffusive layer for As^{V} and other elemental solutes. To ensure sufficient contact between DGTs and rhizosphere soil, a 100 µm-thin plastic spacer was added underneath the dual-layer DGT. The gel stack was then covered by a 10 µm-thin, polycarbonate membrane (0.2 µm, Nuclepore Track-Etch Membrane, Whatman, Maidstone, UK) and sealed by waterproof adhesive tape (Scotch Super 88, 3MTM, St. Paul, Minnesota, USA) along all four edges of the membrane. Care was taken to avoid trapping of air bubbles between the stacked gel layers.

At this time, all protective foils were removed from the rhizotron, the exposed soil profile was slightly wetted with lab water type 1 using a spray bottle, photographed, and the front plate including the dual-layer DGT carefully re-mounted. Subsequently the rhizotron was closed firmly and transferred back into the greenhouse at the same growth conditions as stated above.

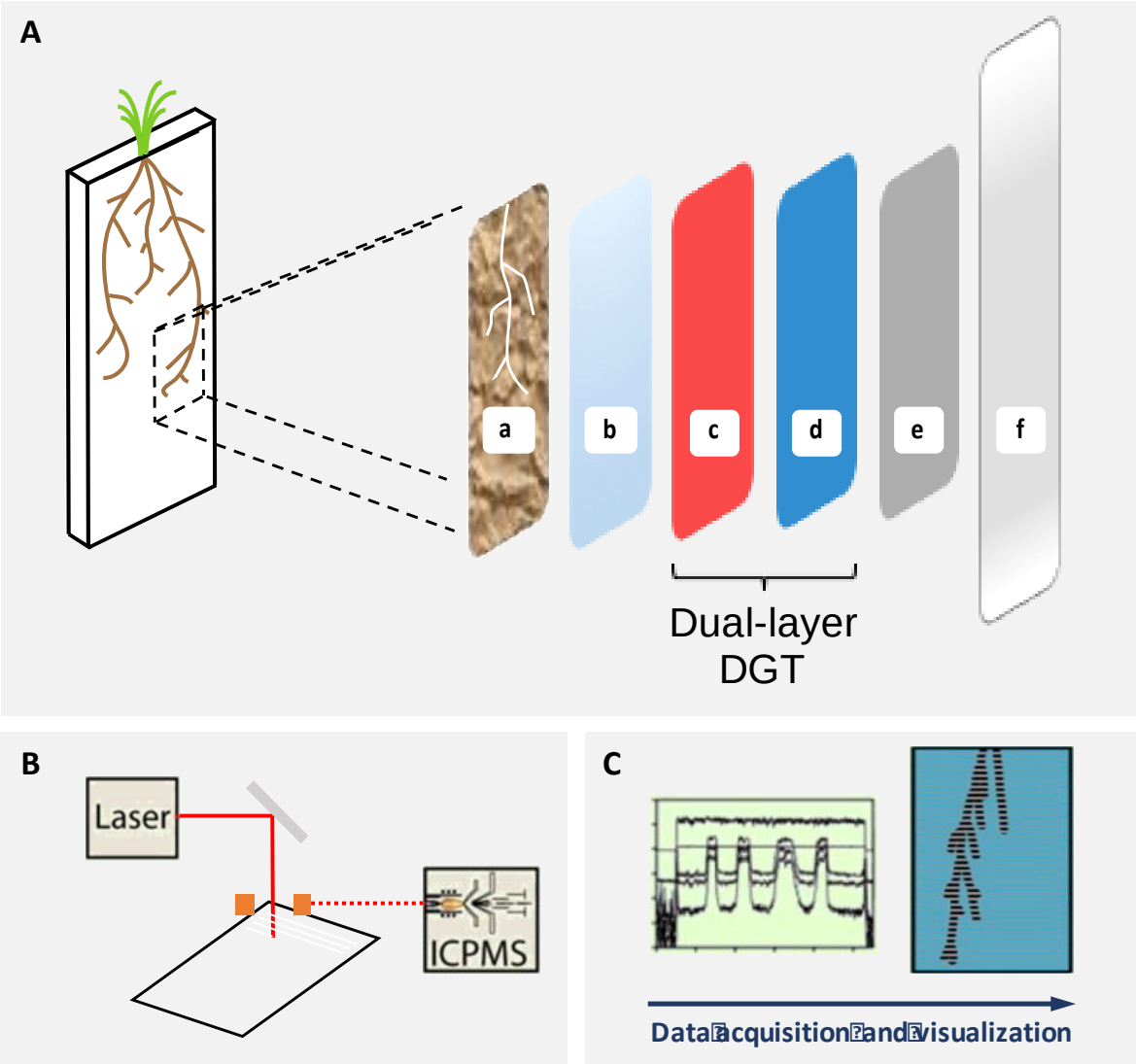

Figure 5: Schematic of the dual-layer DGT chemical imaging experiment and the DGT–LA-ICP-MS setup. (A) Rhizotron and dual-layer DGT deployment showing, (a) region of interest (ROI), (b) Nuclepore membrane filter, (c) As^{III}-selective mercapto silica gel (MSG), (d) mixed binding gel (MBG), (e) 100 µm plastic spacer, (f) removable front plate. (B) Laser ablation of DGT gels and transport of analytes into the ICP-MS instrument. (C) Data acquisition, processing and 2D data visualization in a contour plot. Figures (B) and (C) with courtesy of Dr. Jakob Santner (Division of Agronomy, University of Natural Resources and Life Sciences, Vienna, Austria).

After 24 h of gel deployment, the front plate with the dual-layer DGT was detached from the rhizotron and immediately washed to remove any remaining soil particles using lab water type 1. The front plate was then placed in a laminar flow bench and the polycarbonate membrane overlaying the dual-layer DGT carefully removed. We moistened the DGTs with water, separated the individual gel layers, and dried the MSG and MBG gels, respectively, following the same procedure as described in section 3.4.2. All dried gels, with the side exposed to the ROI facing up, were mounted onto clean glass plates using double-sided adhesive tape.

For laser ablation (LA) of the sample, standard and blank gels, we operated a UP 193-FX (ESI, NWR Division, Portland, USA) excimer LA system in line scanning mode (Kreuzeder et al., 2013; Hoefer et al., 2015; Hoefer et al., 2017). The LA system was coupled to a quadrupole ICP-MS instrument (NexION 350D, Perkin Elmer, Waltham, USA) to scan for ^{13}C, ^{24}Mg, ^{27}Al, ^{31}P, ^{44}Ca, ^{51}V, ^{55}Mn, ^{57}Fe, ^{63}Cu, ^{66}Zn, ^{75}As, ^{98}Mo, ^{114}Cd, and ^{208}Pb signals. LA parameters were set to a beam diameter of 150 µm, interline distance of 400 µm, laser pulse frequency of 20 Hz, and laser energy output of 30%, which equaled a fluence of 1.6–3.0 J cm^{-2}. The maximum scan speed was calculated according to Lear et al. (2012) and set to 250 µm s^{-1}. Laser warm-up time and interline washout delays were set to 10 and 35 s, respectively. Helium was used as carrier gas for analyte transport from the LA cell to the ICP-MS instrument at a flow rate of 0.9 L min^{-1}. The He carrier gas flow was mixed with the nebulizer gas flow (Ar 1.0 L min^{-1}) by a two-way Y-splitter before introduction into the ICP-MS. The ICP-MS scan cycle duration was 0.453 s, which resulted in 8.8 readings mm^{-1} and a total of ~22,000 readings per analyte for an ablated gel area of ~10 cm^2, resulting in a theoretical spatial resolution of 113 × 400 µm. The acquired data was corrected for the gas blank intensity and subsequently normalized by the internal standard ^{13}C to compensate for variations in ablation, transport and ionization efficiency.

Data processing and calculation was carried out in Microsoft Excel 2016 using a custom-built macro written by Dr. Christoph Hoefer (Institute of Soil Research, University of Natural Resources and Life Sciences, Vienna, Austria). After application of the linear calibration functions (µg cm^{-2}), the units were converted to DGT-measured solute fluxes, f_{DGT}, using Eq. 1. For data visualization, the image processing software ImageJ 1.51a (National Institute of Health, Bethesda, Maryland, USA) was used, available free of charge at http://imagej.nih.gov/ij/.

3.6.2 O_2 imaging using PO

Oxygen sensitive POs were deployed concurrently to the deployment of the dual-layer DGTs. Briefly, POs were cut to fit the ROI and fixed on the inside of the removable front plate using waterproof adhesive tape (Scotch Super 88, 3MTM, St. Paul, Minnesota, USA), sensing side facing up (Larsen et al., 2011). PO measurements were performed during the 24 h DGT deployment period. Rhizotrons were transferred from the greenhouse to a dark room and positioned on a horizontal glass pane fixed by a lab stand. One rhizotron replicate (*P. quadriaurita*) was used for an overnight PO measurement sequence, with images taken hourly. Other PO measurements were conducted at varying times however always shortly after the start and at the end of DGT deployment time.

The color ratiometric PO imaging system was similar to the one that was used by Larsen et al. (2011) and Hoefer et al. (2015). The O_2-quenchable fluorophore was excited by six high-power, light-emitting diodes (LEDs; λ peak = 447.5 nm; Royal-Blue, Luxeon, Brantford, Canada) covered by a 475 nm short-pass filter (Edmund Optics GmbH, Karlsruhe, Germany). Images were taken using a digital single-lens reflex (DSLR) camera (Canon EOS 1000D, Canon Inc., Tokyo, Japan) equipped with a macro lens (SIGMA 50 mm F2.8 DG MACRO, Sigma Corporation, Kanagawa, Japan) and a 530 nm long-pass filter (Edmund Optics GmbH, Karlsruhe, Germany) (Figure 6). The Canon EOS 1000D camera has an optical resolution of 10.1 million effective pixels (3888 $\times$ 2592) and was positioned perpendicular to the rhizotron with a lens focus distance to PO surface of ~30 cm. Camera settings were set to ISO: 100, Av: f5.6, and Tv: 1/30 s. The LED assembly was inclined at ~45° relative to the DSLR camera to ensure homogeneous excitation of the O_2 PO and to reduce potential reflections. Excitation LEDs and DSLR camera were synced via a custom-made USB trigger box and controlled with the custom-developed software Look@RGB (http://imaging.fish-n-chips.de/). Images were recorded in triplicate and averaged pixel by pixel to improve the signal to noise ratio. All images were taken in the absence of ambient light. The measured luminescent intensity ratio *R* was determined by image calculation using the ImageJ 1.51a software (National Institute of Health, Bethesda, Maryland, USA). After application of the calibration function (Eq. 4) to calculate C (% O_2), a false color scale was applied to the calibrated PO images to visualize the O_2 distribution in the rhizosphere and bulk soil.

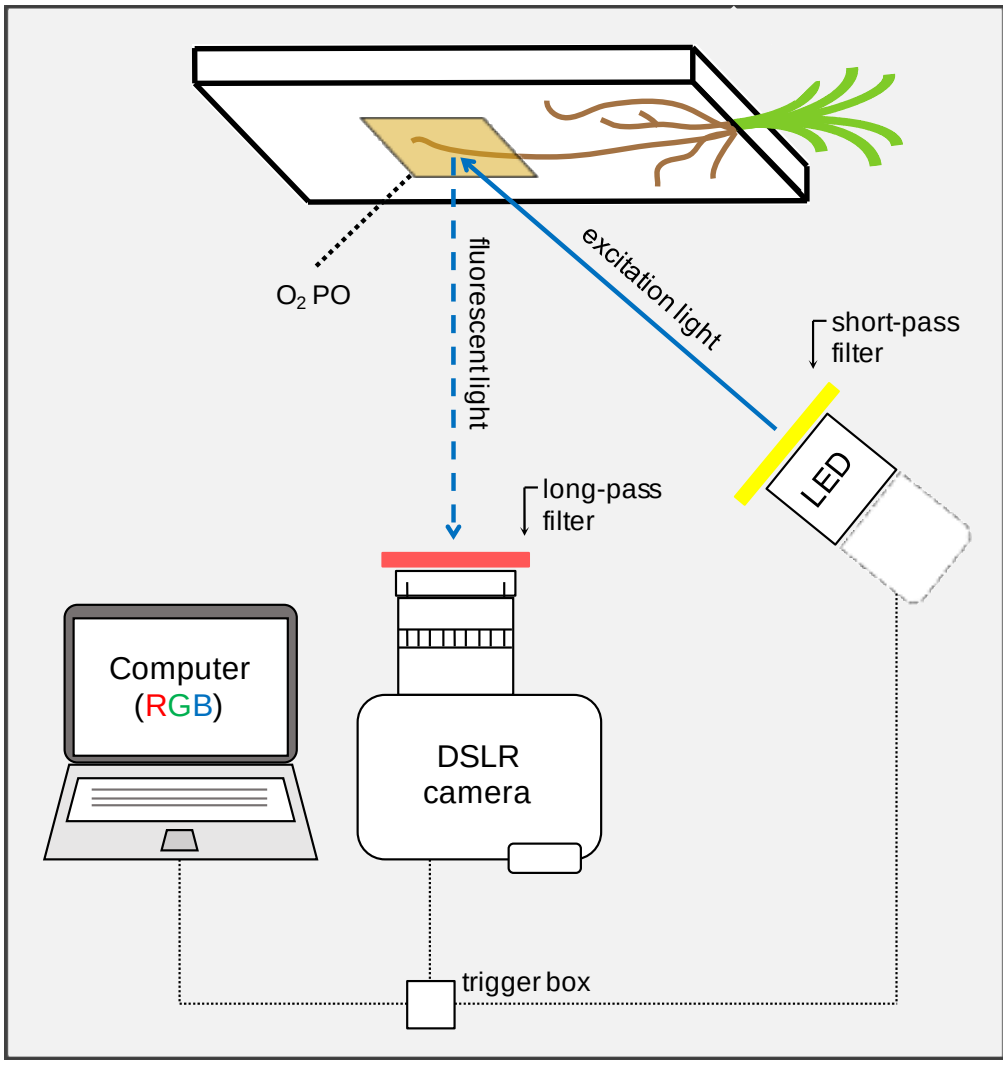

Figure 6: Schematic of the color ratiometric PO setup (not to scale). Excitation LED 447.5 nm; short-pass filter: 475 nm; long-pass filter: 530 nm. Modified after Hoefer et al. (2017).

3.6.3 Plant harvest and biomass analysis

At harvest, between 52 and 67 DAP for *P. vittata*, and 66 and 73 DAP for *P. quadriaurita*, growth and rhizotron compartments were disconnected by cutting developed roots in the transition zone using razor blades. Ferns were cut directly above the soil surface using scissors and separated into roots (including the rhizome) and fronds. Prior to root separation, three soil subsamples were taken from the ROI in the rhizotron to determine the soil water content in the oven (105 °C). Fronds were thoroughly washed with lab water type 1 in a plastic sieve (<2 mm), blotted on tissue paper, and then put into paper bags for oven drying at 65 °C for 72 h (UFE 600, Memmert GmbH + Co. KG, Schwabach, Germany).

The rhizome and roots in the densely rooted growth compartment were separated from soil by repeated washing with tap water in a glass beaker until the water remained clear. Roots in the rhizotron compartment were manually collected using tweezers, gently sieved using a stainless-steel sieve (<2 mm), and thoroughly rinsed with tap water. The washed roots (including the rhizome) were transferred into paper bags and dried at 65 °C for 72 h (UFE 600, Memmert GmbH + Co. KG, Schwabach, Germany).

After recording plant dry biomass, the plant material was finely ground and homogenized using a clean stainless-steel grinder (IKA A11, IKA-Werke® GmbH & Co. KG, Staufen, Germany). Subsamples (0.2 g) of the ground plant material were digested in a mixture HNO_3 (65%, w/w) (EMPARTA, ACS, Merck), H_2O_2 (30%, w/w) (TraceSELECT Ultra, Fluka, Sigma-Aldrich) (5:1, v/v) and a drop of iso-Octanol in open Pyrex tubes using an electrical heating block system (DK Heating Digester, Velp Scientifica, Usmate Velate, Italy). For quality control, three blanks and CRM (Oriental Basma Tobacco Leaves, INCT-OBTL-5, Institute of Nuclear Chemistry and Technology, Warsaw, Poland) was included in each heating block run. The digests were subsequently paper filtered (0.45-µm; Munktell 14/N, Munktell, Bärenstein, Germany), collected in 80-mL PP vials, and diluted with lab water type 1 to reach a 10% (w/w) HNO_3 matrix. Elemental concentrations (^{24}Mg, ^{31}P, ^{39}K, ^{55}Mn, ^{57}Fe, ^{66}Zn, ^{75}As, and ^{98}Mo) of fern digests were measured on ICP-OES (Optima 8300, Perkin Elmer, Waltham, USA) and ICP-MS (Elan 9000 DRCe, Perkin Elmer, Waltham, USA) using ^{115}In as internal standard. During measurement, blanks and CRM (SPEX CertiPrep, New Jersey, USA) was regularly measured to monitor the signal stability of the ICP-OES or ICP-MS, respectively. The CRM recovery was found to be well within 90-110%.

3.6.4 Analysis of arbuscular mycorrhizal root colonization

For screening of potential arbuscular mycorrhization, randomized samples of fresh roots were first cleared by immersion in 10% (w/v) KOH at 60 °C for three days and then stained by boiling at 100 °C in a 5% (v/v) ink (Ink 4001, Pelikan, Schindeleggi, Switzerland)-vinegar solution (Vierheilig et al., 1998). Quantification of the proportion of root length colonized by arbuscular mycorrhizal (AM) fungi was accomplished by using an LED-based light microscope (Eclipse E200-LED, Nikon, Tokyo, Japan) and the magnified intersections method after McGonigle et al. (1990). Images of AM root infections were recorded using a digital camera with 5.0 million effective pixels (2592 × 1944) (VisiCam 5.0, VWR).

4 RESULTS

4.1 Chemical imaging of As^{III}, As^{V}, P, Mn, Fe and O_2 in the rhizosphere

The dual-layer DGT based solute sampling and subsequent LA-ICP-MS analysis of the MSG and MBG gels resulted in datasets of four *P. vittata* (i.e., RT1, RT2, RT3, and RT4) and three *P. quadriaurita* rhizotron replicates (i.e., RT5, RT6, and RT7), respectively. Additional DGT gels deployed in other rhizotron replicates were not analyzed by LA-ICP-MS due to technical complications during gel application (i.e., entrapped air bubbles). In one *P. vittata* (i.e., RT2) and two *P. quadriaurita* rhizotron replicates (i.e., RT5, and RT7) also O_2 sensitive POs were installed to collect PO- parallel to DGT data.

Figures 7 to 16 show the 2D distribution of labile As^{III}, As^{V}, P, Mn, Fe, and O_2 at sub-mm scale around individual roots of *P. vittata* and *P. quadriaurita* grown on Forst99 soil. DGT-measured solute fluxes within individual chemical images were evaluated to identify spatial patterns of As^{III} and As^{V} species along potentially associated solute species. Therefore, graphs were compiled showing horizontal profile plots across selected root sections with single or vertically averaged lines of DGT-measured elemental flux. Similar profile plots were extracted from PO O_2 images. Within all profiles, average DGT-measured fluxes and/or average O_2 air saturation values were calculated, whenever a distinct increase/decrease relative to the corresponding bulk soil signals was measured. If the DGT-measured flux remained unchanged over the whole region of interest (ROI), or problems during gel preparation for LA-ICP-MS analysis occurred (i.e., gel flipping), DGT chemical images were not calibrated but interpreted solely visually.

4.1.1 *Pteris vittata*

<u>Spatial distribution of DGT-labile As^{III} and As^{V} species</u>

The DGT-measured As flux mapped from four *P. vittata* rhizotron replicates clearly showed increased As^{V} flux within soil areas that were unaffected by root activities (bulk soil). These bulk soil As^{V} fluxes ranged between 1.0 in Figure 10 (RT4) and 1.5 pg cm^{-2} s^{-1} in Figure 7 (RT1) (Table 3). Apart from very few randomly distributed, single spot locations of increased DGT-measured As^{III} flux, no As^{III} DGT-flux was mapped in the bulk soil (Table 3).

Table 3: DGT-measured As^{III}, As^{V}, P, and Mn solute fluxes in bulk soil (i.e., soil areas that were unaffected by root activities) of the corresponding ROIs in *P. vittata* and *P. quadriaurita* rhizotron replicates.[1]

Fern species	Rhizotron	DGT-flux in bulk soil[a]			
		As^{III} f_{DGT} (pg cm^{-2} s^{-1})	As^{V} f_{DGT} (pg cm^{-2} s^{-1})	P f_{DGT} (pg cm^{-2} s^{-1})	Mn f_{DGT} (pg cm^{-2} s^{-1})
Pteris vittata	RT1	0.00 ± 0.02	1.49 ± 0.14	5.57 ± 0.58	0.23 ± 0.36
	RT2	0.03 ± 0.04	1.26 ± 0.13	2.01 ± 0.36	0.08 ± 0.04
	RT3	n.a.[b]	1.19 ± 0.08	2.09 ± 0.24	5.97 ± 2.01
	RT4	0.01 ± 0.02	0.96 ± 0.09	1.51 ± 0.31	2.95 ± 0.45
	Average	0.01	1.22	2.79	2.31
	RSD[c]	103%	18%	67%	70%
Pteris quadriaurita	RT5	0.04 ± 0.23[d]	1.73 ± 0.16	1.42 ± 0.42	0.04 ± 0.01
	RT6	0.01 ± 0.09[d]	1.40 ± 0.11	3.46 ± 0.27	0.07 ± 0.03
	RT7	0.07 ± 0.14[d]	1.45 ± 0.21	2.46 ± 0.41	4.84 ± 5.25
	Average	0.04	1.53	2.45	1.65
	RSD[c]	71%	12%	42%	168%

[a] Mean ± standard deviation (SD), n = 750.
[b] The As^{III} image of RT3 (Figure 3) was not calibrated due to problems (i.e., gel flipping) during MSG preparation for LA-ICP-MS analysis.
[c] Relative standard deviation.
[d] RT5 (n = 23,418), RT6 (n = 8661), and RT7 (n = 13,991) As^{III} DGT-fluxes were calculated over the whole ROI.

In contrast, we mapped highly increased As^{III} DGT-flux at the location of the P. *vittata* root, extending up to ~0.5–1.0 mm from the root axis of individual *P. vittata* roots into the adjacent rhizosphere soil. These localized zones of increased As^{III} were evident in all *P. vittata* rhizotron replicates, and occurred as spatially confined As^{III} flux maxima with peak As^{III} DGT-flux of up to 2.5 pg cm^{-2} s^{-1} at the very root surface (Figure 7, RT1).

Exemplarily displayed in the line plot over a root cross section in Figure 7 (RT1, As(b)), the average As^{III} DGT-flux in the zone of increased As^{III} was 0.7 **±** 0.5 pg cm^{-2} s^{-1} (mean ± SD, n = 13) and thus evidently higher when compared to bulk soil (Table 3). Partly, when the root surface was not in direct contact with the dual-layer DGT stack, but covered by a thin soil layer, DGT-labile As^{III} peaks diminished (Figure 7, RT1, As(a)). Similar spatial distribution of DGT-labile

[1] For images showing the selected locations of bulk soil DGT-flux measurements in the ROIs of the respective rhizotrons the reader is referred to the appendix.

As^{III} was observed in Figure 8 (RT2, As(a)), Figure 9 (RT3), and Figure 10 (RT4). While zones of increased As^{III} were highly expressed at the axes of older root parts and in soil areas affected by the activities of multiple roots, only little relative increase was observed at the root apex in Figure 10 (RT4, As(a), As(b)). Here, the average As^{III} DGT-flux at the young root tip was 0.2 **±** 0.1 pg cm^{-2} s^{-1} (n = 102), accounting for a 65% decrease in DGT-labile As^{III} compared to the sub-apical region of the same root.

The DGT-measured As^{V} fluxes showed more complex spatial distribution with merging zones of increased As^{V} and As^{V} depletion extending from the root position both axial and lateral. Zones of elevated As^{V} flux were consistently co-localized with zones of increased As^{III}. The horizontal line plots across the root sections in Figure 7 (RT1, As(b)) and Figure 8 (RT2, As(a)) revealed an average As^{V} DGT-flux in the zone of increased As^{V} of 2.0 **±** 0.3 pg cm^{-2} s^{-1} (RT1; n = 8) and 1.6 **±** 0.2 pg cm^{-2} s^{-1} (RT2; n = 11), equating to a relative increase in As^{V} flux in the rhizosphere of 36% and 30%, respectively, compared to the corresponding bulk soils (Table 3). Peak As^{V} DGT-flux of up to 3.9 pg cm^{-2} s^{-1} was observed at the interface of two roots growing side by side on the top right of the ROI in Figure 9 (RT3). Here, zones of elevated As^{V} fluxes showed the largest spatial expansion and reached up to ~2.0 mm into the rhizosphere soil (Figure 9, As^{V}). Besides these distinct zones of increased As^{V}, slightly elevated DGT-measured As^{V} flux was observed in the immediate vicinity of the apparent root tip in Figure 10 (RT4). The As^{V} images of Figure 7 (RT1) and Figure 9 (RT3, As^{V}), indicate similar patterns of As^{V} solubilisation at the apical root segments.

Substantially decreased As^{V} DGT-flux in Figure 7 (RT1) and Figure 8 (RT2) directly adjacent to the co-localized zones of increased As^{III} and As^{V}, indicate lateral depletion of DGT-labile As^{V} expanding from individual *P. vittata* roots. The plotted root areas in Figure 7 (RT1, As(a)) and Figure 8 (RT2, As(a)), show that the As^{V} DGT-flux in the rhizosphere was depleted down to minimum values of 0.5 and 0.3 pg cm^{-2} s^{-1}. On average, the DGT-measured As^{V} flux in depleted zones (excluding zones of increased As^{V}) was 0.7 ± 0.1 pg cm^{-2} s^{-1} (n = 34) in Figure 7 (RT1, As(a)) and 0.6 ± 0.2 pg cm^{-2} s^{-1} (n = 51) in Figure 8 (RT2, As(b)). This As^{V} depletion accounted for a ~55% decrease compared to the average As^{V} DGT-flux in the corresponding bulk soils (Table 3).

Whereas decreased As^{V} concentrations were detected up to a distance of ~1.5–3.0 mm from the root position in Figure 7 (RT1) and Figure 8 (RT2), only little As^{V} depletion was observed in

the more densely rooted ROI in Figure 9 (RT3) and around the younger root parts in Figure 10 (RT6). The profile plots over the root sections in Figure 7 (RT1, As(b)) and Figure 10 (RT4, As(a), As(b)), visualized slightly lowered As^{V} DGT-flux at the root position.

DGT-measured fluxes of other solutes (P, Mn, Fe, V)

Similar to the spatial distribution of DGT-labile As^{V}, zones of increased P and P depletion were mapped in the *P. vittata* rhizotron replicates. A spatially expanding zone of high DGT-measured P flux confined to the root surface, was only observed in Figure 8 (RT2) and showed generally lower relative increase compared to co-localized zones of high As^{III} and As^{V}. Hotspots, i.e., spatially confined (almost) punctiform increased P DGT-fluxes, were found in all rhizotron replicates. The P image in Figure 9 (RT3) revealed a highly heterogeneous spatial distribution of DGT-measured P flux, with drop-shaped hotspots covering the root tips and partly apical root segments. Two root tips with localized P hotspots are located slightly behind the soil surface at the bottom and on the right hand side of the ROI. On average, the P hotspot at the bottom (corresponding to the peak in Figure 9 (RT3, P)), showed a 1.4-fold increased DGT-measured P flux compared to bulk soil (Table 3). In contrast, the spatial presence of P hotspots in Figure 7 (RT1), Figure 8 (RT2), and Figure 10 (RT4) was limited to isolated micro-niches adjacent to P depletion zones. Similar to the spatial distribution of DGT-labile As^{V}, zones of P depletion were mapped in all *P. vittata* rhizotron replicates. In Figure 8 (RT2, P(a)), lateral depletion of DGT-labile P extended up to ~3.0 mm from the root surface into the rhizosphere lowering the average P DGT-flux in the zone of depletion (excluding zones of increased P) down to 58% compared the bulk soil (Table 3). In Figure 7 (RT1), Figure 9 (RT3), and Figure 10 (RT4), this effect was similar but less pronounced. Note that in Figure 7 (RT1) the average background P DGT-flux in the bulk soil was up to 3-fold compared to the other rhizotron replicates (Table 3).

DGT-measured fluxes of Mn showed high variability among the rhizotron replicates, ranging in bulk soil between relatively low (0.1 pg cm^{-2} s^{-1}) fluxes in Figure 8 (RT2), to relatively high (6.0 pg cm^{-2} s^{-1}) fluxes in Figure 9 (RT3) (Table 3). In all investigated ROIs of P. *vittata*, zones of high DGT-labile Mn were mapped along the axes of individual roots, co-localized with zones of increased DGT-labile As^{III}, As^{V} and P. The spatial distribution of DGT-labile Mn showed considerable variability among individual roots, with the highest relative increase in the rhizosphere compared to the adjacent bulk soil observed in Figure 7 (RT1), exceeding the Mn

calibration working range ~15-fold. The lateral expansion of these zones of increased Mn was clearly wider than the root itself and (except for some root parts in Figure 9 (RT3)) also wider if compared to co-localized zones of increased As^{III}, As^{V} and P. In Figure 10 (RT4), the zone of increased DGT-measured Mn flux was found to be highest at the zone of root maturation and decreased towards the visible part of the root apex. Hotspots of DGT-labile Mn were found around the apical root segments in Figure 9 (RT3) and partly expanded to other zones of high Mn along the root axes. In Figure 9 (RT3), Mn hotspots occurred co-localized with P hotspots, contrarily to Figure 7 (RT1), Figure 8 (RT2), and Figure 10 (RT4), where no co-localization of Mn and P hotspots was mapped.

Exemplarily displayed in Figure 9 (RT3), DGT-measured imaging data for Fe showed no relative change in rhizosphere compared to bulk soil over all replicates.

The locally absent DGT-labile vanadium (V) signals in Figure 9 (RT3) and Figure 10 (RT4), depicted by numerous small black areas in the V DGT images, visualized apparent gel-soil contact discontinuities caused by entrapped air bubbles.

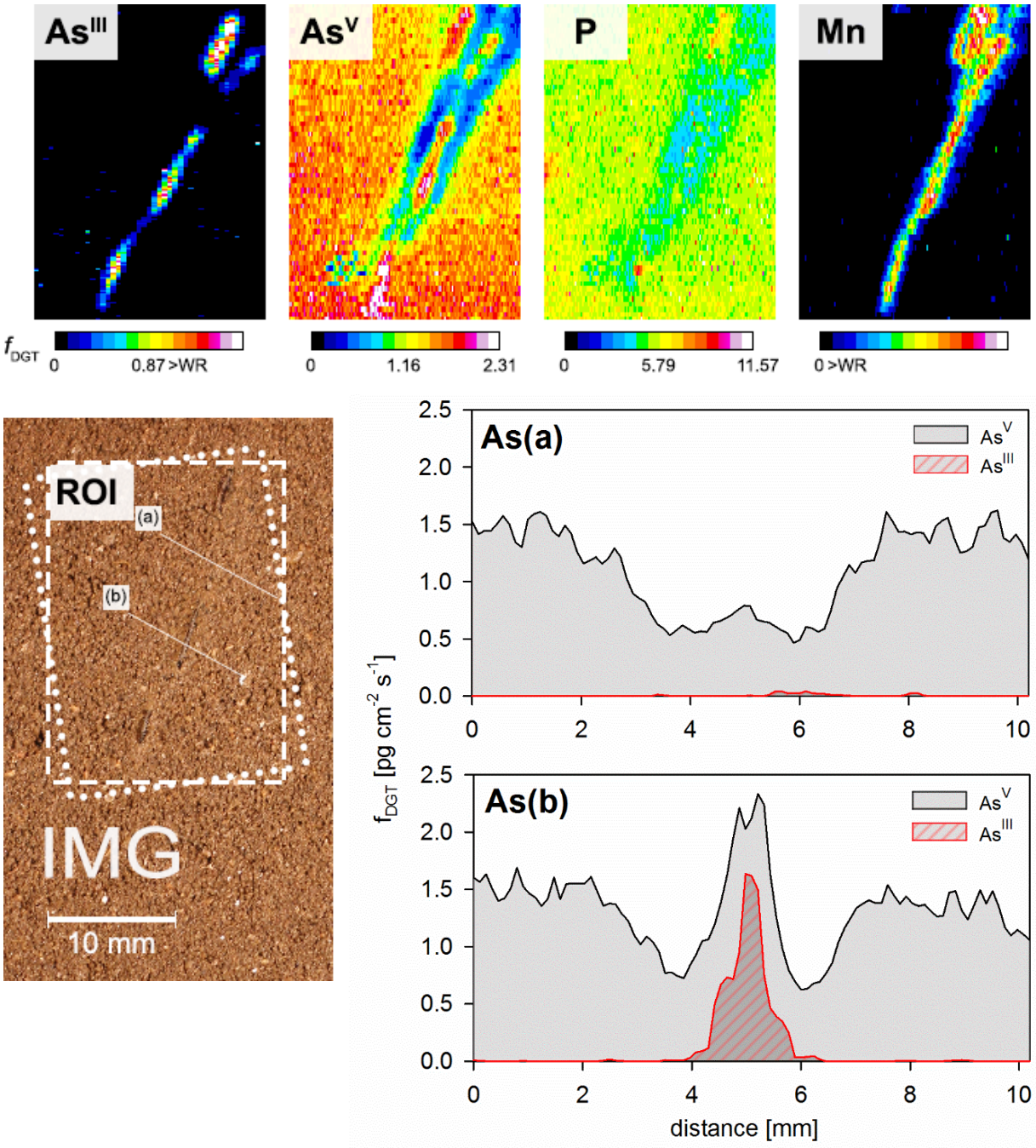

Figure 7: DGT mapped elemental flux in the rhizosphere of *P. vittata* at high spatial resolution in rhizotron 1 (RT1). DGT sampling was conducted for 24 h, 58 days after planting (DAP) at a soil water content of 74% MWHC. On the bottom left a photograph (IMG) of the region of interest (ROI) is shown. In the IMG, the dotted frame refers to the location of the As^{III}-selective MSG, whereas the dashed frame refers to the location of the MBG. Chemical images of As^{III}, As^{V}, P, and Mn are calibrated and values in the calibration bars below each image refer to DGT-measured solute flux: f_{DGT} (pg cm^{-2} s^{-1}). Black spots on the lower left of the As^{V} image indicate areas where diffusion into the DGT gel was hindered by the experimental setup (i.e., entrapped air bubbles). White lines (a and b) in the ROI indicate locations where horizontal profile plots – displayed in graphs on the right hand side of the IMG – were plotted for As^{III} and As^{V}. The profile plots compare As^{III} and As^{V} DGT-measured flux orthogonal to the root. Scale bar indication ">WR" denotes to "above working range".

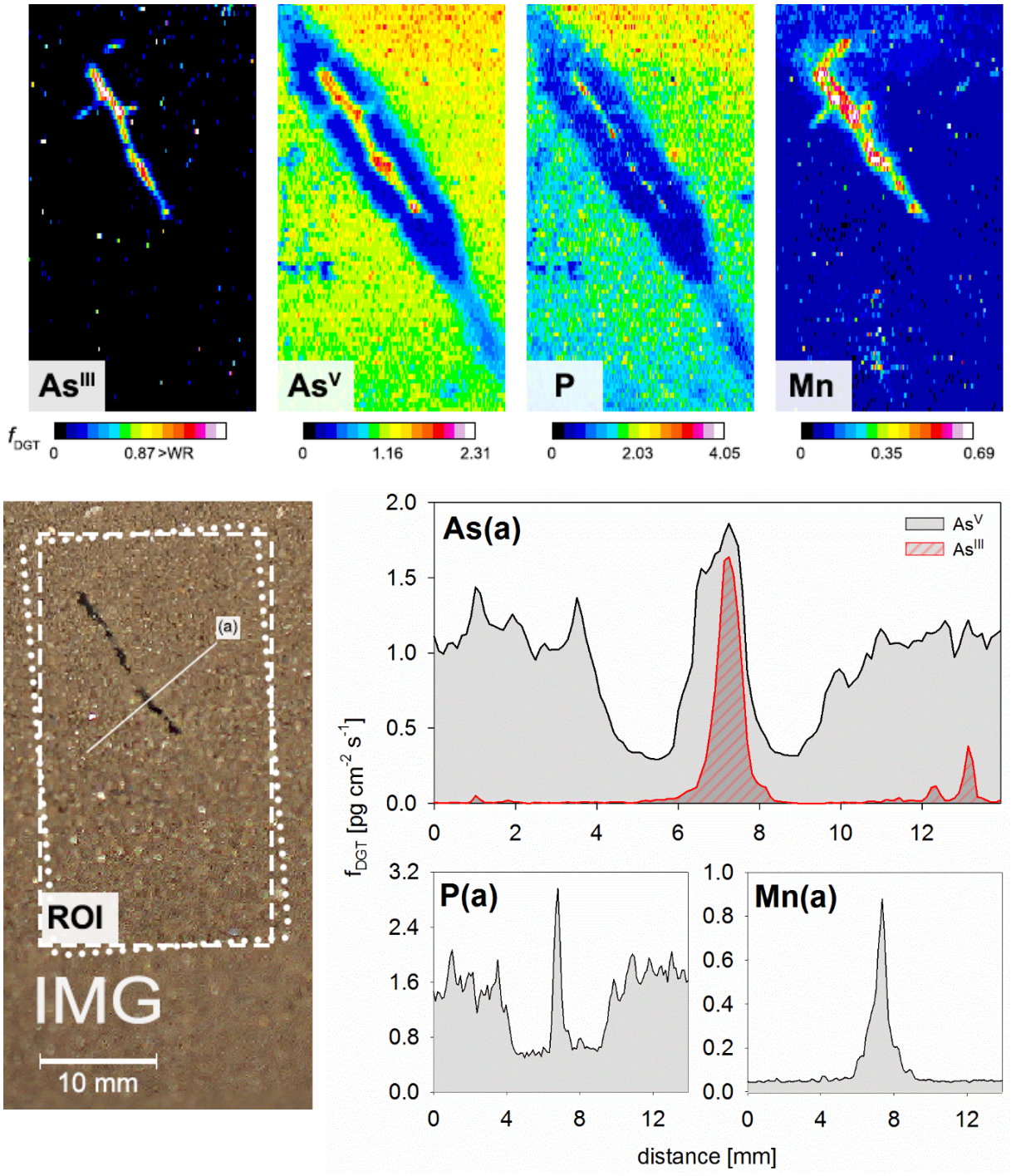

Figure 8: DGT mapped elemental flux in the rhizosphere of *P. vittata* at high spatial resolution in rhizotron 2 (RT2). DGT sampling was conducted for 24 h, 64 DAP at a soil water content of 63% MWHC. On the bottom left the IMG of the ROI is shown. In the IMG, the dotted frame refers to the location of the As^{III}-selective MSG, whereas the dashed frame refers to the location of the MBG. As^{III}, As^{V}, P, and Mn calibration bars are shown as DGT-measured solute flux f_{DGT} (pg cm^{-2} s^{-1}). The line (a) in the ROI indicates the area where horizontal profile plots – displayed in graphs on the right hand side of the IMG – were plotted for As^{III}, As^{V}, P and Mn. The As plot compares As^{III} and As^{V} DGT-measured flux orthogonal to the root. Scale bar indication ">WR" denotes to "above working range". Note that different light settings during taking the photo caused the soil to appear in a slightly darker color compared to other IMGs.

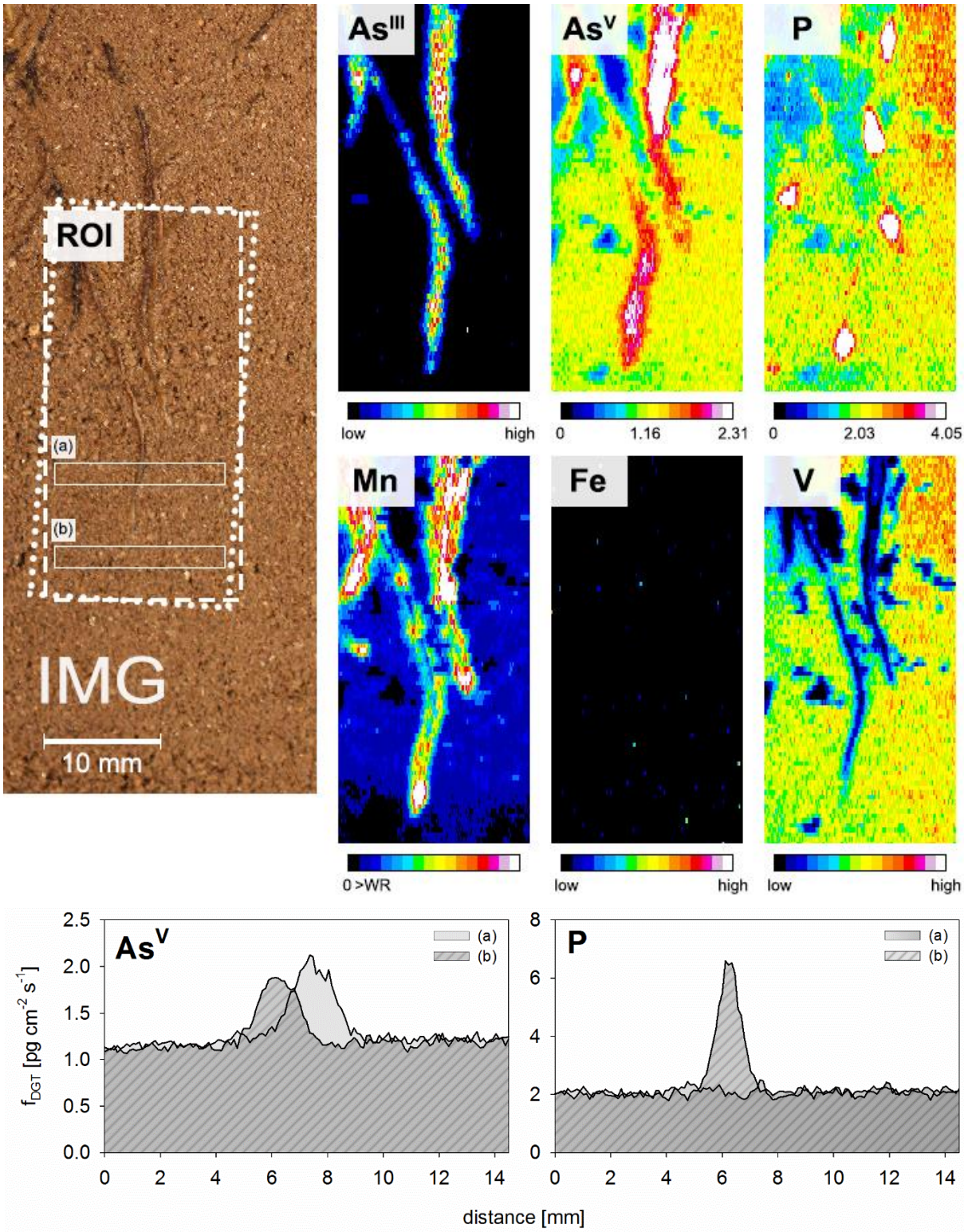

Figure 9: DGT mapped elemental flux in the rhizosphere of *P. vittata* at high spatial resolution in rhizotron 3 (RT3). DGT sampling was conducted for 24 h, 66 DAP at a soil water content of 78% MWHC. On the left the IMG of the ROI is shown. In the IMG, the dotted frame refers to the location of the As^{III}-selective MSG, whereas the dashed frame refers to the location of the MBG. As^{V}, P, and Mn calibration bars are shown as DGT-measured solute flux f_{DGT} (pg cm^{-2} s^{-1}). As^{III}, Fe and V false color scales correspond to uncalibrated, ^{13}C normalized signal intensities. Black areas in the V image indicate entrapped air bubbles. The framed (a and b) areas in the ROI indicate the areas where horizontal profile plots – displayed in graphs beneath the chemical images – were plotted for As^{V} and P. Scale bar indication ">WR" denotes to "above working range".

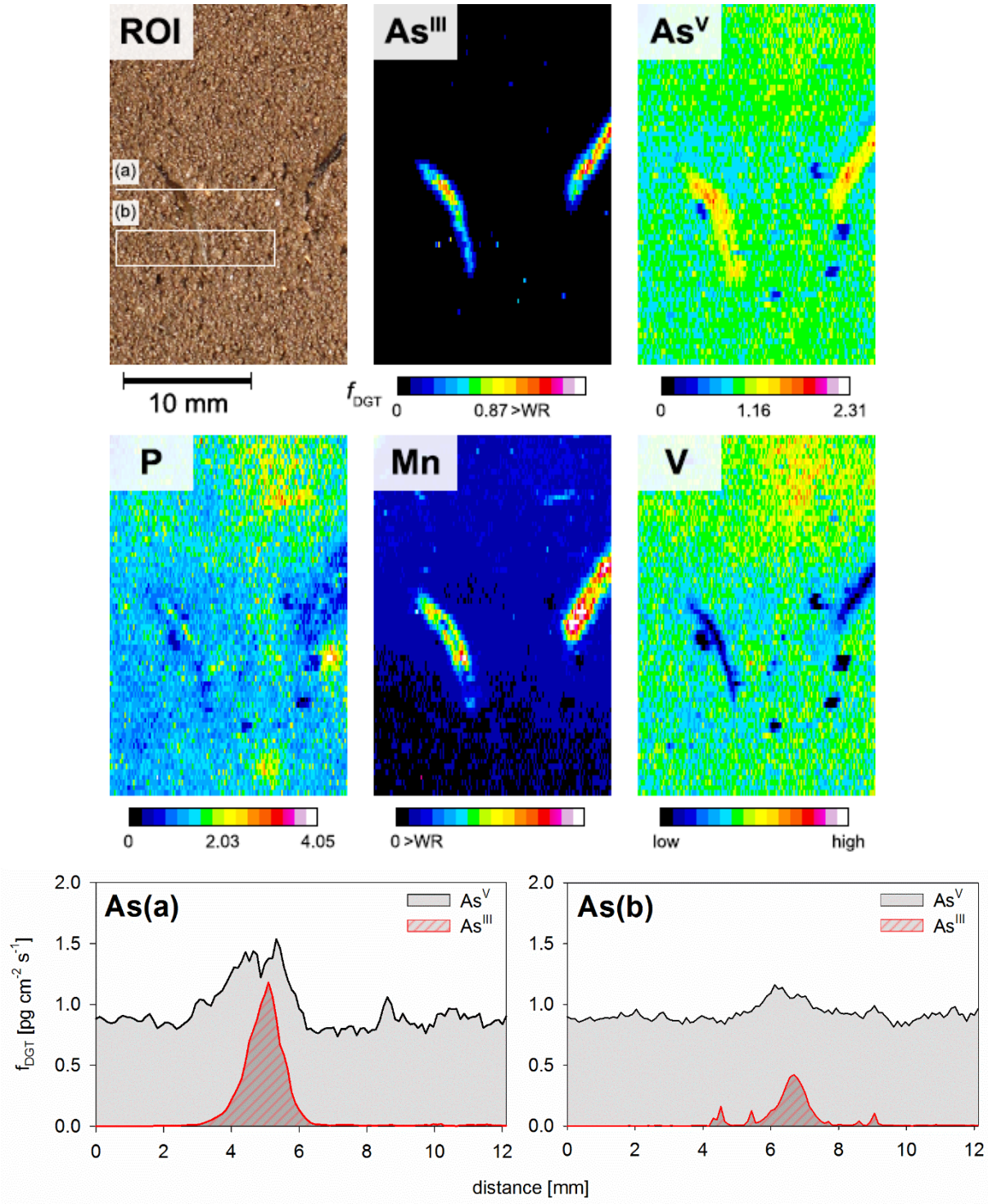

Figure 10: DGT mapped elemental flux in the rhizosphere of *P. vittata* at high spatial resolution in rhizotron 4 (RT4). DGT sampling was conducted for 24 h, 58 DAP at a soil water content of 77% MWHC. On the top left the IMG of the ROI is shown. As^{III}, As^{V}, P, and Mn calibration bars are shown as DGT-measured solute flux f_{DGT} (pg cm^{-2} s^{-1}). The V false color scale corresponds to uncalibrated, ^{13}C normalized signal intensities. Black areas in the V image indicate entrapped air bubbles. The line (a) and framed (b) areas in the ROI indicate the areas where horizontal profile plots – displayed in graphs beneath the chemical images – were plotted for As^{III} and As^{V}. The profile plots compare As^{III} and As^{V} DGT-measured flux orthogonal to the root. Scale bar indication ">WR" denotes to "above working range".

Oxygen saturation in rhizosphere and bulk soil

The O_2 PO measurements in rooted soil of *P. vittata* resulted in only one image in RT2 where distinct O_2 features were clearly visible and could be distinguished from potentially occurring experimental artifacts (Figure 11). As illustrated in Figure 11, 64 DAP, shortly after application of the PO foils, low O_2 levels were measured in densely rooted soil of *P. vittata*, indicating considerable zones of O_2 depletion. Assignment of O_2 mapping to the ROI was challenging due to the lack in spatial reference points in the densely rooted soil where multiple roots were located just behind the soil surface and might have contributed to the extensive O_2 depletion.

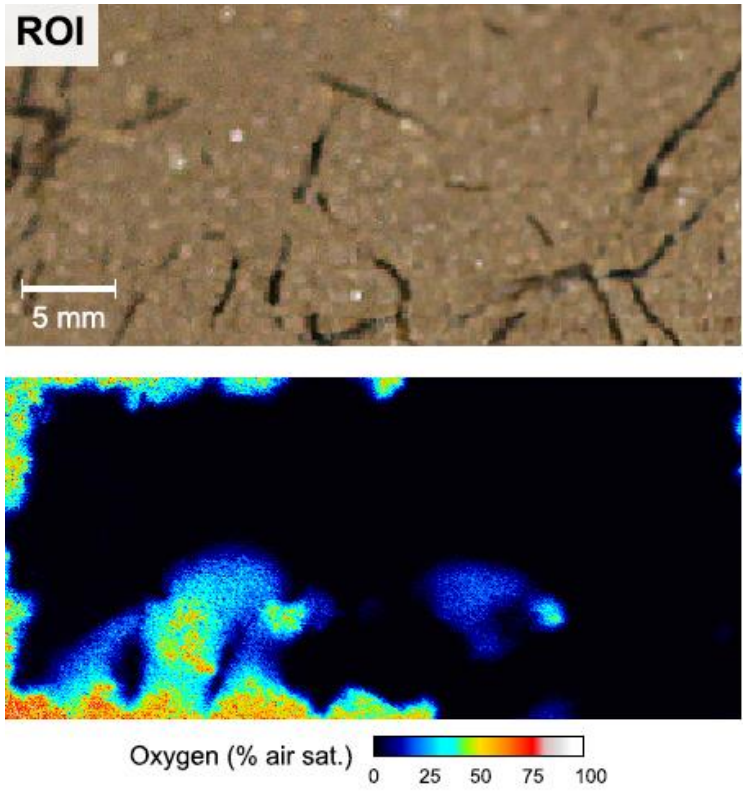

Figure 11: *In situ* measurement of oxygen distribution in the rhizosphere of *P. vittata* at high spatial resolution in rhizotron 2 (RT2). PO sampling was conducted 64 DAP at a soil water content of 63% MWHC. On the top the IMG of the region of the ROI is shown. The false color scale corresponds to the measured oxygen level in percent air saturation ($\%_{air\ sat.}$). The O_2 PO image was recorded ~20 min after the PO and dual-layer DGT deployment at the end of the photoperiod for P. *vittata*. Note that different light settings during taking the photo caused the soil to appear in a slightly darker color compared to other IMGs.

4.1.2 *Pteris quadriaurita*

Spatial distribution of DGT-labile As^{III} and As^{V} species

In agreement with the results obtained for *P. vittata*, labile As^{V} was the dominating DGT-measured As species in all three *P. quadriaurita* rhizotron replicates. The average bulk soil As^{V} DGT-flux, represented by red colored areas in the As^{V} DGT images, ranged between 1.4 pg cm^{-2} s^{-1} in Figure 13 (RT6) and 1.7 pg cm^{-2} s^{-1} in Figure 12 (RT5) (Table 3). Contrary to the As^{III} DGT data for *P. vittata*, in the rhizosphere of P. *quadriaurita*, no DGT-labile As^{III} flux was found. In Figure 12 (RT5), Figure 13 (RT6), and Figure 14 (RT7), As^{III} DGT-flux was almost absent and, besides very few, randomly distributed spots of elevated As^{III} DGT-flux (e.g. Figure 13, RT10, As(a)), in the same range throughout the ROIs (Table 3).

DGT-measured As^{III} and As^{V} showed no increased fluxes corresponding to the root positions in all rhizotron replicates of P. *quadriaurita* when compared to the respective bulk soils. However, substantially decreased As^{V} DGT-flux adjacent to individual roots was evident for all three rhizotron replicates. In Figure 12 (RT5, As(a)) and Figure 13 (RT6, As(a)), the lowest measured As^{V} DGT-flux was 0.8 and 0.5 pg cm^{-2} s^{-1}, respectively, indicating zones of As^{V} depletion extending into ~1.5–2.0 mm from the soil-root interface into the rhizosphere of *P. quadriaurita.* Average As^{V} DGT-flux within these zones was measured at 1.0 ± 0.2 pg cm^{-2} s^{-1} (n = 24) in Figure 12 (RT5, As(a)) and 0.7 ± 0.2 pg cm^{-2} s^{-1} (n = 142) in Figure 13 (RT6, As(a)), corresponding to a 40% and 49% decrease from bulk soil towards P. *quadriaurita* roots. While DGT-labile As^{V} depletion diminished towards the apical root parts, this effect was more pronounced at mature root parts and at root branches, as shown in Figure 12 (RT5) and Figure 13 (RT6), respectively. In Figure 14 (RT7), decrease of DGT-labile As^{V} was much less evident and only present directly at the root position.

<u>DGT-measured fluxes of other solutes (P, Mn, Fe)</u>

DGT-measured fluxes of labile P showed highly localized P hotspots at the root tips and decreased P along the root axis of individual roots of *P. quadriaurita*. The average background P DGT-flux varied considerably among the rhizotron replicates, with the highest bulk soil P flux measured at 3.5 pg cm^{-2} s^{-1} (Table 3) in Figure 13 (RT6). Zones of slightly increased DGT-measured P were visible in Figure 13 (RT6) and Figure 14 (RT7), both towards the root tip P hotspots. The average DGT-measured P flux at the hotspot visible around the root tip in Figure 12 (RT5, P(a)) accounts for a 1.4-fold increase of the DGT-labile P fraction compared to the bulk soil (Table 3). While similar increasing patterns in DGT-measured P flux were observed for both P hotspots in Figure 13 (RT6) and Figure 14 (RT7), in the latter the increase was more

pronounced at the root tip. Zones of P depletion were located at older parts of individual roots and showed a similar spatial distribution as congruent zones of As^V depletion. As shown in Figure 13 (RT6, P(a)), the average DGT-measured P flux in the zone of depletion at the top of the ROI amounts to a 16% decrease relative to the bulk soil. Similar, although more pronounced P depletion was mapped adjacent to the individual root in Figure 12 (RT5).

Bulk soil DGT-measured Mn fluxes showed high variability among all rhizotron replicates, with values ranging between 0.04 pg cm^{-2} s^{-1} in Figure 12 (RT5) and 4.8 pg cm^{-2} s^{-1} in Figure 14 (RT7) (Table 3). While no areas of Mn depletion around the roots were found, merging zones of increased Mn and Mn hotspots were evident for all rhizotron replicates and strongly co-localized with elevated DGT-fluxes of labile P. Hotspots of DGT-labile Mn were exclusively observed at apical root segments and merged with more expanding zones of increased Mn along the root axes. On average, the Mn hotspot in Figure 12 (RT5) showed an increased Mn flux of approximately 8.1-fold compared to bulk soil. Substantially higher relative increases, clearly exceeding the working range of the Mn calibration, of 14.1-fold and 20.8-fold were found at the Mn hotspots in Figure 14 (RT7) and Figure 13 (RT6), respectively. Extending from the apical root segments, zones of increased Mn generally decreased from the root tips towards mature root parts, however, the highest relative increase was observed at the root branches in Figure 13 (RT6).

Corresponding to the DGT chemical images of *P. vittata*, and displayed in Figure 13 (RT6) and Figure 14 (RT7), virtually no DGT-labile Fe was measured in all ROIs of the *P. quadriaurita* replicates, and similar to the dataset of P. *vittata* no root-associated changes in Fe fluxes were observed.

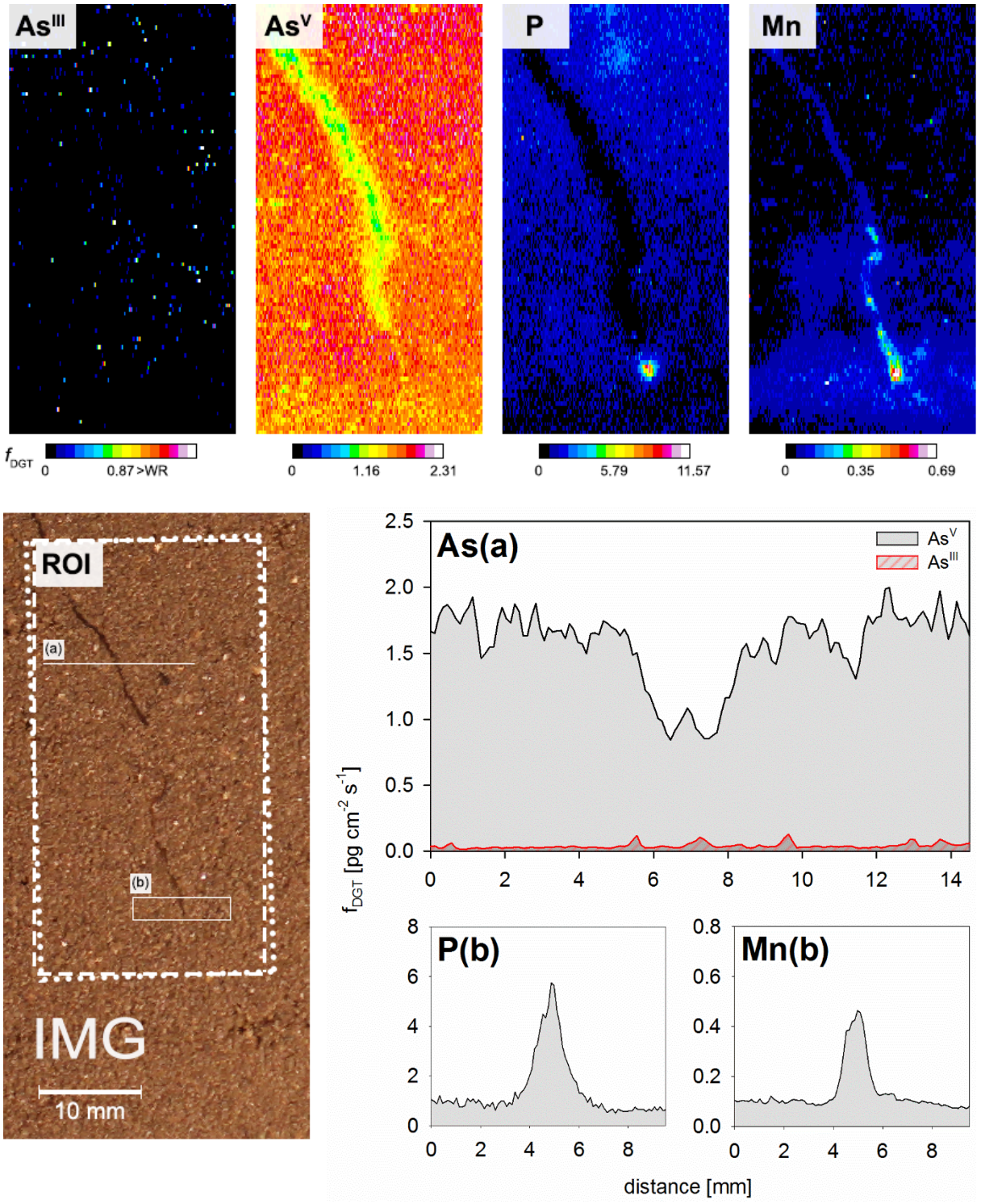

Figure 12: DGT mapped elemental flux in the rhizosphere of *P. quadriaurita* at high spatial resolution in rhizotron 5 (RT5). DGT sampling was conducted for 24 h, 70 DAP at a soil water content of 80% MWHC. On the bottom left the IMG of the ROI is shown. In the IMG, the dotted frame refers to the location of the As^{III}-selective MSG, whereas the dashed frame refers to the location of the MBG. As^{III}, As^{V}, P, and Mn calibration bars are shown as DGT-measured solute flux f_{DGT} (pg cm^{-2} s^{-1}). The line (a) and framed (b) areas in the ROI indicate the areas where horizontal profile plots – displayed in graphs on the right hand side of the IMG – were plotted for As^{III}, As^{V}, P, and Mn. The As plot compares As^{III} and As^{V} DGT-measured flux orthogonal to the root. Scale bar indication ">WR" denotes to "above working range".

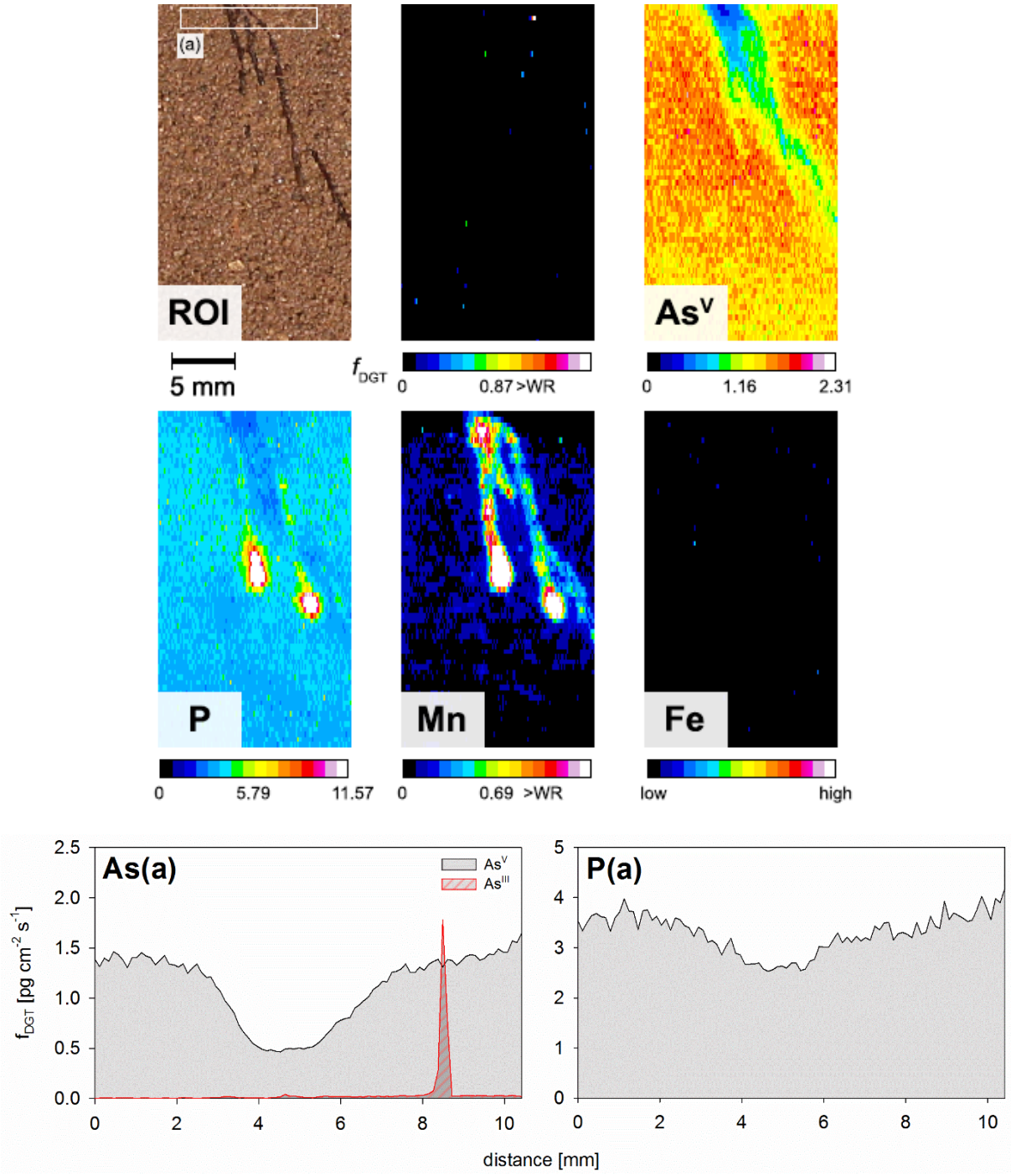

Figure 13: DGT mapped elemental flux in the rhizosphere of *P. quadriaurita* at high spatial resolution in rhizotron 6 (RT6). DGT sampling was conducted for 24 h, 72 DAP at a soil water content of 90% MWHC. On the top left the IMG of the ROI is shown. As^{III}, As^{V}, P, and Mn calibration bars are shown as DGT-measured solute flux f_{DGT} (pg cm^{-2} s^{-1}). The Fe false color scale corresponds to uncalibrated, ^{13}C normalized signal intensities. The framed (a) area in the ROI indicates the area where horizontal profile plots – displayed in graphs beneath the chemical images – were plotted for As^{III}, As^{V}, and P. The As plot compares As^{III} and As^{V} DGT-measured flux orthogonal to the roots. Scale bar indication ">WR" denotes to "above working range".

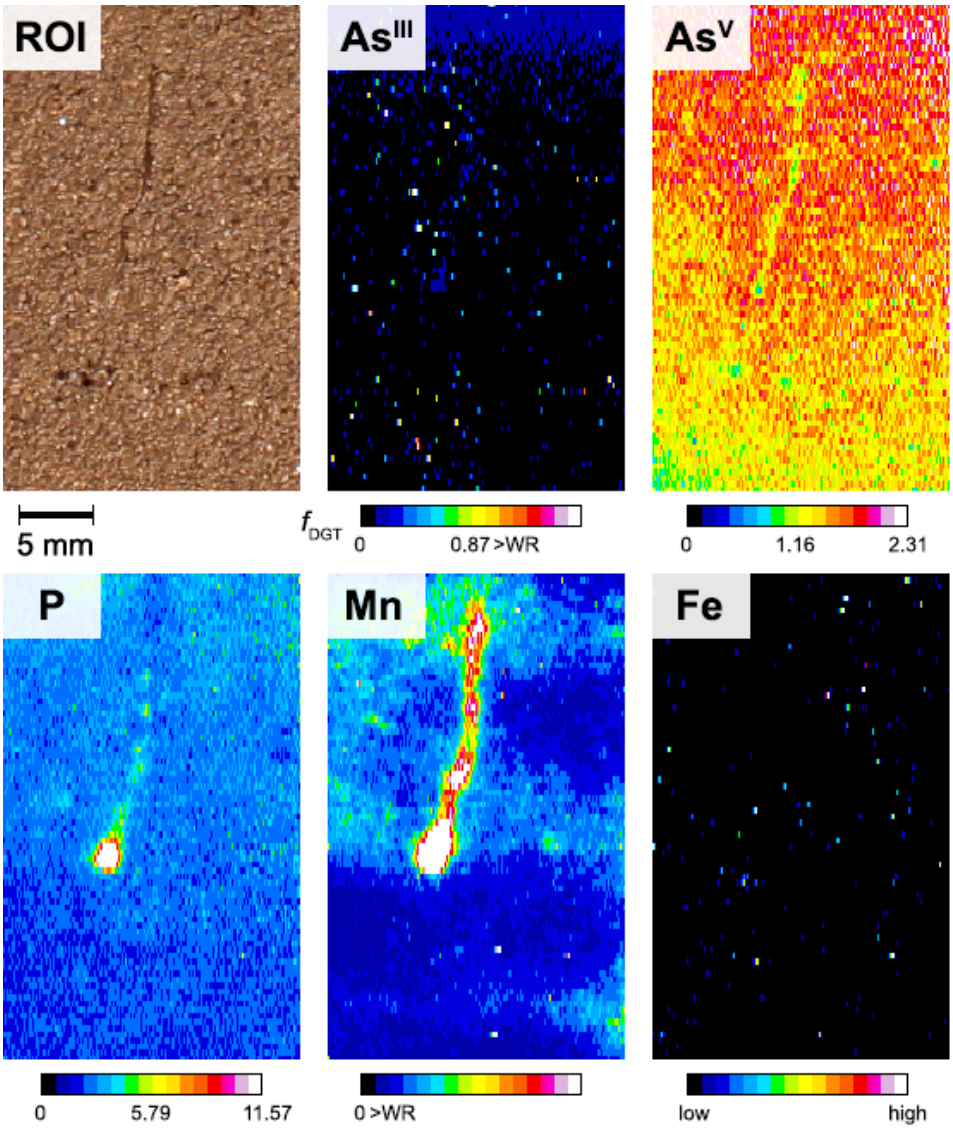

Figure 14: DGT mapped elemental flux in the rhizosphere of *P. quadriaurita* at high spatial resolution in rhizotron 7 (RT7). DGT sampling was conducted for 24 h, 70 DAP at a soil water content of 81% MWHC. On the top left the IMG of the ROI is shown. As^{III}, As^{V}, P, and Mn calibration bars are shown as DGT-measured solute flux f_{DGT} (pg cm^{-2} s^{-1}). The Fe false color scale corresponds to uncalibrated, ^{13}C normalized signal intensities. Scale bar indication ">WR" denotes to "above working range".

Oxygen saturation in rhizosphere and bulk soil

The time-resolved O_2 images of two rhizotron replicates revealed substantial changes of O_2 levels in soil areas surrounding the roots of *P. quadriaurita* (Figures 15 and 16). Drastically decreased O_2 concentrations extending from individual roots indicate extensive zones of O_2 depletion in the rhizosphere.

In Figure 15 (RT5), relatively low O_2 levels were mapped at the end of the photoperiod (18:28), ranging from 46.1 ± 4.5%$_{air\ sat.}$ in the bulk soil down to 15.8 ± 12.9%$_{air\ sat.}$ in the rooted soil where two fern roots were growing side by side on the left hand side of the ROI. Here, the average decrease in PO-measured O_2 levels between bulk and rhizosphere soil around the older root parts accounted for ~66%. Similar O_2 depletion continued at younger root parts growing towards the bottom right of the ROI, however, the extent of O_2 depletion was less pronounced and more confined to the root position. Progressive O_2 depletion extending from the last visible root part in the ROI of RT5 might indicate roots growing directly behind the soil surface. At the beginning of the next photoperiod (10:07), a second O_2 measurement showed considerable spatial expansion of the zone of lower O_2 levels, rendering these soil areas partly anaerobic.

We observed similar spatio-temporal O_2 distribution around three *P. quadriaurita* roots in Figure 16 (RT7). Here, the PO O_2 images were recorded overnight in an hourly sequence to investigate fluctuations of the O_2 levels over one photoperiod. Starting at the end of the photoperiod (18:47), we observed decreasing O_2 levels resulting in low $O_{2\ air\ sat.}$ around the roots and maximum spatial expansion of the partly anaerobic zones in the absence of photosynthesis (02:54). The decrease in PO-measured O_2 levels between 18:47 and 09:00 was similar compared to the O_2 decrease between 18:28 and 10:07 in Figure 15 (RT5). At the beginning of the photoperiod (09:00), O_2 levels gradually increased again until the last image of the PO-imaging sequence taken the next day during photosynthesis (15:19).

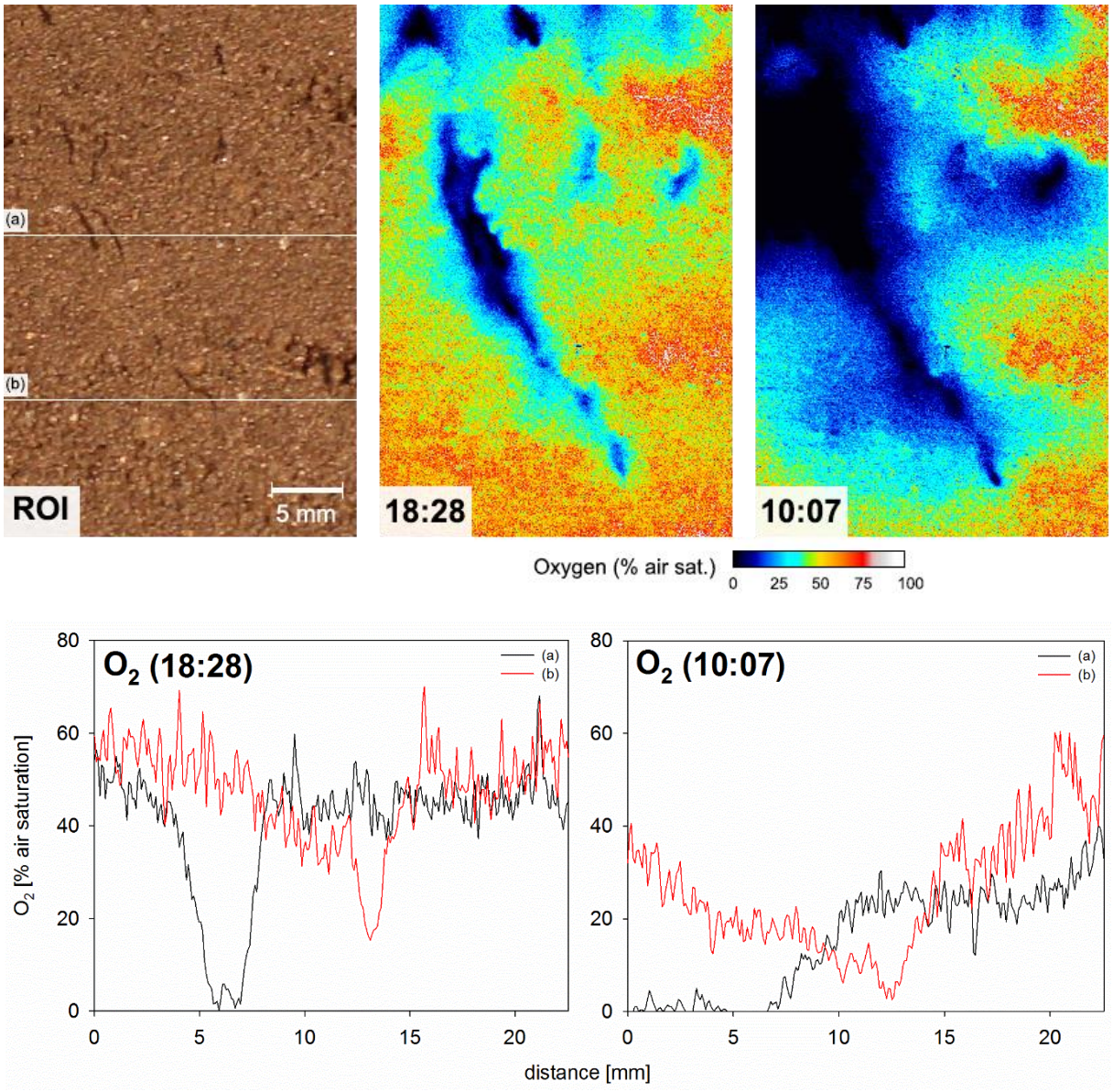

Figure 15: Spatio-temporal oxygen distribution in the rhizosphere of *P. quadriaurita* at high spatial resolution in rhizotron 5 (RT5). PO sampling was conducted 70 DAP at a soil water content of 80% MWHC. On the left the IMG of the ROI is shown. The false color scale corresponds to the measured oxygen level in percent air saturation ($\%_{air\ sat.}$). Lines (a) and (b) in the ROI indicate areas where horizontal profile plots – displayed in graphs beneath the O_2 images – were extracted from the O_2 images. The profile plots show percent air saturation (y-axis) over horizontal distance (x-axis). The time in the O_2 images denotes the actual PO-measurement time. 18:28 corresponds to the end of the photoperiod and 10:07 to the beginning of the photoperiod. The first O_2 image (18:28) was recorded ~60 min after PO and dual-layer DGT deployment.

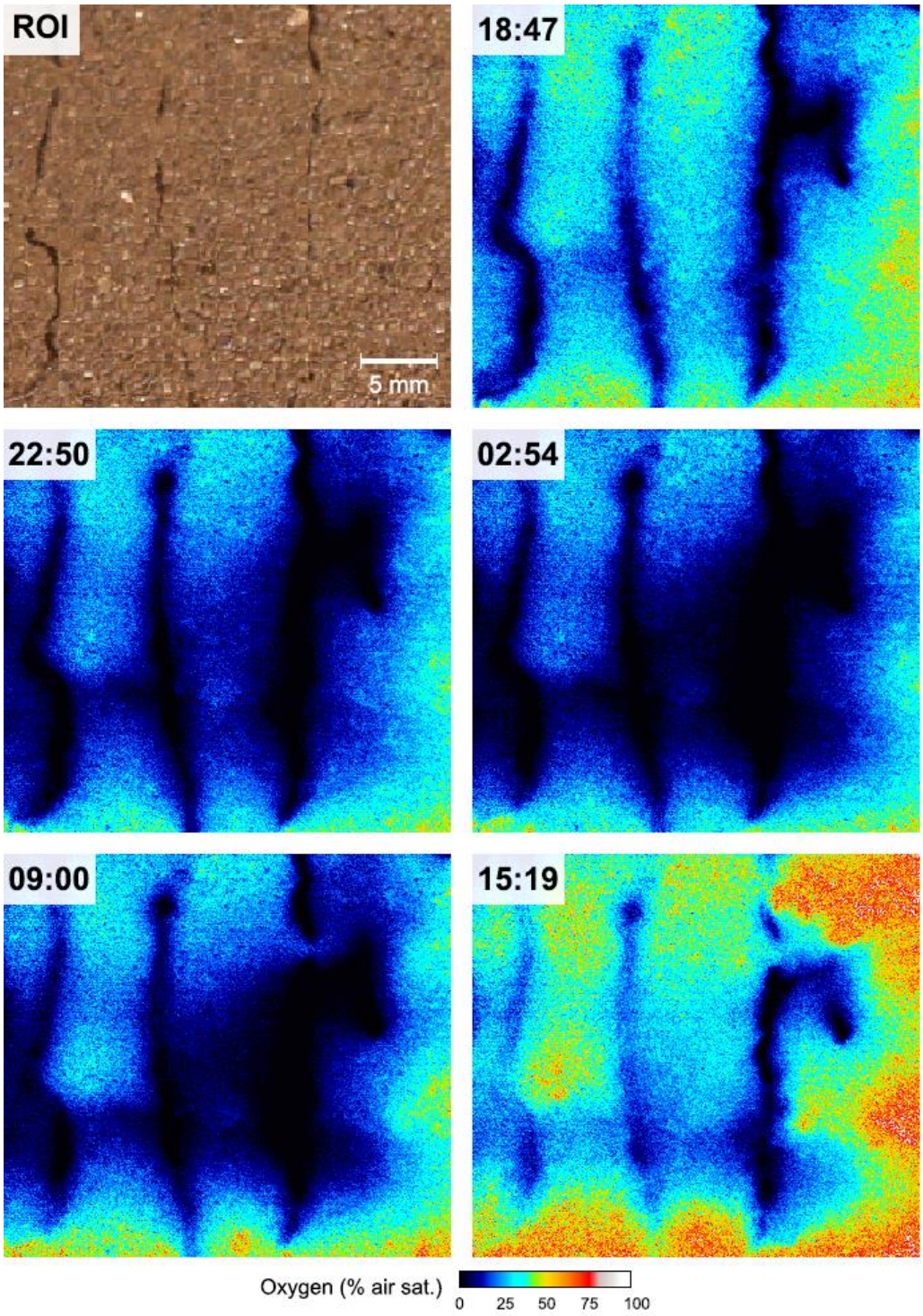

Figure 16: Spatio-temporal oxygen distribution in the rhizosphere of *P. quadriaurita* at high spatial resolution in rhizotron 7 (RT7). PO sampling was conducted 70 DAP at a soil water content of 81% MWHC. On the top left the IMG of the ROI is shown. The false color scale corresponds to the measured oxygen level in percent air saturation ($\%_{air\ sat.}$). The time in the O_2 images denotes the actual PO-measurement time. 18:47 corresponds to the end of the photoperiod and 09:00 to the beginning of the photoperiod. The first O_2 image (18:47) was recorded ~3 h after PO and dual-layer DGT deployment. In between the O_2 images at 09:00 and 15:19, RT7 was located in the greenhouse.

4.2 Arsenic accumulation in *P. vittata* and *P. quadriaurita*

After ~61 and ~69 days, respectively, of growth on highly As-contaminated Forst99 soil, *P. vittata* and *P. quadriaurita* did not show any signs of phytotoxicity symptoms besides little necrosis at the tips and edges of a few mature fronds. Average biomass production was similar for both fern species, with 3.3 **±** 0.7 g dwt of fronds and 2.0 **±** 0.7 g dwt of roots for *P. vittata* (n = 5), and 3.1 ± 0.8 g dwt of fronds and 2.0 ± 0.5 g dwt of roots for *P. quadriaurita* (n = 4). Selected elemental concentrations in fronds and roots are summarized in Figure 17. While root As concentrations were similar among the two fern species, *P. vittata* accumulated 3.3-fold more As in its fronds (6986 ± 610 mg kg^{-1} dwt) compared to *P. quadriaurita* (1611 ± 187 mg kg^{-1} dwt) (Figure 11). This was reflected by the higher As translocation factor (TF; i.e., ratio of As in fronds to As in roots) of 15 for *P. vittata* compared to the As TF of 4 for *P. quadriaurita*.

Phosphorus was approximately equally sequestered in the plant tissues, while both Mn, and particularly Fe were predominantly accumulated in the fern roots. Arsenic accumulation in roots of both fern species occurred under the influence of arbuscular mycorrhizal (AM) infections, with 35 ± 4% (n = 4) and 20 ± 6% (n = 3) of root length colonized in *P. vittata* and *P. quadriaurita*, respectively. Figure 18 shows selected microscopic images of stained AM structures penetrating cortical root cells of both fern species.

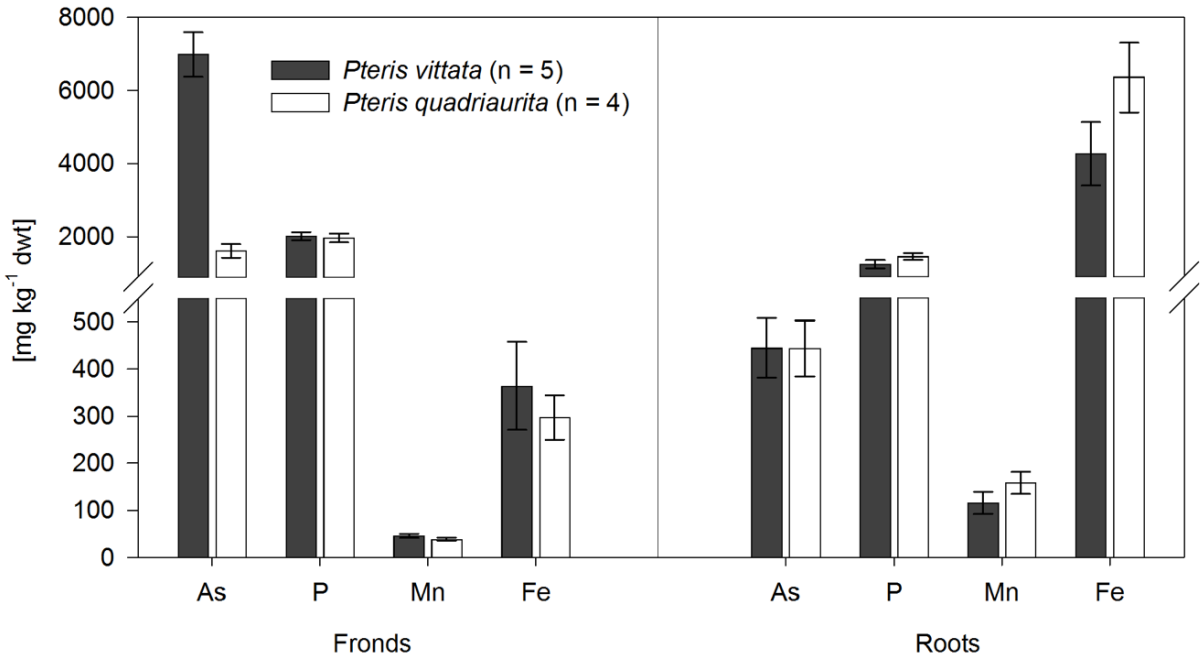

Figure 17: Elemental concentrations (mean ± SEM) in plant tissues of *P. vittata* (between 51 and 66 DAP) and *P. quadriaurita* (between 65 and 72 DAP) grown on Forst99 soil in rhizotrons.

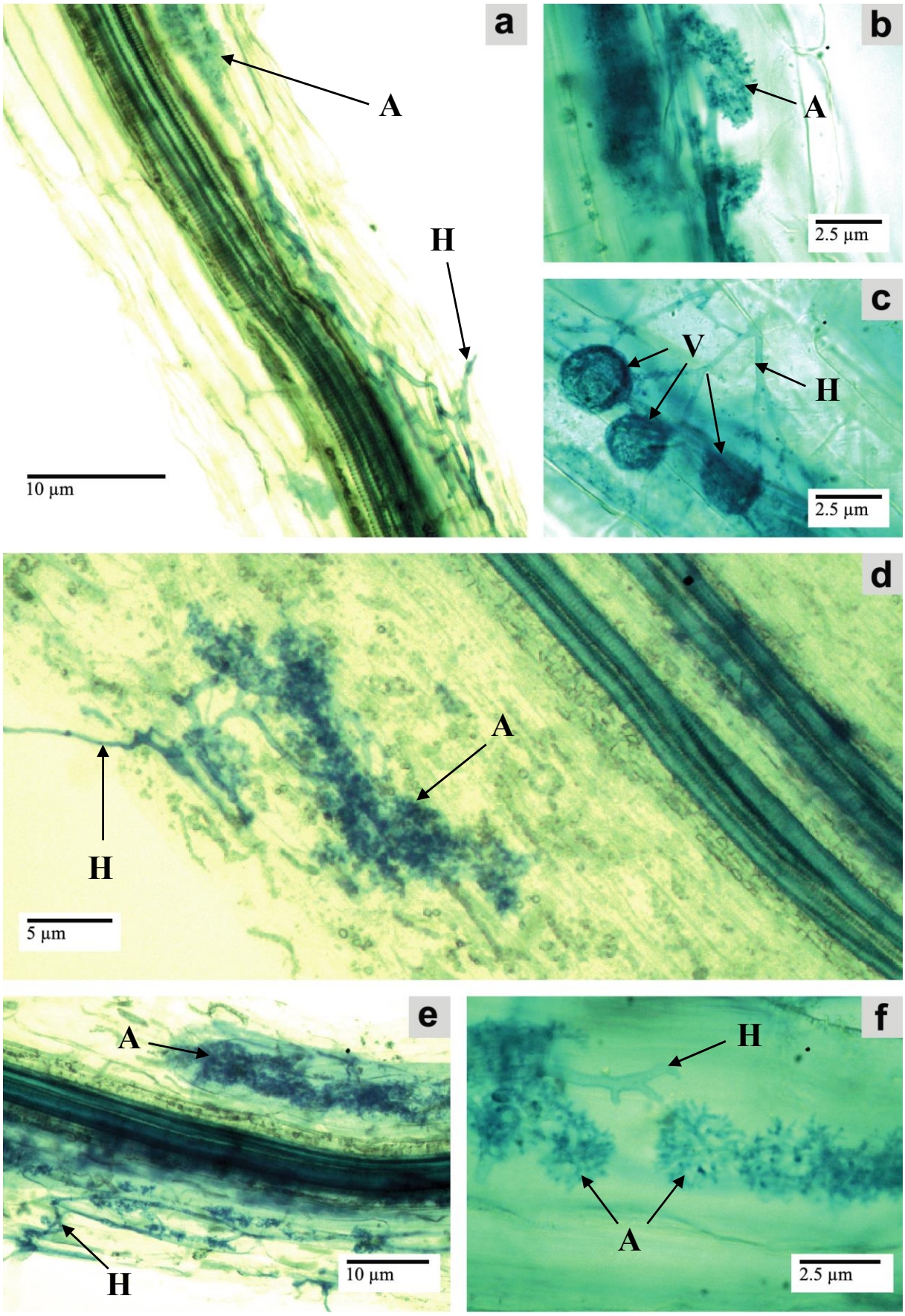

Figure 18: Arbuscular mycorrhizal infections in *P. vittata* (a, b, c) and *P. quadriaurita* (d, e, f) root tissues magnified at different spatial scales. "A" refers to arbuscule, "H" refers to hyphae, and "V" refers to vesicles.

5 DISCUSSION

5.1 Spatial pattern of inorganic As speciation and element uptake in hyperaccumulator ferns

The excessive As root uptake and efficient translocation within fern tissues confirmed the expected ability of both *P. vittata* and *P. quadriaurita* to hyperaccumulate As from As-contaminated soil. Besides similar biomass production, *P. vittata* showed clearly higher As translocation rates than *P. quadriaurita,* indicating different plant physiological adaptations.

The high pH (H_2O; 7.97) and total (*aqua regia* extractable*)* As contamination of the Forst99 soil (2080 mg kg^{-1}) was reflected in elevated As^{V} lability throughout all investigated bulk soil areas. Given that no DGT-available As^{III} was detected in the bulk soil environment, the DGT imaging data provides sound evidence that As^{V} oxyanions are the dominant, potentially bioavailable inorganic As species in aerobic, calcareous soil environments. Previous solution culture studies demonstrated that high exposure to labile As^{V} can result in elevated As^{III} concentrations in *P. vittata* growth media (Huang et al., 2011; Chen et al., 2016; Han et al., 2016). This finding is corroborated by the present DGT imaging data, with 4 out of 4 *P. vittata* DGT images showing spatially expanding zones of localized, increased As^{III} concentrations along the root axis of individual roots. Accumulation zones of total inorganic As were imaged previously in the rhizosphere of *Zea mays* L. (Kuppardt et al., 2010), *Lupinus albus* L. (Fresno et al., 2017), and *Oryza sativa* L. (Williams et al., 2014), yet, the methods used could not differentiate between labile As^{III} and As^{V} species. The fact that a previous rhizobox study could not detect relevant As^{III} accumulation in rhizosphere soil of *P. vittata* (Fitz et al., 2003) may be explained by insufficient spatial resolution of the measurement method to detect sub-mm speciation changes in the immediate vicinity of growing roots, or rapid oxidation of As^{III} to As^{V} during sample handling.

The observed As^{III} flux maxima were spatially confined to the surface and immediate surroundings of single *P. vittata* roots, forming a steep chemical gradient between rhizosphere and adjacent bulk soil. The measured As^{III}/As^{V} flux ratio decreased from up to 0.88 at the very root surface down to 0.01 in bulk soil, strongly indicating root-mediated As^{V} reduction in the rhizosphere (Figure 19). This observation supports previous work showing that, following As^{V}

uptake, As^{V} can be efficiently reduced to As^{III} within *P. vittata* root cells when grown at increased As substrate concentrations (Danh et al., 2014).

Adaptive up-regulation of the arsenate reductase (AR) activity due to high As exposure (Cesaro et al., 2015) may lead to high As^{III} accumulation rates in the root cells, exceeding the capacity of *P. vittata* for As^{III} sequestration in the vacuole and As^{III} translocation from the roots to the fronds within the DGT sampling time of 24 h (Wang et al., 2010). Thus, As^{III} efflux by *P. vittata* roots back into the apoplast and eventually the surrounding rhizosphere soil could explain the observed As^{III} accumulation in the rhizosphere. Similar to recent reports about exocellular As^{III} in *P. vittata* fronds (Datta et al., 2017), a proportion of the As^{III} pool in *P. vittata* roots may be retained in the apoplast to prevent autotoxic effects when exposed to high As^{V} concentrations. The release of secondary As^{III} across the cell membrane may be controlled by passive transport via aquaporins (e.g. PvTIP4;1) (He et al., 2016), as a result of the steep As^{III} concentration gradient between cytoplasm and external medium, and/or by active transport via enhanced expression of, so far unidentified, As^{III}-specific efflux transporters (Wang et al., 2011) (Figure 19).

Interestingly, highest As^{III} concentrations were found in the zone of root maturation, decreasing towards the root apical segments. Modelling studies showed that water and, hence, ion uptake is usually low at the very root apex, but increases towards the zone of elongation, reaching a maximum in the root hair zone (Doussan et al., 2009). Water diffusion across root cell membranes is facilitated by aquaporin channels which are also thought to be responsible for bi-directional As^{III} transport in plant roots (Bienert et al., 2008; Ali et al., 2009), including *P. vittata* (Mathews et al., 2011; He et al., 2016) (Figure 19). The abundance of aquaporins has been reported to be greatest in zones of root elongation and maturation (Hachez et al., 2006), which may explain the higher As^{III} accumulation at mature root parts compared to root apices. But how and if As^{III} efflux by *P. vittata* roots occurs via aquaporin transport is still unclear and merits further studies.

Increased DGT-measured As^{III} flux indicating As^{III} root efflux was observed for *P. vittata*, but not for *P. quadriaurita.* While As^{III} efflux by roots of non-accumulator plants has been suggested as an important As detoxification mechanism (Zhao et al., 2009), the substantially higher As translocation efficiency found in *P. vittata* (TF = 15) compared to *P. quadriaurita* (TF = 4) indicates that the root-promoted As transformation in the rhizosphere of *P. vittata* may

essentially contribute to enhanced As translocation efficiency. Since total As concentrations in roots were similar among the fern species, it may be hypothesized that *P. vittata* roots exhibit a higher AR activity than *P. quadriaurita* roots, leading to higher As^{III} concentrations in root cells and an overall more efficient As^{III} root efflux, xylem loading and translocation into fronds.

Zones of secondary As^{III} accumulation alongside roots of *P. vittata* were consistently (4 out of 4 *P. vittata* DGT images) co-localized with zones of increased As^{V} concentrations. Similar to As^{III}, root efflux of As^{V} by *P. vittata* is a potential reason for this observation. Little As^{V} efflux has been reported for *P. vittata* upon exposure to non-sterile hydroponic growth media containing 1.5 mg As^{V} L^{-1} (Huang et al., 2011). However, later solution studies under sterile conditions could not confirm this observation (Chen et al., 2016; Han et al., 2016), suggesting that microbial As^{III} oxidation caused the presence of As^{V} in the medium (Mathews et al., 2010) (see section 5.2). In addition, so far no evidence for an As^{V} efflux mechanism was reported for plants, strongly indicating that the increased As^{V} lability is not derived from As^{V} efflux by *P. vittata* roots.

An alternative explanation for the increased As^{V} concentrations along *P. vittata* roots is As^{V} mobilization from sorbent phases adhering to the root surface due to the exudation of low-molecular-weight-organic-anions (LMWOAs). Batch experiments have shown that typical LMWOAs released by plant roots like citrate, malate and oxalate can effectively mobilize As^{V} from the soil matrix (Liu et al., 2001; Zhang et al., 2005; Tao et al., 2006). Moreover, Lessl and Ma (2013) demonstrated that, under field conditions, *P. vittata* can effectively acquire As and P from sparingly-soluble phosphate rock via secretion of oxalate and malate. Some solution culture studies also detected phytate in root exudates of *P. vittata* (Tu et al., 2004; Liu et al., 2016; Fu et al., 2017), which appears to be more effective than oxalate at solubilizing As and P from phosphate rock (Fu et al., 2017). Since As^{V} and P oxyanions show physico-chemical similarity, LMWOAs released by *P. vittata* roots may induce co-dissolution of As^{V} and P through ligand exchange reactions and subsequently increased competition between As^{V} and P for sorption sites (Figure 19). This is supported by the observed co-localization of spatially expanding increased As^{V} and P concentrations in one of the *P. vittata* DGT imaging datasets. However, the fact that zones of increased As^{V} occurred not necessarily together with zones of increased P weakens this interpretation. In particular, patterns of As^{V} solubilisation around

the root apical segments were found in 3 out of 4 *P. vittata* DGT images, but only in one *P. vittata* DGT image As^V solubilisation at root apices was coincidental with that of P. Therefore, we hypothesize that As^V is solubilized without direct link to P mobilization or that in highly As-contaminated soil the higher molar ratio of As/P may strongly influence DGT mapped fluxes. Additionally, labile P can be readily taken up by roots and/or rhizosphere microorganisms, leading to the observed less pronounced increase compared to As^V.

In addition to root exudates, As-resistant bacteria may cause As^V mobilization along *P. vittata* roots (Ghosh et al., 2011; Han et al., 2017b). Under conditions of limited Fe availability, which may occur in aerobic soils with above neutral pH such as the Forst99 soil used in this study, rhizobacteria of *P. vittata* have been shown to enhance their Fe nutrition by producing Fe(III) chelating organic ligands such as siderophores (George et al., 2012; Liu et al., 2015). Given the efficiency of bacterial siderophores in Fe solubilisation from Fe(III) (oxyhydr)oxide surfaces (Kraemer, 2004), siderophore-promoted Fe solubilisation can result in co-dissolution of As^V and Fe(III) (oxyhydr)oxides and subsequently increased As^V concentrations in the rhizosphere (Liu et al., 2017) (Figure 19). However, in 4 out of 4 *P. vittata* DGT images no relevant changes in the labile Fe flux were observed, even at root locations showing highly elevated As^V lability. This observation indicates that either labile Fe concentrations were sufficient for microbial nutrition, or that potentially solubilized Fe(III) was rapidly re-oxidized under these conditions (see section 5.2).

In contrast to the co-localized zones of As^{III} and As^V accumulation in the rhizosphere of *P. vittata*, zones of As^V depletion were observed in all DGT images of both hyperaccumulator species. In 2 out of 4 *P. vittata* DGT images, *P. vittata* roots were able to deplete approximately 55% of the labile As^V fraction within the first 3 mm of rhizosphere soil adjacent to the zones of As^{III} and As^V co-accumulation along the root axis. This As^V depletion in the rhizosphere is in good agreement with Fitz et al. (2003), where the lateral expansion of the lowered DGT-labile As^V concentrations correlated well with the average length of *P. vittata* root hairs. Similar As^V depletion, although less pronounced, was observed alongside roots of *P. quadriaurita*. The decreased As^V concentrations in the rhizosphere porewater may be ascribed to the low solubility of As^V compounds in aerobic soil environments (Wenzel et al., 2002), highly efficient uptake of labile As^V in hyperaccumulator roots (Poynton et al., 2004), and limited As^V replenishment by desorption and/or dissolution from the solid phase of well-aged

contaminated soils (Fitz et al., 2003). As previously suggested by Fitz and Wenzel (2006), diffusion appears to be rate-limiting in As uptake by hyperaccumulator ferns, further contributing to the observed patterns of strong As^V depletion in the rhizosphere (Jungk, 2002; Hinsinger et al., 2005). The finding of axial depletion gradients, with clearly lower As^V fluxes around mature root segments compared to apical root segments, indicates that quantifiable As^V depletion may establish only when roots had enough time to absorb relevant amounts of As^V solutes. The fact that *P. vittata* depleted the rhizosphere soil solution down to lower minimum As^V concentrations compared to *P. quadriaurita*, further suggests a higher As^V uptake efficiency of *P. vittata*. Therefore, it may be supposed that P/As^V transporters in *P. vittata* root tissues are more abundant and/or have a higher affinity for As^V compared to *P. quadriaurita*, leading to a higher As^V/P ratio in *P. vittata* root cells.

Co-localized zones of As^V and P depletion along single roots of both hyperaccumulator ferns were found in all but 1 out of 7 DGT images. Depletion zones of labile P were mapped in previous DGT–LA-ICP-MS studies in the rhizosphere of *Brassica napus* L. (Santner et al., 2012), *Zea mays* L. (Kreuzeder et al., 2013), *Triticum aestivum* L., *Fagopyrum esculentum* Moench, and *Lupinus albus* L. (Kreuzeder et al., unpublished). Similar to the depletion of labile As^V, high P uptake rates of the fern roots and limited resupply from the solid phase may cause the development of the observed P depletion zones (Kreuzeder et al., unpublished). The congruent spatial expansion of As^V and P depletion indicates that As^V and P oxyanions were at least partly acquired from similar sources (e.g. As^V- and P-bearing Fe(III) (oxyhydr)oxides) and through similar acquisition mechanisms (e.g. release of LMWOAs). The mapped P depletion of both hyperaccumulator ferns was further influenced by the action of AM fungi, which are known to confer protective effects on the host plant by improving P nutrition without increasing As uptake (Liu et al., 2005; Smith et al., 2010). The extra-radical hyphae observed in roots of *P. vittata* and *P. quadriaurita* enables the ferns to acquire labile P from a greater soil volume (Smith and Read, 2008), and may thereby directly contribute to the spatial expansion of decreased P lability in the DGT images. Root exudates solubilizing P can also diffuse over some distance from roots into the soil, which can lead to a complex P concentration profile with maximum P concentrations beyond the zone of P depletion (Hinsinger, 2001). Such peaks of increased P were also observed in this study, where they occurred as punctiform hotspots in isolated micro-niches similar to the P hotspots in the DGT images provided by Santner et al. (2012). Distinct patterns of localized, highly increased P

concentrations at the root apices were observed in 1 out of 4 *P. vittata* and in all *P. quadriaurita* DGT images. They are in line with the observations of Santner et al. (2012) and Kreuzeder et al. (unpublished), who found similar patterns of P solubilization in the rhizosphere of different crop plants and concluded that both, P mobilization and/or P release by roots may explain the localized increased P lability frequently observed around root apices.

As previously demonstrated by Kreuzeder et al. (unpublished), localized P accumulation at the root apical segments was coincidental with that of Mn. Considering the enhanced release of LMWOAs at root apices (Neumann and Römheld, 2007) and their similar effect on Mn and P solubilisation (Ström, 1997; Lambers et al., 2015), it is possible that P and Mn mobilization in the rhizosphere of hyperaccumulator ferns are coupled. Moreover, given that zones of spatially expanding increased Mn concentrations were mapped more often and independently from P solubilisation, we assume that the cause of the elevated element concentrations had a stronger effect on Mn, owing to the higher chemical reactivity and lability of Mn in soils compared to P (see section 5.2). However, P and Mn mobilization might also proceed only partly through the same mechanisms. Some variations in P and Mn background bulk soil fluxes between individual DGT images of this study may further be linked to variations in elemental diffusivity in the corresponding soil areas as a result of variations in the soil water content (Hooda et al., 1999).

Although Mn and Fe concentrations in plant tissues were clearly above deficiency levels (Broadley et al., 2012), no Mn or Fe depletion associated to the root location was observed in any of the DGT images that might indicate root uptake exceeding resupply of these essential micronutrients. Since Fe(III) (oxyhydr)oxides are the main binding sites for As in the Forst99 soil (Lombi et al., 2000), we further expected that depletion of labile As^{V} along hyperaccumulator roots occurs concurrently to solubilisation of Fe(III) sorbent phases. However, independent of the fern species, the DGT-measured labile Fe flux remained consistently (7 out of 7 DGT images) unchanged in the presence of roots. This is in seeming contrast to the findings of Fitz et al. (2003), who reported that soluble Fe in rhizosphere soil solution of *P. vittata* collected with soil porewater samplers increased 2.8-fold compared to the bulk soil solution. The authors concluded that increased DOC concentrations in the rhizosphere triggered the dissolution of Fe from Fe(III) (oxyhydr)oxide surfaces by the formation of soluble Fe-DOC complexes. These Fe-DOC complexes can also contribute to the

DGT-measured Fe flux (Puy et al., 2016), but we suppose that the extent of manifestation in the DGT chemical images is negligible due to their potentially low diffusion coefficients and low dissociation rate constants and the ultra-thin diffusive layer used in this study (Scally et al., 2003; Warnken et al., 2007). The high Fe concentrations measured in root tissues of both ferns might indicate internal accumulation of Fe(III) through adsorption to carboxylic groups in the apoplast (White, 2012). However, as the roots were only cleared with tap water, the possibility that the high Fe concentrations are derived from residual Fe particles adhering to the roots cannot be ruled out.

5.2 Spatial pattern of soil redox reactions in the rhizosphere

The observation of strong O_2 depletion concurrently to spatially expanding increased Mn lability alongside roots of both *P. vittata* and *P. quadriaurita* point at the establishment of spatio-temporal redox gradients in the rhizosphere. The soil redox potential (E_h) is primarily controlled by microorganisms, which derive energy from coupling the oxidation of organic matter or reduced inorganic compounds to the reduction of terminal electron acceptors (TEAs). Molecular oxygen (O_2) serves as the primary TEA as long as there is sufficient supply. Under conditions of limited O_2 supply, which were apparent in all PO-images of this study, microorganisms switch from aerobic to facultative or obligate anaerobic respiration and use alternative TEAs following the reduction potentials of the respective redox couples: O_2/H_2O > NO_3^-/NO_2^- > Mn(III)/Mn(II) > Mn(IV)/Mn(II) > Fe(III)/Fe(II) > SO_4^{2-}/HS^- (McBride, 1994). Hence, the reduced O_2 levels and increased concentrations of labile Mn likely indicate their function as microbial TEAs, resulting in lowered E_h values in the rhizosphere compared to bulk soil (Figure 19). Lowered E_h conditions can directly contribute to the observed As^V reduction in the rhizosphere of *P. vittata*. However, as elevated As^{III} concentrations were highly confined to the surface and immediate surroundings of single *P. vittata* roots, the measured O_2 depletion appears to be insufficient to cause reducing E_h conditions which could result in direct As^V reduction.

Manganese (III, IV) (oxyhydr)oxides are highly redox-active mineral phases which readily participate as strong oxidizing agents in numerous biogeochemical redox and sorption reactions affecting the mobility and distribution of many metal(loid) contaminants in soil (Tebo et al., 2005; Borch et al., 2010). The formation of Mn(III, IV) (oxyhydr)oxides proceeds mostly through the activity of Mn(II)-oxidizing microorganisms (bacteria and fungi) (Figure 19),

which have been reported to thrive in aerobic-anaerobic transition zones (Tebo et al., 2004; Thompson et al., 2005). Solubilisation of Mn is influenced by (bio)chemical Mn reduction, with Mn(III, IV) (oxyhydr)oxides prevailing in aerobic soil environments and at high pH, and labile Mn (i.e., Mn(II)) dominating in anaerobic conditions and at low pH (Adriano, 2001). Since acidification of the rhizosphere is unlikely to play an important role in As hyperaccumulation (Wenzel et al., 2004), particularly in soils with high carbonate buffer capacity (Fitz et al., 2003), the results of the DGT–LA-ICP-MS investigation indicate that reductive dissolution of Mn(III, IV) (oxyhydr)oxides was responsible for the observed increase in Mn lability alongside fern roots (Figure 19).

The reduction of Mn(III, IV) occurs prior to that of Fe(III) as it is initiated at relatively high E_h values (≤~400 mV at pH 7) (Borch et al., 2010). Contrary, chemical oxidation of Mn(II) is thermodynamically less favorable and, hence, slower than that of Fe(II). Thus, the absence of relative changes in soluble Fe concentrations in all DGT images of *P. vittata* and *P. quadriaurita* may be explained by both, E_h values in rhizosphere soil limiting Fe(III) reduction, and rapid abiotic and biotic re-oxidation of potentially solubilized Fe(II) to Fe(III). The temporarily dissolving Fe(III) (oxyhydr)oxides may liberate sorbed As^V and thereby contribute to the enhanced As^V lability in the rhizosphere of *P. vittata* (Figure 19). Once released into solution, As^V can be quickly re-adsorbed onto surfaces of Fe(III) (oxyhydr)oxides (Ying et al., 2012), which may be indicated by the diminishing As^V accumulation when *P. vittata* roots were covered by a thin soil layer. Considering the high lability of Mn(II) in reduced soil systems (Mundus et al., 2012), the narrow accumulation of labile Mn in the immediate vicinity of hyperaccumulator roots suggests relatively sharp redox gradients at the soil-root interface.

Several Mn(III, IV) (oxyhydr)oxides, such as e.g. birnessite (δ-MnO_2), are effective As^{III} oxidants in soil systems (Oscarson et al., 1981; Manning et al., 2002; Suda and Makino, 2016). Whereas the oxidation of As^{III} by O_2 or Fe(III) is very slow (Kim and Nriagu, 2000; Oscarson et al., 1981), the oxidation of As^{III} by δ-MnO_2 is rapid, proceeding within minutes (Scott and Morgan, 1995). Simplified, the chemical oxidation reaction of As^{III} to As^V on δ-MnO_2 surfaces follows two sequential steps, including (1) Mn(IV) reduction to Mn(III) and formation of an Mn(III)OOH intermediate reaction product, and (2) As(III) oxidation by Mn(III)OOH producing Mn(II) and As^V (Nesbitt et al., 1998). The Mn(II) and As^V reaction products are released into solution, where they may readily bind to available sorption sites (Ying et al., 2012), including the

introduced DGT gel surface. The fact that zones of increased labile Mn in the rhizosphere of *P. vittata* occurred consistently (4 out of 4 *P. vittata* DGT images) together with zones of labile As^{III} and As^{V} co-accumulation indicates that this chemical As^{III} oxidation also occurred alongside roots of *P. vittata* (Figure 19). Thus, consistent with recent findings derived from soil incubation experiments (Ehlert et al., 2016; Xu et al., 2017), Mn(III, IV) (oxyhydr)oxides may effectively retard reductive As mobilization and leaching from the rhizosphere into the surrounding bulk soil environment via direct oxidation of As^{III} and/or promoting Fe(II) oxidation to Fe(III) leading to As^{III}/As^{V} adsorption on freshly formed Fe(III) (oxyhydr)oxide surfaces (Figure 19). However, similar patterns of increased Mn lability in the rhizosphere of *P. quadriaurita* suggest that As^{III} oxidation on Mn(III, IV) (oxyhydr)oxide surfaces is less important for the observed Mn solubilisation than reductive dissolution of Mn(III, IV) (oxyhydr)oxides.

Although our PO-imaging data is not providing any information about the origin of the change in O_2 levels (Blossfeld, 2013), it is reasonable to assume that root and microbial respiration are the main causes for the observed O_2 depletion in the rhizosphere of the As-hyperaccumulating ferns. It is well-known that carbon-rich compounds exuded from living roots (rhizodeposition) stimulate a higher population density and metabolic activity of microorganisms in the rhizosphere compared to the bulk soil (Jones et al., 2004; Watt et al., 2006) (Figure 19). Generally, microbial density is considered to be highest in the zone of root elongation and root hair formation, decreasing bi-directionally towards the root apices and the zone of root maturation (Wenzel et al., 2004). Thus, the enhanced O_2 depletion extending behind the root apical segments in the PO images of *P. quadriaurita* may be linked to the spatial distribution of microbial O_2 consumption alongside individual roots. However, rhizodeposition and subsequent proliferation of the microbial community is not only affected by the root development status. Also changes in the photosynthetic activity of plants influence their interactions with the rhizosphere microbiome (Neumann and Römheld, 2007). The temporal fluctuations in O_2 levels observed in the rhizosphere of *P. quadriaurita* indicate that the pattern of O_2 consumption followed a diurnal rhythm (Lambers et al., 2002). The observed peak O_2 depletion reached in the absence of photosynthesis may be caused by elevated carbohydrate supply during the end of the photoperiod and subsequently elevated bacterial and fungal activity and respiration. More detailed information on the microbial community is essentially needed for the interpretation of these observations.

The colonization of root tissues by microorganisms may further extend to the apoplasm of the cortex (Marschner, 2012), as shown in this study by the AM fungi penetrating root cortical cells of both hyperaccumulator ferns. Using synchrotron radiation spectroscopy, González-Chávez et al. (2014) demonstrated that rapid As^{V} reduction and subsequent extrusion of As^{III} occurs in extra-radical hyphae of *Rhizophagus intraradices*, indicating that AM symbionts not only contribute to limit As transfer to host roots, but also to As transformation in the rhizosphere.

In addition to AM fungi, many other endophytes can directly oxidize As^{III} and reduce As^{V} in the apoplast (Xu et al., 2016), influencing the subsequent As transport *in planta* (Figure 19). Several microbes are known to cope with high As^{V}-loadings in the medium by Intracellular reduction of As^{V} via AR and subsequent As^{III} extrusion via As^{III}-specific efflux pumps (Oremland and Stolz, 2003). Strict or facultative anaerobic bacteria expressing the As^{V} respiratory reductase (ArrA) can also use As^{V} as TEA in dissimilatory As^{V} respiration (Cavalca et al., 2013). Since both, high As^{V}-loadings and limited O_2 supply were apparent along *P. vittata* roots, the observed increased As^{III} concentrations might not only derive from As^{III} root efflux, but also from microbial As^{V} reduction (Figure 19). On the other hand, rapid microbial As^{III} oxidation via As^{III} oxidase (*aio*) also appears to play an essential role in the rhizosphere of *P. vittata.* Mathews et al. (2010) showed that, under aerated hydroponic conditions, a major portion of As^{III} in the sterile growth media of *P. vittata* can be oxidized to As^{V} within 24 h, whereas no As^{III} oxidation in the growth media was found without *P. vittata*. More recently, Wang et al. (2012) observed complete As^{III} oxidation within 48 h in hydroponic solution containing *P. vittata* rhizobacteria, which diminished after the addition of antibiotics. These observations indicate that root-associated As^{III}-oxidizing microorganisms, and especially bacteria, play a critical role in controlling As dynamics *P. vittata* rhizospheres and thus, may also have contributed to the localized increased As^{V} concentrations along *P. vittata* roots in this study (Figure 19). Besides, microorganisms can also produce reactive organic or inorganic compounds that participate in redox reactions with As^{III} or As^{V} and thereby indirectly trigger inorganic As transformation. In particular, (semi-)quinones and hydroquinones produced during microbial reduction of humic substances may have contributed to As^{III} oxidation and As^{V} reduction, respectively (Borch et al., 2010) (Figure 19).

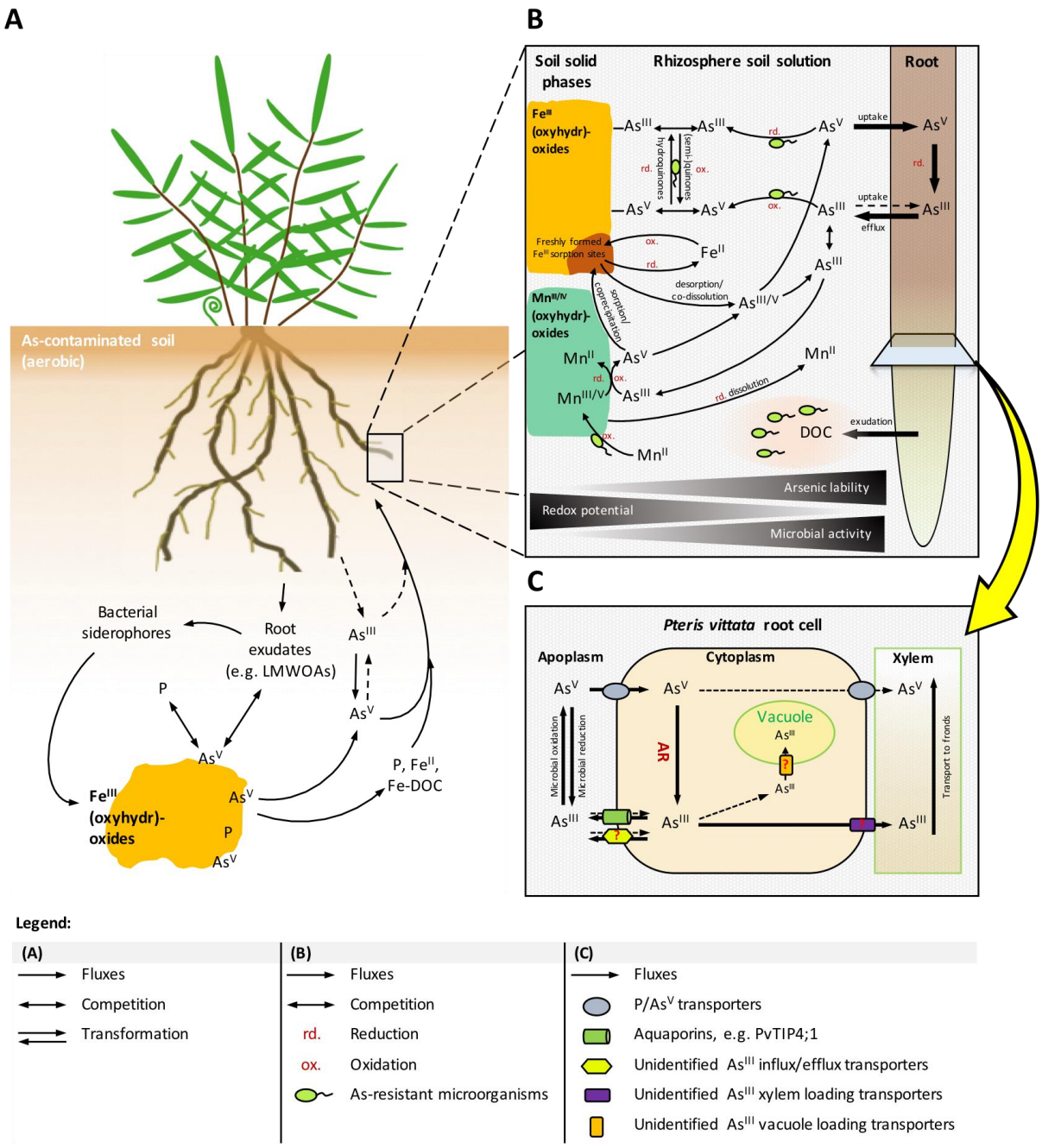

Figure 19: Conceptual model of inorganic As biogeochemistry in the rhizosphere of *P. vittata* grown in As-contaminated, aerobic soil. The line thickness relates to the dominancy of As flux pathways, with the dotted lines indicating minor pathways. (A) Co-mobilization of As^{V}, P and Fe^{II} from Fe(III) (oxyhydr)oxide sorption phases. LMWOAs, low-molecular-weight-organic-anions. (B) Selected biogeochemical gradients and abiotic/biotic redox reactions that affect the inorganic As speciation and contribute to As cycling in the rhizosphere soil solution. DOC, dissolved organic carbon. (C) Simplified As uptake and metabolism pathways in *P. vittata* root cells. Question marks indicate knowledge gaps. AR, arsenate reductase.

6 CONCLUSION

In this study we successfully applied a dual-layer DGT–LA-ICP-MS methodology in combination with PO O_2 sensing, allowing for multi-analyte mapping of labile inorganic As species, other elemental solutes, and O_2 in the rhizosphere of ferns at high spatial (sub-mm) resolution. The resulting chemical images simultaneously visualized the small-scale spatial heterogeneity of DGT-labile As^{III}, As^{V}, P, Mn and Fe species and O_2 levels between the rhizosphere and the bulk soil as well as alongside individual roots for the first time.

Consistent with their As hyperaccumulation abilities, *P. vittata* and *P. quadriaurita* showed strong As^{V} depletion way beyond the root position, demonstrating efficient As^{V} mobilization in the rhizosphere. Spatial pattern of As^{V} depletion were related to the root development status, with enhanced As^{V} depletion surrounding older root segments compared to younger root parts. Decreased As^{V} concentrations coincided with zones of decreased P, corroborating their analogous uptake pathways in hyperaccumulating ferns.

The DGT-based inorganic As speciation provided – to the best of our knowledge – the first evidence of elevated As^{III} concentrations in the rhizosphere of soil-grown *P. vittata* specimen. The localized, increased As^{III} lability alongside *P. vittata* roots pointed at As^{III} efflux from root cells into the apoplast and the surrounding rhizosphere soil. Contrary to our expectations, no indication for As^{III} efflux was found in the rhizosphere of *P. quadriaurita*. Efflux of excess As^{III} concentrations might be an adaptive mechanism of *P. vittata* to (1) limit the As^{III} burden within root cells to physiologically tolerable levels, and to (2) overcome capacity limitations for As^{III} translocation from the roots to the fronds if grown at high soil As concentrations. However, the release of As^{III} back into the environment by *P. vittata* following As^{V} uptake must be considered when *P. vittata* is used for the phytoremediation of highly As-contaminated soil. Increased As^{V} concentrations, co-localized with increased As^{III}, resulted from either As^{V} mobilization from soil solid phases and/or re-oxidation of effluxed As^{III} in the rhizosphere.

The PO-measured O_2 depletion in the rhizosphere relative to bulk soil indicated the formation of spatio-temporal redox gradients. Time-resolved O_2 imaging alongside roots of *P. quadriaurita* further showed diurnal fluctuations in O_2 levels, likely caused by changing patterns of root and microbial respiration. Due to the low O_2 availability, Mn (oxyhydr)oxides served as TEAs for microorganisms and underwent reductive dissolution. Potentially

solubilized Fe (oxyhyr)oxides were rapidly re-oxidized, which probably induced the formation of fresh As^{III}/As^{V} sorption sites. Moreover, rapid abiotic/biotic As^{III} oxidation mediated by Mn (oxyhydr)oxides (abiotic) and/or As-resistant fungal and microbial rhizosphere organisms (biotic) contributed to dynamic As cycling in the rhizosphere and root apoplast of *P. vittata* and, thus, effectively confined As mobilization to the immediate root surroundings.

In conclusion, our 2D high resolution chemical imaging data highlight the importance of small-scale redox reactions on As transformation and speciation dynamics in the rhizosphere of As-hyperaccumulating ferns grown in aerobic soil. The presented dual-layer DGT–LA-ICP-MS methodology in combination with POs is a promising tool to provide advanced perspectives on mechanisms controlling the biogeochemistry of As in the soil-plant interface, which are essential to effectively mitigate the risks posed by As-contaminated environments.

APPENDIX

BULK SOIL DGT-FLUX MEASUREMENTS.

The selected areas for calculating bulk soil (i.e., soil areas that were unaffected by root activities) DGT-fluxes in the corresponding ROIs of *P. vittata* (i.e., RT1, RT2, RT3, and RT4) and *P. quadriaurita* (i.e., RT5, RT6, and RT7) rhizotron replicates are shown in Figure A1.

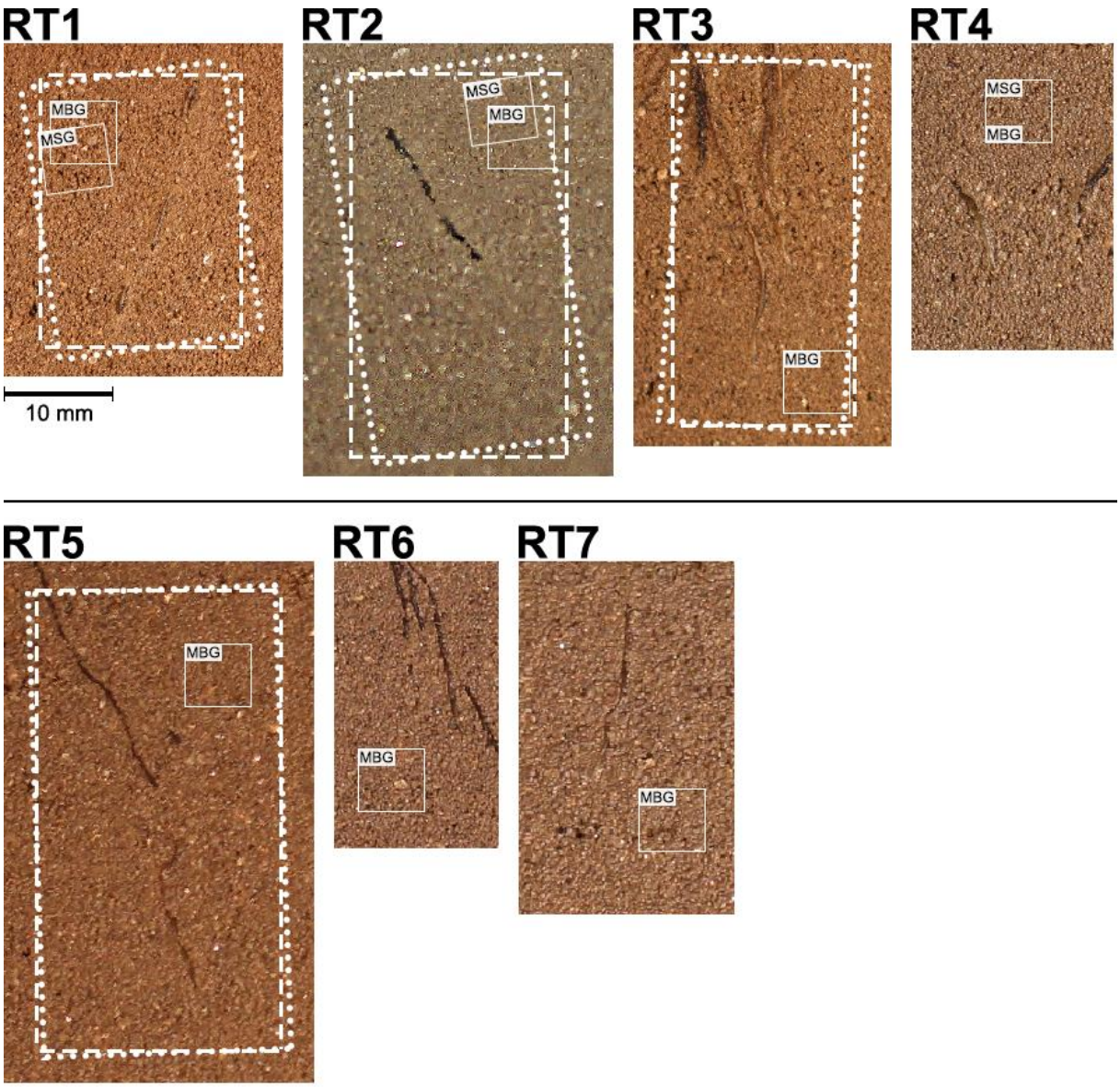

Figure A1: Photographic IMGs of the ROIs in the rhizotron replicates RT1–RT7 showing the selected areas for bulk soil DGT-flux measurements. In IMGs of RT1, RT2, RT3, and RT5, the dotted frame refers to the location of the As^{III}-selective MSG, whereas the dashed frame refers to the location of the MBG. In IMGs of RT4, RT6, and RT7, offset between MSG and MBG DGTs was negligible. Solid frames in the IMGs indicate the areas selected for calculating the mean As^{III} (MSG), As^{V}, P, and Mn (MBG) DGT-fluxes and standard deviations in bulk soil. In RT5, RT6, and RT7, As^{III} (MSG) DGT-flux was measured over the whole ROI. Note that different light settings during taking the photo of RT2 caused the soil to appear in a slightly darker color compared to other IMGs.

LIST OF FIGURES

LIST OF TABLES

REFERENCES

ADRIANO, D. C. 2001. *Trace Elements in Terrestrial Environments: Biogeochemistry, Bioavailability, and Risks of Metals,* New York, Springer.

ALI, W., ISAYENKOV, S. V., ZHAO, F.-J. & MAATHUIS, F. J. M. 2009. Arsenite transport in plants. *Cellular and Molecular Life Sciences,* 66**,** 2329-2339.

BAKER, A. J. M., MCGRATH, S. P., SIDOLI, C. M. D. & REEVES, R. D. 1994. The possibility of in situ heavy metal decontamination of polluted soils using crops of metal-accumulating plants. *Resources, Conservation and Recycling,* 11**,** 41-49.

BENNETT, W. W., TEASDALE, P. R., PANTHER, J. G., WELSH, D. T. & JOLLEY, D. F. 2011. Speciation of dissolved inorganic arsenic by diffusive gradients in thin films: selective binding of AsIII by 3-mercaptopropyl-functionalized silica gel. *Anal Chem,* 83**,** 8293-9.

BHATTACHARJEE, H. & ROSEN, B. P. 2007. Arsenic Metabolism in Prokaryotic and Eukaryotic Microbes. *In:* NIES, D. H. & SILVER, S. (eds.) *Molecular Microbiology of Heavy Metals.* Berlin, Heidelberg: Springer Berlin Heidelberg.

BIENERT, G. P., THORSEN, M., SCHÜSSLER, M. D., NILSSON, H. R., WAGNER, A., TAMÁS, M. J. & JAHN, T. P. 2008. A subgroup of plant aquaporins facilitate the bi-directional diffusion of As(OH)3 and Sb(OH)3across membranes. *BMC Biology,* 6**,** 1-15.

BLOSSFELD, S. 2013. Light for the dark side of plant life: —Planar optodes visualizing rhizosphere processes. *Plant and Soil,* 369**,** 29-32.

BLOSSFELD, S. & GANSERT, D. 2012. The Use of Planar Optodes in Root Studies for Quantitative Imaging. *In:* MANCUSO, S. (ed.) *Measuring Roots: An Updated Approach.* Berlin, Heidelberg: Springer Berlin Heidelberg.

BLUM, W. E. H., SPIEGEL, H. & WENZEL, W. W. 1996. *Bodenzustandsinventur, Konzeption und Durchführung,* Vienna, Bundesminsterium für Land und Forstwirtschaft und Bundesministerium für Wissenschaft; Verkehr und Kunst.

BORCH, T., KRETZSCHMAR, R., KAPPLER, A., CAPPELLEN, P. V., GINDER-VOGEL, M., VOEGELIN, A. & CAMPBELL, K. 2010. Biogeochemical Redox Processes and their Impact on Contaminant Dynamics. *Environmental Science & Technology,* 44**,** 15-23.

BROADLEY, M., BROWN, P., CAKMAK, I., RENGEL, Z. & ZHAO, F. 2012. Chapter 7 - Function of Nutrients: Micronutrients A2 - Marschner, Petra. *Marschner's Mineral Nutrition of Higher Plants (Third Edition).* San Diego: Academic Press.

CAVALCA, L., CORSINI, A., ZACCHEO, P., ANDREONI, V. & MUYZER, G. 2013. Microbial transformations of arsenic: perspectives for biological removal of arsenic from water. *Future Microbiology,* 8**,** 753-768.

CESARO, P., CATTANEO, C., BONA, E., BERTA, G. & CAVALETTO, M. 2015. The arsenic hyperaccumulating Pteris vittata expresses two arsenate reductases. *Scientific Reports,* 5**,** 14525.

CHEN, Y., FU, J.-W., HAN, Y.-H., RATHINASABAPATHI, B. & MA, L. Q. 2016. High As exposure induced substantial arsenite efflux in As-hyperaccumulator Pteris vittata. *Chemosphere,* 144**,** 2189-2194.

CHEN, Y., XU, W., SHEN, H., YAN, H., XU, W., HE, Z. & MA, M. 2013. Engineering Arsenic Tolerance and Hyperaccumulation in Plants for Phytoremediation by a PvACR3 Transgenic Approach. *Environmental Science & Technology,* 47**,** 9355-9362.

DANH, L. T., TRUONG, P., MAMMUCARI, R. & FOSTER, N. 2014. A Critical Review of the Arsenic Uptake Mechanisms and Phytoremediation Potential of Pteris vittata. *International Journal of Phytoremediation,* 16**,** 429-453.

DAS, S., CHOU, M.-L., JEAN, J.-S., YANG, H.-J. & KIM, P. J. 2017. Arsenic-enrichment enhanced root exudates and altered rhizosphere microbial communities and activities in hyperaccumulator Pteris vittata. *Journal of Hazardous Materials,* 325**,** 279-287.

DATTA, R., DAS, P., TAPPERO, R., PUNAMIYA, P., ELZINGA, E., SAHI, S., FENG, H., KIISKILA, J. & SARKAR, D. 2017. Evidence for exocellular Arsenic in Fronds of Pteris vittata. *Scientific Reports,* 7**,** 2839.

DAVISON, W. & ZHANG, H. 1994. In situ speciation measurements of trace components in natural waters using thin-film gels. *Nature,* 367**,** 546-548.

DAVISON, W. & ZHANG, H. 2016. Introduction to DGT. *In:* DAVISON, W. (ed.) *Diffusive Gradients in Thin-Films for Environmental Measurements.* UK: Camebridge University Press.

DEGRYSE, F., SMOLDERS, E., ZHANG, H. & DAVISON, W. 2009. Predicting availability of mineral elements to plants with the DGT technique: a review of experimental data and interpretation by modelling. *Environmental Chemistry,* 6**,** 198-218.

DING, S., XU, D., WANG, Y., WANG, Y., LI, Y., GONG, M. & ZHANG, C. 2016. Simultaneous Measurements of Eight Oxyanions Using High-Capacity Diffusive Gradients in Thin Films (Zr-Oxide DGT) with a High-Efficiency Elution Procedure. *Environmental Science & Technology,* 50**,** 7572-7580.

DOUSSAN, C., PAGÈS, L. & PIERRET, A. 2009. Soil Exploration and Resource Acquisition by Plant Roots: An Architectural and Modelling Point of View. *In:* LICHTFOUSE, E., NAVARRETE, M., DEBAEKE, P., VÉRONIQUE, S. & ALBEROLA, C. (eds.) *Sustainable Agriculture.* Dordrecht: Springer Netherlands.

DUAN, G.-L., ZHU, Y.-G., TONG, Y.-P., CAI, C. & KNEER, R. 2005. Characterization of Arsenate Reductase in the Extract of Roots and Fronds of Chinese Brake Fern, an Arsenic Hyperaccumulator. *Plant Physiology,* 138**,** 461-469.

EDMUNDS, W. M., AHMED, K. M. & WHITEHEAD, P. G. 2015. A review of arsenic and its impacts in groundwater of the Ganges-Brahmaputra-Meghna delta, Bangladesh. *Environmental Science: Processes & Impacts,* 17**,** 1032-1046.

EHLERT, K., MIKUTTA, C. & KRETZSCHMAR, R. 2016. Effects of Manganese Oxide on Arsenic Reduction and Leaching from Contaminated Floodplain Soil. *Environmental Science & Technology,* 50**,** 9251-9261.

FITZ, W. J. & WENZEL, W. W. 2002. Arsenic transformations in the soil/rhizosphere/plant system: fundamentals and potential application to phytoremediation. *Journal of Biotechnology,* 99**,** 259-278.

FITZ, W. J. & WENZEL, W. W. 2006. Sequestration of arsenic by plants. *In:* NAIDU, R., SMITH, E., OWENS, G., BHATTACHARYA, P. & NADEBAUM, P. (eds.) *Managing Arsenic In The Environment.* Australia: CSIRO.

FITZ, W. J., WENZEL, W. W., ZHANG, H., NURMI, J., ŠTIPEK, K., FISCHEROVA, Z., SCHWEIGER, P., KÖLLENSPERGER, G., MA, L. Q. & STINGEDER, G. 2003. Rhizosphere Characteristics of the Arsenic Hyperaccumulator Pteris vittata L. and Monitoring of Phytoremoval Efficiency. *Environmental Science & Technology,* 37**,** 5008-5014.

FRESNO, T., PEÑALOSA, J. M., SANTNER, J., PUSCHENREITER, M. & MORENO-JIMÉNEZ, E. 2017. Effect of Lupinus albus L. root activities on As and Cu mobility after addition of iron-based soil amendments. *Chemosphere,* 182**,** 373-381.

FU, J.-W., LIU, X., HAN, Y.-H., MEI, H., CAO, Y., DE OLIVEIRA, L. M., LIU, Y., RATHINASABAPATHI, B., CHEN, Y. & MA, L. Q. 2017. Arsenic-hyperaccumulator Pteris vittata efficiently solubilized phosphate rock to sustain plant growth and As uptake. *Journal of Hazardous Materials,* 330**,** 68-75.

GANSERT, D. & BLOSSFELD, S. 2008. The Application of Novel Optical Sensors (Optodes) in Experimental Plant Ecology. *In:* LÜTTGE, U., BEYSCHLAG, W. & MURATA, J. (eds.) *Progress in Botany.* Berlin, Heidelberg: Springer Berlin Heidelberg.

GEORGE, E., HORST, W. J. & NEUMANN, E. 2012. Chapter 17 - Adaptation of Plants to Adverse Chemical Soil Conditions A2 - Marschner, Petra. *Marschner's Mineral Nutrition of Higher Plants (Third Edition).* San Diego: Academic Press.

GHOSH, P., RATHINASABAPATHI, B. & MA, L. Q. 2011. Arsenic-resistant bacteria solubilized arsenic in the growth media and increased growth of arsenic hyperaccumulator Pteris vittata L. *Bioresource Technology,* 102**,** 8756-8761.

GLUD, R. N., RAMSING, N. B., GUNDERSEN, J. K. & KLIMANT, I. 1996. Planar optrodes: a new tool for fine scale measurements of two-dimensional O2 distribution in benthic communities. *Marine Ecology Progress Series,* 140**,** 217-226.

GONZAGA, M. I. S., MA, L. Q., SANTOS, J. A. G. & MATIAS, M. I. S. 2009. Rhizosphere characteristics of two arsenic hyperaccumulating Pteris ferns. *Science of The Total Environment,* 407**,** 4711-4716.

GONZÁLEZ-CHÁVEZ, M. D. C. A., MILLER, B., MALDONADO-MENDOZA, I. E., SCHECKEL, K. & CARRILLO-GONZÁLEZ, R. 2014. Localization and speciation of arsenic in Glomus intraradices by synchrotron radiation spectroscopic analysis. *Fungal Biology,* 118**,** 444-452.

GUAN, D.-X., WILLIAMS, P. N., LUO, J., ZHENG, J.-L., XU, H.-C., CAI, C. & MA, L. Q. 2015. Novel Precipitated Zirconia-Based DGT Technique for High-Resolution Imaging of Oxyanions in Waters and Sediments. *Environmental Science & Technology,* 49**,** 3653-3661.

HACHEZ, C., MOSHELION, M., ZELAZNY, E., CAVEZ, D. & CHAUMONT, F. 2006. Localization and Quantification of Plasma Membrane Aquaporin Expression in Maize Primary Root: A Clue to Understanding their Role as Cellular Plumbers. *Plant Molecular Biology,* 62**,** 305-323.

HAN, C., REN, J., WANG, Z., TANG, H. & XU, D. 2017a. A novel hybrid sensor for combined imaging of dissolved oxygen and labile phosphorus flux in sediment and water. *Water Research,* 108**,** 179-188.

HAN, Y.-H., LIU, X., RATHINASABAPATHI, B., LI, H.-B., CHEN, Y. & MA, L. Q. 2017b. Mechanisms of efficient As solubilization in soils and As accumulation by As-hyperaccumulator Pteris vittata. *Environmental Pollution,* 227**,** 569-577.

HAN, Y. H., FU, J. W., CHEN, Y., RATHINASABAPATHI, B. & MA, L. Q. 2016. Arsenic uptake, arsenite efflux and plant growth in hyperaccumulator Pteris vittata: Role of arsenic-resistant bacteria. *Chemosphere,* 144**,** 1937-42.

HE, Z., YAN, H., CHEN, Y., SHEN, H., XU, W., ZHANG, H., SHI, L., ZHU, Y.-G. & MA, M. 2016. An aquaporin PvTIP4;1 from Pteris vittata may mediate arsenite uptake. *New Phytologist,* 209**,** 746-761.

HINSINGER, P. 2001. Bioavailability of soil inorganic P in the rhizosphere as affected by root-induced chemical changes: a review. *Plant and Soil,* 237**,** 173-195.

HINSINGER, P., GOBRAN, G. R., GREGORY, P. J. & WENZEL, W. W. 2005. Rhizosphere geometry and heterogeneity arising from root-mediated physical and chemical processes. *New Phytologist,* 168**,** 293-303.

HOEFER, C., SANTNER, J., BORISOV, S. M., WENZEL, W. W. & PUSCHENREITER, M. 2017. Integrating chemical imaging of cationic trace metal solutes and pH into a single hydrogel layer. *Analytica Chimica Acta,* 950**,** 88-97.

HOEFER, C., SANTNER, J., PUSCHENREITER, M. & WENZEL, W. W. 2015. Localized metal solubilization in the rhizosphere of Salix smithiana upon sulfur application. *Environ Sci Technol,* 49**,** 4522-9.

HÖFER, C. 2017. *Development and application of novel chemical imaging methods in the rhizosphere using the diffusive gradients in thin films technique and planar optodes.* PhD Dissertation, University of Natural Resources and Life Sciences, Vienna.

HOODA, P. S., ZHANG, H., DAVISON, W. & EDWARDS, A. C. 1999. Measuring bioavailable trace metals by diffusive gradients in thin films (DGT): soil moisture effects on its performance in soils. *European Journal of Soil Science,* 50**,** 285-294.

HUANG, J.-H. 2014. Impact of Microorganisms on Arsenic Biogeochemistry: A Review. *Water, Air, & Soil Pollution,* 225**,** 1848.

HUANG, Y., HATAYAMA, M. & INOUE, C. 2011. Characterization of As efflux from the roots of As hyperaccumulator Pteris vittata L. *Planta,* 234**,** 1275-1284.

HUGHES, M. F. 2002. Arsenic toxicity and potential mechanisms of action. *Toxicology Letters,* 133**,** 1-16.

IARC. 2004. *IARC Monographs on Evaluation of Carcinogenic Risks to Humans: Vol. 84: Some Drinking-Water Disinfectants and Contaminants, Including Arsenic* [Online]. Vienna: IARC. Available: http://monographs.iarc.fr/ENG/Monographs/vol84/mono84.pdf [Accessed 6 September 2016].

IUSS WORKING GROUP WRB. 2015. *World Reference Base for Soil Resources 2014, update 2015: International soil classification system for naming soils and creating legends for soil maps* [Online]. Rome: FAO. Available: http://www.fao.org/3/a-i3794e.pdf [Accessed 19 January 2017].

JAMES, B. R., BARTLETT, R. J. & AMADON, J. F. 1985. A root observation and sampling chamber (rhizotron) for pot studies. *Plant and Soil,* 85**,** 291-293.

JIANG, J., BAUER, I., PAUL, A. & KAPPLER, A. 2009. Arsenic Redox Changes by Microbially and Chemically Formed Semiquinone Radicals and Hydroquinones in a Humic Substance Model Quinone. *Environmental Science & Technology,* 43**,** 3639-3645.

JONES, C. A., LANGNER, H. W., ANDERSON, K., MCDERMOTT, T. R. & INSKEEP, W. P. 2000. Rates of Microbially Mediated Arsenate Reduction and Solubilization. *Soil Science Society of America Journal,* 64**,** 600-608.

JONES, D. L. 1987. *Encyclopedia of ferns: an introduction to ferns, their structure, biology, economic importance, cultivation and propagation,* Portland, USA, Timber Press.

JONES, D. L., HODGE, A. & KUZYAKOV, Y. 2004. Plant and mycorrhizal regulation of rhizodeposition. *New Phytologist,* 163**,** 459-480.

JUNGK, A. 2002. Dynamics of Nutrient Movement at the Soil–Root Interface. *Plant Roots: The Hidden Half.* New York, USA: Marcel Dekker.

KERTULIS, G. M., MA, L. Q., MACDONALD, G. E., CHEN, R., WINEFORDNER, J. D. & CAI, Y. 2005. Arsenic speciation and transport in Pteris vittata L. and the effects on phosphorus in the xylem sap. *Environmental and Experimental Botany,* 54**,** 239-247.

KIM, M.-J. & NRIAGU, J. 2000. Oxidation of arsenite in groundwater using ozone and oxygen. *Science of The Total Environment,* 247**,** 71-79.

KLIMANT, I., MEYER, V. & KÜHL, M. 1995. Fiber-optic oxygen microsensors, a new tool in aquatic biology. *Limnology and Oceanography,* 40**,** 1159-1165.

KRAEMER, S. M. 2004. Iron oxide dissolution and solubility in the presence of siderophores. *Aquatic Sciences,* 66**,** 3-18.

KREUZEDER, A., SANTNER, J., PROHASKA, T. & WENZEL, W. W. 2013. Gel for simultaneous chemical imaging of anionic and cationic solutes using diffusive gradients in thin films. *Anal Chem,* 85**,** 12028-36.

KREUZEDER, A., SANTNER, J., SCHARSCHING, V., OBURGER, E., HOEFER, C., HANN, S. & WENZEL, W. unpublished. In situ observation of localized, sub-mm scale changes of phosphorus biogeochemistry in the rhizosphere.

KUPPARDT, A., VETTERLEIN, D., HARMS, H. & CHATZINOTAS, A. 2010. Visualisation of gradients in arsenic concentrations around individual roots of Zea mays L. using agar-immobilized bioreporter bacteria. *Plant and Soil,* 329**,** 295-306.

LAMBERS, H., ATKIN, O. & MILLENAAR, F. 2002. Respiratory Patterns in Roots in Relation to Their Functioning. *Plant Roots.* CRC Press.

LAMBERS, H., HAYES, P. E., LALIBERTÉ, E., OLIVEIRA, R. S. & TURNER, B. L. 2015. Leaf manganese accumulation and phosphorus-acquisition efficiency. *Trends in Plant Science,* 20**,** 83-90.

LARSEN, M., BORISOV, S. M., GRUNWALD, B., KLIMANT, I. & GLUD, R. N. 2011. A simple and inexpensive high resolution color ratiometric planar optode imaging approach: application to oxygen and pH sensing. *Limnology and Oceanography: Methods,* 9**,** 348-360.

LEAR, J., HARE, D., ADLARD, P., FINKELSTEIN, D. & DOBLE, P. 2012. Improving acquisition times of elemental bio-imaging for quadrupole-based LA-ICP-MS. *J. Anal. At. Spectrom.,* 27**,** 159-164.

LEHTO, N. J., DAVISON, W., ZHANG, H. & TYCH, W. 2006. Theoretical Comparison of How Soil Processes Affect Uptake of Metals by Diffusive Gradients in Thinfilms and Plants. *Journal of Environmental Quality,* 35**,** 1903-1913.

LESSL, J. T. & MA, L. Q. 2013. Sparingly-Soluble Phosphate Rock Induced Significant Plant Growth and Arsenic Uptake by Pteris vittata from Three Contaminated Soils. *Environmental Science & Technology,* 47**,** 5311-5318.

LIU, F., DE CRISTOFARO, A. & VIOLANTE, A. 2001. Effect of pH, phosphate and oxalate on the adsorption/desorption of arsenate on/from goethite. *Soil Science,* 166**,** 197-208.

LIU, X., FU, J.-W., GUAN, D.-X., CAO, Y., LUO, J., RATHINASABAPATHI, B., CHEN, Y. & MA, L. Q. 2016. Arsenic Induced Phytate Exudation, and Promoted FeAsO4 Dissolution and Plant Growth in As-Hyperaccumulator Pteris vittata. *Environmental Science & Technology,* 50**,** 9070-9077.

LIU, X., FU, J. W., DA SILVA, E., SHI, X. X., CAO, Y., RATHINASABAPATHI, B., CHEN, Y. & MA, L. Q. 2017. Microbial siderophores and root exudates enhanced goethite dissolution and Fe/As uptake by As-hyperaccumulator Pteris vittata. *Environmental Pollution,* 223**,** 230-237.

LIU, X., YANG, G. M., GUAN, D. X., GHOSH, P. & MA, L. Q. 2015. Catecholate-siderophore produced by As-resistant bacterium effectively dissolved FeAsO4 and promoted Pteris vittata growth. *Environ Pollut,* 206**,** 376-81.

LIU, Y., WANG, H. B., WONG, M. H. & YE, Z. H. 2009. The role of arsenate reductase and superoxide dismutase in As accumulation in four Pteris species. *Environment International,* 35**,** 491-495.

LIU, Y., ZHU, Y. G., CHEN, B. D., CHRISTIE, P. & LI, X. L. 2005. Influence of the arbuscular mycorrhizal fungus Glomus mosseae on uptake of arsenate by the As hyperaccumulator fern Pteris vittata L. *Mycorrhiza,* 15**,** 187-92.

LOMBI, E., SLETTEN, R. S. & WENZEL, W. W. 2000. Sequentially Extracted Arsenic from Different Size Fractions of Contaminated Soils. *Water, Air, and Soil Pollution,* 124**,** 319-332.

LOMBI, E., ZHAO, F.-J., FUHRMANN, M., MA, L. Q. & MCGRATH, S. P. 2002. Arsenic distribution and speciation in the fronds of the hyperaccumulator Pteris vittata. *New Phytologist,* 156**,** 195-203.

MA, J. F., YAMAJI, N., MITANI, N., XU, X.-Y., SU, Y.-H., MCGRATH, S. P. & ZHAO, F.-J. 2008. Transporters of arsenite in rice and their role in arsenic accumulation in rice grain. *Proceedings of the National Academy of Sciences,* 105**,** 9931-9935.

MA, L. Q., KOMAR, K. M., CONGU, T., ZHANG, W., CAI, Y. & KENNELLEY, E. D. 2001. A fern that hyperaccumulates arsenic. *Nature,* 409**,** 579.

MANNING, B. A., FENDORF, S. E., BOSTICK, B. & SUAREZ, D. L. 2002. Arsenic(III) Oxidation and Arsenic(V) Adsorption Reactions on Synthetic Birnessite. *Environmental Science & Technology,* 36**,** 976-981.

MARSCHNER, P. 2012. Chapter 15 - Rhizosphere Biology. *Marschner's Mineral Nutrition of Higher Plants (Third Edition).* San Diego: Academic Press.

MASSCHELEYN, P. H., DELAUNE, R. D. & PATRICK, W. H. 1991. Effect of redox potential and pH on arsenic speciation and solubility in a contaminated soil. *Environmental Science & Technology,* 25**,** 1414-1419.

MATHEWS, S., MA, L. Q., RATHINASABAPATHI, B., NATARAJAN, S. & SAHA, U. K. 2010. Arsenic transformation in the growth media and biomass of hyperaccumulator Pteris vittata L. *Bioresource Technology,* 101**,** 8024-8030.

MATHEWS, S., RATHINASABAPATHI, B. & MA, L. Q. 2011. Uptake and translocation of arsenite by Pteris vittata L.: Effects of glycerol, antimonite and silver. *Environmental Pollution,* 159**,** 3490-3495.

MCBRIDE, M. 1994. *Environmental Chemistry of Soils,* New York, Oxford University Press.

MCGONIGLE, T. P., MILLER, M. H., EVANS, D. G., FAIRCHILD, G. L. & SWAN, J. A. 1990. A new method which gives an objective measure of colonization of roots by vesicular—arbuscular mycorrhizal fungi. *New Phytologist,* 115**,** 495-501.

MEADOWS, R. 2014. How Plants Control Arsenic Accumulation. *PLOS Biology,* 12**,** e1002008.

MUNDUS, S., LOMBI, E., HOLM, P. E., ZHANG, H. & HUSTED, S. 2012. Assessing the plant availability of manganese in soils using Diffusive Gradients in Thin films (DGT). *Geoderma,* 183–184**,** 92-99.

NESBITT, H. W., CANNING, G. W. & BANCROFT, G. M. 1998. XPS study of reductive dissolution of 7Å-birnessite by H3AsO3, with constraints on reaction mechanism. *Geochimica et Cosmochimica Acta,* 62**,** 2097-2110.

NEUMANN, G. & RÖMHELD, V. 2007. The Release of Root Exudates as Affected by the Plant Physiological Status. *In:* PINTON, R., VARANINI, Z. & NANNIPIERI, P. (eds.) *The Rhizosphere - Biochemistry and Organic Substances at the Soil-Plant Interface.* 2 ed.: CRC Press.

NEWMAN, D. K., KENNEDY, E. K., COATES, J. D., AHMANN, D., ELLIS, D. J., LOVELY, D. R. & MOREL, F. M. 1997. Dissimilatory arsenate and sulfate reduction in Desulfotomaculum auripigmentum sp. nov. *Arch. Microbiol.,* 168**,** 380-388.

NOLAN, A. L., ZHANG, H. & MCLAUGHLIN, M. J. 2005. Prediction of Zinc, Cadmium, Lead, and Copper Availability to Wheat in Contaminated Soils Using Chemical Speciation, Diffusive Gradients in Thin Films, Extraction, and Isotopic Dilution Techniques. *Journal of Environmental Quality,* 34**,** 496-507.

OBURGER, E. & SCHMIDT, H. 2016. New Methods To Unravel Rhizosphere Processes. *Trends Plant Sci,* 21**,** 243-55.

OREMLAND, R. S. & STOLZ, J. F. 2003. The Ecology of Arsenic. *Science,* 300**,** 939-944.

OSCARSON, D. W., HUANG, P. M., DEFOSSE, C. & HERBILLON, A. 1981. Oxidative power of Mn(IV) and Fe(III) oxides with respect to As(III) in terrestrial and aquatic environments. *Nature,* 291**,** 50-51.

PICKERING, I. J., GUMAELIUS, L., HARRIS, H. H., PRINCE, R. C., HIRSCH, G., BANKS, J. A., SALT, D. E. & GEORGE, G. N. 2006. Localizing the Biochemical Transformations of Arsenate in a Hyperaccumulating Fern. *Environmental Science & Technology,* 40**,** 5010-5014.

POYNTON, C. Y., HUANG, J. W., BLAYLOCK, M. J., KOCHIAN, L. V. & ELLESS, M. P. 2004. Mechanisms of arsenic hyperaccumulation in Pteris species: root As influx and translocation. *Planta,* 219**,** 1080-1088.

PUY, J., GALCERAN, J. & REY-CASTRO, C. 2016. Interpreting the DGT Measurement. *In:* DAVISON, W. (ed.) *Diffusive Gradients in Thin-Films for Environmental Measurements.* Cambridge: Cambridge University Press.

RHOADES, J. D. 1982. Soluble Salts. *In:* PAGE, A. L., MILLER, R. H. & KENNEY, D. R. (eds.) *Methods of Soil Analysis. Part 2. Chemical and Microbiological Properties.* Madison, WI: American Society of Agronomy, Soil Science Society of America.

ROCHETTE, E. A., BOSTICK, B. C., LI, G. & FENDORF, S. 2000. Kinetics of Arsenate Reduction by Dissolved Sulfide. *Environmental Science & Technology,* 34**,** 4714-4720.

SADIQ, M. 1997. Arsenic chemistry in soils: An overview of thermodynamic predictions and field observations. *Water, Air, and Soil Pollution,* 93**,** 117-136.

SALT, D. E., SMITH, R. D. & RASKIN, I. 1998. Phytoremediation. *Annual Review of Plant Physiology and Plant Molecular Biology,* 49**,** 643-668.

SANTNER, J., KREUZEDER, A., SCHNEPF, A. & WENZEL, W. W. 2015a. Numerical Evaluation of Lateral Diffusion Inside Diffusive Gradients in Thin Films Samplers. *Environmental Science & Technology,* 49**,** 6109-6116.

SANTNER, J., LARSEN, M., KREUZEDER, A. & GLUD, R. N. 2015b. Two decades of chemical imaging of solutes in sediments and soils--a review. *Anal Chim Acta,* 878**,** 9-42.

SANTNER, J. & WILLIAMS, P. N. 2016. Measurement at High Spatial Resolution. *In:* DAVISON, W. (ed.) *Diffusive Gradients In Thin-Films For Environmental Measurements.* Cambridge: Cambridge University Press.

SANTNER, J., ZHANG, H., LEITNER, D., SCHNEPF, A., PROHASKA, T., PUSCHENREITER, M. & WENZEL, W. W. 2012. High-resolution chemical imaging of labile phosphorus in the rhizosphere of Brassica napus L. cultivars. *Environmental and Experimental Botany,* 77**,** 219-226.

SCALLY, S., DAVISON, W. & ZHANG, H. 2003. In Situ Measurements of Dissociation Kinetics and Labilities of Metal Complexes in Solution Using DGT. *Environmental Science & Technology,* 37**,** 1379-1384.

SCOTT, M. J. & MORGAN, J. J. 1995. Reactions at Oxide Surfaces. 1. Oxidation of As(III) by Synthetic Birnessite. *Environmental Science & Technology,* 29**,** 1898-1905.

SMEDLEY, P. L. & KINNIBURGH, D. G. 2002. A review of the source, behaviour and distribution of arsenic in natural waters. *Applied Geochemistry,* 17**,** 517-568.

SMEDLEY, P. L. & KINNIBURGH, D. G. 2013. Arsenic in Groundwater and the Environment. *In:* SELINUS, O. (ed.) *Essentials of Medical Geology: Revised Edition.* Dordrecht: Springer Netherlands.

SMITH, S. E., CHRISTOPHERSEN, H. M., POPE, S. & SMITH, F. A. 2010. Arsenic uptake and toxicity in plants: integrating mycorrhizal influences. *Plant and Soil,* 327**,** 1-21.

SMITH, S. E. & READ, D. 2008. Mineral nutrition, toxic element accumulation and water relations of arbuscular mycorrhizal plants. *Mycorrhizal Symbiosis (Third Edition).* London: Academic Press.

SPARKS, D. L. 2003. The Chemistry of Soil Acidity. *Environmental Soil Chemistry (Second Edition).* Burlington: Academic Press.

SRIVASTAVA, M., MA, L. Q. & SANTOS, J. A. 2006. Three new arsenic hyperaccumulating ferns. *Sci Total Environ,* 364**,** 24-31.

STAHL, H., WARNKEN, K. W., SOCHACZEWSKI, L., GLUD, R. N., DAVISON, W. & ZHANG, H. 2012. A combined sensor for simultaneous high resolution 2-D imaging of oxygen and trace metals fluxes. *Limnology and Oceanography: Methods,* 10**,** 389-401.

STRÖM, L. 1997. Root Exudation of Organic Acids: Importance to Nutrient Availability and the Calcifuge and Calcicole Behaviour of Plants. *Oikos,* 80**,** 459-466.

SU, Y. H., MCGRATH, S. P., ZHU, Y. G. & ZHAO, F. J. 2008. Highly efficient xylem transport of arsenite in the arsenic hyperaccumulator Pteris vittata. *New Phytologist,* 180**,** 434-441.

SUDA, A. & MAKINO, T. 2016. Functional effects of manganese and iron oxides on the dynamics of trace elements in soils with a special focus on arsenic and cadmium: A review. *Geoderma,* 270**,** 68-75.

SUN, Q., CHEN, J., ZHANG, H., DING, S., LI, Z., WILLIAMS, P. N., CHENG, H., HAN, C., WU, L. & ZHANG, C. 2014. Improved Diffusive Gradients in Thin Films (DGT) Measurement of Total Dissolved Inorganic Arsenic in Waters and Soils Using a Hydrous Zirconium Oxide Binding Layer. *Analytical Chemistry,* 86**,** 3060-3067.

TAO, Y., ZHANG, S., JIAN, W., YUAN, C. & SHAN, X.-Q. 2006. Effects of oxalate and phosphate on the release of arsenic from contaminated soils and arsenic accumulation in wheat. *Chemosphere,* 65**,** 1281-1287.

TEBO, B. M., BARGAR, J. R., CLEMENT, B. G., DICK, G. J., MURRAY, K. J., PARKER, D., VERITY, R. & WEBB, S. M. 2004. Biogenic manganese oxides: Properties and Mechanisms of Formation. *Annual Review of Earth and Planetary Sciences,* 32**,** 287-328.

TEBO, B. M., JOHNSON, H. A., MCCARTHY, J. K. & TEMPLETON, A. S. 2005. Geomicrobiology of manganese(II) oxidation. *Trends in Microbiology,* 13**,** 421-428.

THOMPSON, I. A., HUBER, D. M., GUEST, C. A. & SCHULZE, D. G. 2005. Fungal manganese oxidation in a reduced soil. *Environmental Microbiology,* 7**,** 1480-1487.

TU, S., MA, L. & LUONGO, T. 2004. Root exudates and arsenic accumulation in arsenic hyperaccumulating Pteris vittata and non-hyperaccumulating Nephrolepis exaltata. *Plant and Soil,* 258**,** 9-19.

ULTRA, V. U., TANAKA, S., SAKURAI, K. & IWASAKI, K. 2007a. Effects of arbuscular mycorrhiza and phosphorus application on arsenic toxicity in sunflower (Helianthus annuus L.) and on the transformation of arsenic in the rhizosphere. *Plant and Soil,* 290**,** 29-41.

ULTRA, V. U. Y., TANAKA, S., SAKURAI, K. & IWASAKI, K. 2007b. Arbuscular mycorrhizal fungus (Glomus aggregatum) influences biotransformation of arsenic in the

rhizosphere of sunflower (Helianthus annuus L.). *Soil Science & Plant Nutrition,* 53**,** 499-508.

VETTERLEIN, D., SZEGEDI, K., ACKERMANN, J., MATTUSCH, J., NEUE, H.-U., TANNEBERG, H. & JAHN, R. 2007. Competitive Mobilization of Phosphate and Arsenate Associated with Goethite by Root Activity. *Journal of Environmental Quality,* 36**,** 1811-1820.

VIERHEILIG, H., COUGHLAN, A. P., WYSS, U. & PICHÉ, Y. 1998. Ink and Vinegar, a Simple Staining Technique for Arbuscular-Mycorrhizal Fungi. *Applied and Environmental Microbiology,* 64**,** 5004-5007.

WAN, X., LEI, M., CHEN, T. & MA, J. 2017. Micro-distribution of arsenic species in tissues of hyperaccumulator Pteris vittata L. *Chemosphere,* 166**,** 389-399.

WANG, J., BAI, L., ZENG, X., SU, S., WANG, Y. & WU, C. 2014. Assessment of arsenic availability in soils using the diffusive gradients in thin films (DGT) technique-a comparison study of DGT and classic extraction methods. *Environmental Science: Processes & Impacts,* 16**,** 2355-2361.

WANG, J., ZHAO, F. J., MEHARG, A. A., RAAB, A., FELDMANN, J. & MCGRATH, S. P. 2002. Mechanisms of arsenic hyperaccumulation in Pteris vittata. Uptake kinetics, interactions with phosphate, and arsenic speciation. *Plant Physiol,* 130**,** 1552-61.

WANG, X. & MA, L. Q. 2015. Recent advances in phytoremediation of arsenic-contaminated soils. *In:* BUNDSCHUH, J., HOLLÄNDER, H. M. & MA, L. Q. (eds.) *In-situ Remediation of Arsenic-Contaminated Sites.* London, UK.: Taylor & Francis Group.

WANG, X., MA, L. Q., RATHINASABAPATHI, B., CAI, Y., LIU, Y. G. & ZENG, G. M. 2011. Mechanisms of efficient arsenite uptake by arsenic hyperaccumulator Pteris vittata. *Environ Sci Technol,* 45**,** 9719-25.

WANG, X., MA, L. Q., RATHINASABAPATHI, B., LIU, Y. & ZENG, G. 2010. Uptake and translocation of arsenite and arsenate by Pteris vittata L.: Effects of silicon, boron and mercury. *Environmental and Experimental Botany,* 68**,** 222-229.

WANG, X., RATHINASABAPATHI, B., OLIVEIRA, L. M. D., GUILHERME, L. R. G. & MA, L. Q. 2012. Bacteria-Mediated Arsenic Oxidation and Reduction in the Growth Media of Arsenic Hyperaccumulator Pteris vittata. *Environmental Science & Technology,* 46**,** 11259-11266.

WARNKEN, K. W., DAVISON, W., ZHANG, H., GALCERAN, J. & PUY, J. 2007. In Situ Measurements of Metal Complex Exchange Kinetics in Freshwater. *Environmental Science & Technology,* 41**,** 3179-3185.

WARNKEN, K. W., ZHANG, H. & DAVISON, W. 2004a. Analysis of Polyacrylamide Gels for Trace Metals Using Diffusive Gradients in Thin Films and Laser Ablation Inductively Coupled Plasma Mass Spectrometry. *Analytical Chemistry,* 76**,** 6077-6084.

WARNKEN, K. W., ZHANG, H. & DAVISON, W. 2004b. Performance characteristics of suspended particulate reagent-iminodiacetate as a binding agent for diffusive gradients in thin films. *Analytica Chimica Acta,* 508**,** 41-51.

WATT, M., SILK, W. K. & PASSIOURA, J. B. 2006. Rates of Root and Organism Growth, Soil Conditions, and Temporal and Spatial Development of the Rhizosphere. *Annals of Botany,* 97**,** 839-855.

WENZEL, W. W. 2009. Rhizosphere processes and management in plant-assisted bioremediation (phytoremediation) of soils. *Plant and Soil,* 321**,** 385-408.

WENZEL, W. W. 2013. Arsenic. *In:* ALLOWAY, B. (ed.) *Heavy Metals in Soils: Trace Metals and Metalloids in Soils and their Bioavailability.* 3 ed. Dordrecht: Springer Science+Business Media.

WENZEL, W. W., BRANDSTETTER, A., WUTTE, H., LOMBI, E., PROHASKA, T., STINGEDER, G. & ADRIANO, D. C. 2002. Arsenic in field-collected soil solutions and extracts of contaminated soils and its implication to soil standards. *Journal of Plant Nutrition and Soil Science,* 165**,** 221-228.

WENZEL, W. W., KIRCHBAUMER, N., PROHASKA, T., STINGEDER, G., LOMBI, E. & ADRIANO, D. C. 2001. Arsenic fractionation in soils using an improved sequential extraction procedure. *Analytica Chimica Acta,* 436**,** 309-323.

WENZEL, W. W., LOMBI, E. & ADRIANO, D. C. 2004. Root and Rhizosphere Processes in Metal Hyperaccumulation and Phytoremediation Technology. *In:* PRASAD, M. N. V. (ed.) *Heavy Metal Stress in Plants: From Biomolecules to Ecosystems.* Berlin, Heidelberg: Springer Berlin Heidelberg.

WHITE, P. J. 2012. Chapter 2 - Ion Uptake Mechanisms of Individual Cells and Roots: Short-distance Transport A2 - Marschner, Petra. *Marschner's Mineral Nutrition of Higher Plants (Third Edition).* San Diego: Academic Press.

WILLIAMS, P. N., SANTNER, J., LARSEN, M., LEHTO, N. J., OBURGER, E., WENZEL, W., GLUD, R. N., DAVISON, W. & ZHANG, H. 2014. Localized flux maxima of arsenic, lead, and iron around root apices in flooded lowland rice. *Environ Sci Technol,* 48**,** 8498-506.

XU, J.-Y., HAN, Y.-H., CHEN, Y., ZHU, L.-J. & MA, L. Q. 2016. Arsenic transformation and plant growth promotion characteristics of As-resistant endophytic bacteria from As-hyperaccumulator Pteris vittata. *Chemosphere,* 144**,** 1233-1240.

XU, X., CHEN, C., WANG, P., KRETZSCHMAR, R. & ZHAO, F.-J. 2017. Control of arsenic mobilization in paddy soils by manganese and iron oxides. *Environmental Pollution,* 231, Part 1**,** 37-47.

XU, X. Y., MCGRATH, S. P. & ZHAO, F. J. 2007. Rapid reduction of arsenate in the medium mediated by plant roots. *New Phytologist,* 176**,** 590-599.

YING, S. C., KOCAR, B. D. & FENDORF, S. 2012. Oxidation and competitive retention of arsenic between iron- and manganese oxides. *Geochimica et Cosmochimica Acta,* 96**,** 294-303.

ZHANG, H. & DAVISON, W. 1995. Performance Characteristics of Diffusion Gradients in Thin Films for the in Situ Measurement of Trace Metals in Aqueous Solution. *Analytical Chemistry,* 67**,** 3391-3400.

ZHANG, H., LOMBI, E., SMOLDERS, E. & MCGRATH, S. 2004. Kinetics of Zn Release in Soils and Prediction of Zn Concentration in Plants Using Diffusive Gradients in Thin Films. *Environmental Science & Technology,* 38**,** 3608-3613.

ZHANG, H., ZHAO, F.-J., SUN, B., DAVISON, W. & MCGRATH, S. P. 2001. A New Method to Measure Effective Soil Solution Concentration Predicts Copper Availability to Plants. *Environmental Science & Technology,* 35**,** 2602-2607.

ZHANG, S., LI, W., SHAN, X.-Q., LU, A. & ZHOU, P. 2005. Effects of Low Molecular Weight Organic Anions on the Release of Arsenite and Arsenate from a Contaminated Soil. *Water, Air, and Soil Pollution,* 167**,** 111-122.

ZHAO, F.-J., AGO, Y., MITANI, N., LI, R.-Y., SU, Y.-H., YAMAJI, N., MCGRATH, S. P. & MA, J. F. 2010. The role of the rice aquaporin Lsi1 in arsenite efflux from roots. *New Phytologist,* 186**,** 392-399.

ZHAO, F. J., MA, J. F., MEHARG, A. A. & MCGRATH, S. P. 2009. Arsenic uptake and metabolism in plants. *New Phytologist,* 181**,** 777-794.